

# Learning nonlinear constitutive models in finite strain thermo-electro-mechanics with physics-augmented neural networks

R. Ortigosa<sup>†1</sup>, J. Martínez-Frutos<sup>†2</sup>, A. Pérez-Escolar<sup>†</sup>, I. Castañar<sup>‡</sup>, A. J. Gil<sup>‡3</sup>

† Technical University of Cartagena, Campus Muralla del Mar, 30202, Cartagena (Murcia), Spain

‡Zienkiewicz Centre for Computational Engineering

Faculty of Science and Engineering, Swansea University

Bay Campus, SA1 8EN, United Kingdom

---

## Abstract

The aim of this paper is the design a new one-step implicit and thermodynamically consistent Energy-Momentum (EM) preserving time integration scheme for the simulation of thermo-elastic processes undergoing large deformations and temperature fields. Following [11], we consider well-posed constitutive models for the entire range of deformations and temperature. In that regard, the consideration of polyconvexity inspired constitutive models and a new tensor cross product algebra are shown to be crucial in order to derive the so-called discrete derivatives, fundamental for the construction of the algorithmic derived variables, namely the second Piola-Kirchoff stress tensor and the entropy (or the absolute temperature). The proposed scheme inherits the advantages of the EM scheme recently published by Franke et al. [14], whilst resulting in a simpler scheme from the implementation standpoint. A series of numerical examples will be presented in order to demonstrate the robustness and applicability of the new EM scheme. Although the examples presented will make use of a temperature-based version of the EM scheme (using the Helmholtz free energy as the thermodynamical potential and the temperature as the thermodynamical state variable), we also include in an Appendix an entropy-based analogue EM scheme (using the internal energy as the thermodynamical potential and the entropy as the thermodynamical state variable).

*Keywords:* finite element method, nonlinear thermo-elastodynamics, energy-momentum scheme, structure-preserving discretisation.

---

## 1. Introduction

The development of thermo-elastic constitutive models for the simulation of materials undergoing external mechanical and thermal loading has been the focus of intensive study in numerous References [14, 21]. These constitutive models are typically based on an invariant representation of the Helmholtz free energy functional, defined in terms of the deformation gradient tensor  $\mathbf{F}$  (through the objective right Cauchy-Green tensor  $\mathbf{C}$ ) and the *absolute temperature*  $\theta$  (temperature in the sequel). Based on this energy (potential) functional, many authors [14, 21] have proposed temperature-based consistent implicit energy momentum (EM) time integration schemes for the long term simulation of structural components governed by this Helmholtz potential. This type of time integration schemes are well-known for their robustness and stability properties due to their structure-preserving features, making them ideal for long term stable simulations. We purposely

---

<sup>1</sup>Corresponding author: r.ortigosa@swansea.ac.uk

<sup>2</sup>Corresponding author: jesus.martinez@upct.es

<sup>3</sup>Corresponding author: a.j.gil@swansea.ac.uk

use the term *temperature-based* to stress the fact that this type of algorithms rely on the temperature field as the thermodynamical state variable and, as such, this temperature represents one of the unknowns to be solved.

EM schemes are regarded as both elegant and robust because they are endowed by construction with the discrete analogue of the conservation properties of the continuum, namely the conservation of total energy, linear and angular momenta. The *consistency* of EM schemes refers to their ability to preserve (or dissipate for non-reversible constitutive models) the total energy of a system in agreement with the laws of thermodynamics [17, 6, 14, 21]. Consistency of these methods is attained by replacing the (exact) partial derivatives of the Helmholtz free energy functional with respect to its arguments ( $\mathbf{C}$  and  $\theta$ ) with their carefully designed algorithmic counterparts. These algorithmic partial derivatives, also known as *discrete derivatives* [14, 6, 22, 15, 25], are formulated in compliance with the so-called *directionality property* [15]. Unfortunately, the success of current temperature-based EM consistent integrators rely on the introduction of discrete derivatives incorporating consistency restoring terms [18] which are not that straightforward to be systematised and generalised, especially if interested in pursuing multi-physics applications beyond thermo-mechanics.

An alternative approach uses the entropy-based GENERIC framework, where the entropy  $\eta$  is considered as the thermodynamical state variable (see the works of Romero [23] and Conde [21]), where EM schemes have been also successfully developed. However, a well-accepted difficulty of entropy-based formulations is the non-trivial consideration of temperature boundary conditions. Indeed, unless relatively simple thermo-mechanical models are considered, a (computationally expensive) Newton-Raphson type procedure is required in order to solve a nonlinear equation relating  $\eta$  and  $\theta$  on the part of the boundary subjected to prescribed temperature (at each boundary quadrature point). This is one of the main reasons to prefer the Helmholtz free energy functional as a thermodynamic potential over the internal energy and, thus, the temperature over the entropy as the thermodynamical state variable.

Very recently, Franke et. al. [14] have proposed a novel EM scheme in the context of thermo-elasticity, by taking advantage of the concept of isothermal polyconvexity [1, 2, 3, 4, 24] and the use of a novel tensor cross product pioneered by de Boer [12] and re-discovered in the context of nonlinear continuum mechanics by Bonet et al. [9, 8, 7]. In essence, the authors propose the consideration of four discrete derivatives which are used to form algorithmic versions of the second Piola-Kirchoff stress tensor and the entropy of the system. In addition to the discrete derivative with respect to the temperature, three further discrete derivatives are presented, which represent the algorithmic counterparts of the work conjugates of the right Cauchy-Green deformation tensor, its co-factor and its determinant. This strategy leads to simplified expressions of the algorithmic second Piola-Kirchoff stress tensor and entropy, when comparing against those obtained following the classical approach [15]. Finally, as the EM scheme in [14] relies on the *re-definition* of the internal energy of the system in terms of the temperature, this ultimately entails a certain level of complexity in the derivation of the discrete derivatives (refer to Appendix B).

The aim of the current paper is the development of a new polyconvexity inspired temperature-based EM scheme which uses the Helmholtz free energy functional as the fundamental thermodynamical potential. As a result, the new EM scheme will be shown to inherit the advantages of that of [14] (i.e. consistency, stability, conservation) whilst, in addition, resulting in dramatically far simpler algorithmic expressions. We conceive the simplification brought forward by the new EM scheme as a crucial preliminary step in order to bridge the gap with recently published EM schemes developed by the authors in the context of electro-elasticity [22] and, therefore, seek extension to thermo-electro-elasticity.

The outline of this paper is as follows: in Section 2, some basic principles of kinematics are presented. The governing equations in nonlinear thermo-elastodynamics are also presented in this section. Section 3 introduces the Helmholtz free energy functional and the internal en-

ergy functional. Section ?? presents the weak forms associated with the governing equations in thermo-elastodynamics. These will help introducing the new temperature-based one-step implicit EM time integrator scheme for thermo-elastodynamics in Section ???. Section 5 briefly describes the finite element implementation of the new time integrator scheme and Section ?? presents a series of numerical examples in order to validate the conservation properties and robustness of the new scheme. Finally, Section 7 provides some concluding remarks. Appendix A presents an entropy-based EM scheme, counterpart of the temperature-based scheme pursued in this paper. Appendix B outlines the definition of the discrete derivative expressions featuring in the proposed time integrator in Section ???. Appendix C summarises the EM scheme in Reference [14], illustrating the differences between this and the new EM proposed. Appendix D presents the steps that need to be carried out in order to derive the thermo-elastic constitutive model presented in Section ??.

*Notation:* Throughout this paper,  $\mathbf{A} : \mathbf{B} = A_{iI}B_{iI}$ ,  $\forall \mathbf{A}, \mathbf{B} \in \mathbb{R}^{3 \times 3}$ , and the use of repeated indices implies summation. The tensor product is denoted by  $\otimes$  and the second order identity tensor by  $\mathbf{I}$ . The tensor cross product operation  $\mathbf{x}$  between two arbitrary second order tensor  $\mathbf{A}$  and  $\mathbf{B}$  entails  $[\mathbf{A} \mathbf{x} \mathbf{B}]_{iI} = \mathcal{E}_{ijk}\mathcal{E}_{IJK}A_{jJ}B_{kK}$ . Furthermore,  $\mathcal{E}$  represents the third-order alternating tensor. Lower case indices  $\{i, j, k\}$  will be used to represent the spatial configuration whereas capital case indices  $\{I, J, K\}$  will be used to represent the material configuration. The full and special orthogonal groups in  $\mathbb{R}^3$  are represented as  $O(3) = \{\mathbf{A} \in \mathbb{R}^{3 \times 3}, |\mathbf{A}^T \mathbf{A} = \mathbf{I}\}$  and  $SO(3) = \{\mathbf{A} \in \mathbb{R}^{3 \times 3}, |\mathbf{A}^T \mathbf{A} = \mathbf{I}, \det \mathbf{A} = 1\}$ , respectively and the set of invertible second order tensors with positive determinant is denoted by  $GL^+(3) = \{\mathbf{A} \in \mathbb{R}^{3 \times 3} | \det \mathbf{A} > 0\}$ . Differentiation with respect to time of any field  $(\bullet)$  will be denoted through  $(\bullet)$ .

## 2. Nonlinear continuum thermo-electro-mechanics

A brief introduction into nonlinear continuum mechanics and the relevant governing equations will be presented in this section.

### 2.1. Kinematics: motion and deformation

Let us consider the motion of an EAP with reference configuration  $\mathcal{B}_0 \in \mathbb{R}^3$  (refer to Figure 1). After the motion, the continuum  $\mathcal{B}_0$  occupies a deformed configuration  $\mathcal{B} \in \mathbb{R}^3$ . The deformation mapping  $\phi(\mathbf{X}, t)$  links a material particle from the reference configuration  $\mathbf{X} \in \mathcal{B}_0$  to the deformed configuration  $\mathbf{x} \in \mathcal{B}$  according to  $\mathbf{x} = \phi(\mathbf{X}, t)$ . Associated with  $\phi$ , we define the deformation gradient tensor  $\mathbf{F} \in GL^+(3)$  (or fibre map) [10, 16, 13, 5] as  $\mathbf{F} = \partial_{\mathbf{X}}\phi$ . The later permits to introduce its co-factor  $\mathbf{H}$  (or area map) and its Jacobian  $J$  (or volume map), according to

$$\mathbf{H} = (\det \mathbf{F}) \mathbf{F}^{-T}; \quad J = \det \mathbf{F}, \quad (1)$$

which can be equivalently re-written as [12, 9] as

$$\mathbf{H} = \frac{1}{2} \mathbf{F} \mathbf{x} \mathbf{F}; \quad J = \frac{1}{3} \mathbf{H} : \mathbf{F}, \quad (2)$$

### 2.2. Governing equations in nonlinear thermo-mechanics

The behaviour of the EAP is governed by a system of coupled PDEs. These include the conservation of linear momentum [16], which can be recast in a Lagrangian setting as

$$\begin{aligned} \rho_0 \dot{\mathbf{v}} - \text{DIV} \mathbf{P} - \mathbf{f}_0 &= \mathbf{0}; & \text{in } \mathcal{B}_0 \times [0, T]; \\ \mathbf{P} \mathbf{N} &= \mathbf{t}_0; & \text{on } \partial_t \mathcal{B}_0 \times [0, T]; \\ \phi &= \bar{\phi}; & \text{on } \partial_\phi \mathcal{B}_0 \times [0, T]; \\ \phi|_{t=0} &= \bar{\phi}_0; & \text{in } \mathcal{B}_0; \\ \dot{\phi}|_{t=0} &= \bar{v}_0; & \text{in } \mathcal{B}_0, \end{aligned} \quad (3)$$

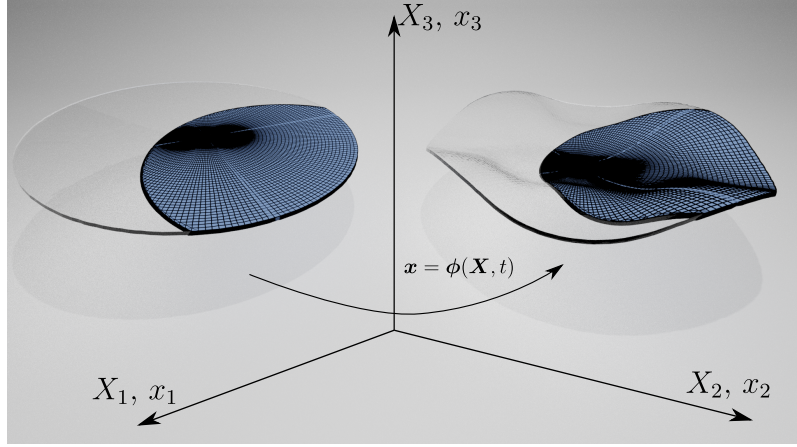


Figure 1: The mapping  $\phi$  and the reference  $\mathcal{B}_0$  (left) and deformed  $\mathcal{B}$  (right) configurations.

where  $\rho_0 : \mathcal{B}_0 \rightarrow \mathbb{R}^+$  represents the mass density of the continuum in the reference configuration,  $\mathbf{v}$  the velocity field. Furthermore,  $\mathbf{f}_0$  represents a body force per unit undeformed volume  $\mathcal{B}_0$  and  $\mathbf{t}_0$ , the traction force per unit undeformed area applied on  $\partial_t \mathcal{B}_0 \subset \partial \mathcal{B}_0$ , such that  $\partial_t \mathcal{B}_0 \cup \partial_\phi \mathcal{B}_0 = \partial \mathcal{B}_0$  and  $\partial_t \mathcal{B}_0 \cap \partial_\phi \mathcal{B}_0 = \emptyset$ . Moreover,  $\bar{\phi}$  represents the Dirichlet condition for  $\phi$ ,  $\bar{\phi}_0$  and  $\bar{\mathbf{v}}_0$  are the initial conditions for the mapping  $\phi$  and the velocity fields, respectively. Finally, local conservation of angular momentum leads to the well-known tensor condition  $\mathbf{F}\mathbf{P} = \mathbf{P}^T\mathbf{F}^T$ , where  $\mathbf{P}$  represents the first Piola-Kirchhoff stress tensor.

The second set of PDEs that govern the behaviour of the EAP comprises the electrostatic form of the Gauss' and Faraday's laws, recast in a Lagrangian setting as follows

$$\begin{aligned} \mathbf{E}_0 &= -\partial_{\mathbf{X}}\varphi; && \text{in } \mathcal{B}_0 \times [0, T]; \\ \text{DIV} \mathbf{D}_0 &= -\rho_0^e; && \text{in } \mathcal{B}_0 \times [0, T]; \\ \mathbf{D}_0 \cdot \mathbf{N} &= -\omega_0^e; && \text{on } \partial_\omega \mathcal{B}_0 \times [0, T]; \\ \varphi &= \bar{\varphi}; && \text{on } \partial_\varphi \mathcal{B}_0 \times [0, T], \end{aligned} \quad (4)$$

where  $\varphi : \mathcal{B}_0 \rightarrow \mathbb{R}$  represents the electric potential,  $\rho_0^e : \mathcal{B}_0 \rightarrow \mathbb{R}$  is the electric charge per unit volume in the reference configuration and  $\omega_0$ , the electric charge per unit undeformed area applied on  $\partial_\omega \mathcal{B}_0 \subset \partial \mathcal{B}_0$ , such that  $\partial_\omega \mathcal{B}_0 \cup \partial_\varphi \mathcal{B}_0 = \partial \mathcal{B}_0$  and  $\partial_\omega \mathcal{B}_0 \cap \partial_\varphi \mathcal{B}_0 = \emptyset$ . Finally,  $\bar{\varphi}$  represents the Dirichlet condition for  $\varphi$ . In above equation (4),  $\mathbf{E}_0$  and  $\mathbf{D}_0$  represent the material electric field and electric displacement field, respectively.

Finally, the last coupled PDE governing the behaviour of the EAP is the balance of energy, which in the absence of internal state variables (i.e. plastic strain or viscoelasticity), can be written in a Lagrangian setting as

$$\begin{aligned} \theta\dot{\eta} + \text{DIV} \mathbf{Q} - R_\theta &= 0; && \text{in } \mathcal{B}_0 \times [0, T]; \\ \mathbf{Q} \cdot \mathbf{N} &= -Q_\theta; && \text{on } \partial_Q \mathcal{B}_0 \times [0, T]; \\ \theta &= \bar{\theta}; && \text{on } \partial_\theta \mathcal{B}_0 \times [0, T]; \\ \theta|_{t=0} &= \bar{\theta}_0; && \text{in } \mathcal{B}_0, \end{aligned} \quad (5)$$

where  $\theta$  is the absolute temperature field and  $\eta$  and  $\mathbf{Q}$ , the entropy and heat flux per unit undeformed volume  $\mathcal{B}_0$ , respectively. In addition,  $R_\theta$  represents the heat source per unit undeformed volume  $\mathcal{B}_0$  and  $Q_\theta$ , the heat source per unit undeformed area applied on  $\partial_Q \mathcal{B}_0 \subset \partial \mathcal{B}_0$ . In (5),  $\partial_\theta \mathcal{B}_0$  represents the part of the boundary  $\partial \mathcal{B}_0$  where essential temperature boundary conditions are applied such that  $\partial_Q \mathcal{B}_0 \cup \partial_\theta \mathcal{B}_0 = \partial \mathcal{B}_0$  and  $\partial_Q \mathcal{B}_0 \cap \partial_\theta \mathcal{B}_0 = \emptyset$ .

### 3. Constitutive equations in nonlinear thermo-electro-elasticity

The governing equations presented in Section 2 are coupled by means of a suitable constitutive law. The objective of the following section is to introduce some notions on constitutive laws in thermo-electro-elasticity.

#### 3.1. The Helmholtz free energy

In the case of thermo-electro-elasticity, and in the absence of internal state variables, the Helmholtz free energy  $\Psi$  per unit of undeformed volume can be defined as

$$\Psi : \text{GL}^+(3) \times \mathbb{R}^3 \times \mathbb{R}^+ \rightarrow \Psi(\mathbf{F}, \mathbf{E}_0, \theta) \quad (6)$$

In order to derive constitutive equations, we begin with the Clausius-Duhem inequality, which takes the following form

$$-\dot{\Psi} + \mathbf{P} : \dot{\mathbf{F}} - \mathbf{D}_0 \cdot \dot{\mathbf{E}}_0 - \eta \dot{\theta} - \frac{1}{\theta} \mathbf{Q} \cdot \partial_{\mathbf{x}} \theta \geq 0 \quad (7)$$

For the EAP, following [?], use of the Coleman-Noll procedure into (7)

$$(\mathbf{P} - \partial_F \Psi) : \dot{\mathbf{F}} - (\mathbf{D}_0 + \partial_{\mathbf{E}_0} \Psi) \cdot \dot{\mathbf{E}}_0 - (\eta + \partial_{\theta} \Psi) \dot{\theta} - \frac{1}{\theta} \mathbf{Q} \cdot \partial_{\mathbf{x}} \theta \geq 0 \quad (8)$$

Fourier law relates the spatial heat flux  $\mathbf{q}$  and the spatial gradient of  $\theta$  by virtue of the following expression

$$\mathbf{q} = -\mathbf{k} \partial_{\mathbf{x}} \theta, \quad (9)$$

where  $\mathbf{k}$  represents the semi-positive definite second order thermal conductivity tensor in the deformed configuration. The relation between  $\mathbf{q}$  and its material counterpart  $\mathbf{Q}$  in (5) can be carried out by making use of the Gauss' theorem and the Nanson's rule (i.e.  $d\mathbf{a} = \mathbf{H} d\mathbf{A}$ ), yielding [?]

$$\mathbf{Q} = -\mathbf{K} \partial_{\mathbf{x}} \theta; \quad \mathbf{K} = J^{-1} \mathbf{H}^T \mathbf{k} \mathbf{H}. \quad (10)$$

Positive definiteness of the material thermal conductivity tensor  $\mathbf{K}$  permits to establish [16?] the following relationships

$$\mathbf{P} = \partial_F \Psi(\mathbf{F}, \mathbf{E}_0, \theta); \quad \mathbf{D}_0 = -\partial_{\mathbf{E}_0} \Psi(\mathbf{F}, \mathbf{E}_0, \theta); \quad \eta = -\partial_{\theta} \Psi(\mathbf{F}, \mathbf{E}_0, \theta). \quad (11)$$

The Helmholtz free energy density must adhere to the principle of objectivity or material frame indifference, which entails its invariance with respect to rotations  $\mathbf{Q} \in \text{SO}(3)$  applied to the spatial configuration, namely

$$\Psi(\mathbf{Q} \mathbf{F}, \mathbf{E}_0, \theta) = \Psi(\mathbf{F}, \mathbf{E}_0, \theta); \quad \forall \mathbf{F} \in \text{GL}^+(3), \mathbf{E}_0 \in \mathbb{R}^3, \theta \in \mathbb{R}^+, \mathbf{Q} \in \text{SO}(3). \quad (12)$$

Furthermore, a second invariance condition must hold, known as the material symmetry conditions, which reads as follows

$$\Psi(\mathbf{F} \mathbf{Q}^T, \mathbf{Q} \mathbf{E}_0, \theta) = \Psi(\mathbf{F}, \mathbf{E}_0, \theta); \quad \forall \mathbf{F} \in \text{GL}^+(3), \mathbf{E}_0 \in \mathbb{R}^3, \theta \in \mathbb{R}^+, \mathbf{Q} \in \mathcal{G} \subset \text{O}(3), \quad (13)$$

where  $\mathcal{G}$  denotes the symmetry group of the material under consideration. Section 3.3 will demonstrate how the two physical conditions specified in equation (12) and (13) can be imposed a priori. Moreover, the Helmholtz free energy density  $\Psi(\mathbf{F}, \mathbf{E}_0, \theta)$ , along with the first Piola-Kirchhoff stress tensor  $\mathbf{P}(\mathbf{F}, \mathbf{E}_0, \theta)$ , the electric displacement field  $\mathbf{D}_0(\mathbf{F}, \mathbf{E}_0, \theta)$  and the entropy  $\eta(\mathbf{F}, \mathbf{E}_0, \theta)$

must vanish in the absence of deformations (i.e.  $\mathbf{F} = \mathbf{I}$ , with  $\mathbf{I}$  the second order identity tensor), electric fields (i.e.  $\mathbf{E}_0 = \mathbf{0}$ ) and when the temperature is equal to the so-called reference temperature, denoted as  $\theta_R$ . All that is mathematically stated as

$$\begin{aligned}\Psi(\mathbf{F}, \mathbf{E}_0, \theta)|_{\mathbf{I}, \mathbf{0}, \theta_R} &= 0; & \mathbf{P}(\mathbf{F}, \mathbf{E}_0, \theta)|_{\mathbf{I}, \mathbf{0}, \theta_R} &:= \partial_{\mathbf{F}}\Psi(\mathbf{F}, \mathbf{E}_0, \theta)|_{\mathbf{I}, \mathbf{0}, \theta_R} = \mathbf{0} \\ \mathbf{D}_0(\mathbf{F}, \mathbf{E}_0, \theta)|_{\mathbf{I}, \mathbf{0}, \theta_R} &=: \partial_{\mathbf{E}_0}\Psi(\mathbf{F}, \mathbf{E}_0, \theta)|_{\mathbf{I}, \mathbf{0}, \theta_R} = \mathbf{0}; & \eta(\mathbf{F}, \mathbf{E}_0, \theta)|_{\mathbf{I}, \mathbf{0}, \theta_R} &:= \partial_{\theta}\Psi(\mathbf{F}, \mathbf{E}_0, \theta)|_{\mathbf{I}, \mathbf{0}, \theta_R} = 0\end{aligned}\quad (14)$$

Equation (11) establishes the relationship between the first derivatives of the Helmholtz free energy density, namely  $\{\mathbf{P}, \mathbf{D}_0, \eta\}$ , with their work conjugates, namely  $\{\mathbf{F}, \mathbf{E}_0, \theta\}$ , thus closing the system of coupled PDEs in (2.2), governing the behaviour of EAPs. However, the second derivatives of the Helmholtz energy lead also to constitutive tensors with insightful physical relevance, in particular when characterizing the behaviour of the EAP in the linearized regime, i.e. in the vicinity of  $\mathbf{F} \approx \mathbf{I}$ . These can be encompassed within the (symmetric) Hessian of the Helmholtz free energy density, denoted as  $[\mathbb{H}_{\Psi}]$ , namely

$$[\mathbb{H}_{\Psi}] = \begin{bmatrix} \partial_{\mathbf{FF}}^2\Psi & \partial_{\mathbf{FE}_0}^2\Psi & \partial_{\mathbf{F}\theta}^2\Psi \\ \text{sym.} & \partial_{\mathbf{E}_0\mathbf{E}_0}^2\Psi & \partial_{\mathbf{F}\theta}^2\Psi \\ & & \partial_{\theta\theta}^2\Psi \end{bmatrix} \quad (15)$$

where  $\partial_{\mathbf{FF}}^2\Psi$  represents the fourth order elasticity tensor,  $\partial_{\mathbf{FE}_0}^2\Psi$  the third order piezoelectric tensor,  $\partial_{\mathbf{E}_0\mathbf{E}_0}^2\Psi$  represents the second order dielectric tensor, whereas  $\partial_{\mathbf{F}\theta}^2\Psi$  and  $\partial_{\theta\theta}^2\Psi$  are second and first order tensors encoding the influence of the thermal field  $\theta$  on the first Piola-Kirchhoff stress tensor  $\mathbf{P}$  and on the electric displacement field  $\mathbf{D}_0$ . Finally,  $\partial_{\theta\theta}^2\Psi$  can be related with a relevant physical property of a material, in particular, the specific heat capacity, denoted as  $c_v$ , and defined as [? ]

$$c_v(\mathbf{F}, \mathbf{E}_0, \theta) = -\theta\partial_{\theta\theta}^2\Psi(\mathbf{F}, \mathbf{E}_0, \theta) \quad (16)$$

In addition to the physical conditions encompassing the objectivity condition (12), the material symmetry condition (13) and the reference conditions (14), there are mathematical conditions that the Helmholtz free energy density  $\Psi(\mathbf{F}, \mathbf{E}_0, \theta)$  must comply with. In the context of thermo-electro-elasticity, it is accepted that suitable conditions that  $\Psi(\mathbf{F}, \mathbf{E}_0, \theta)$  must satisfy are: rank-one convexity with respect to the deformation gradient  $\mathbf{F}$ , concavity with respect to  $\mathbf{E}_0$ , and concavity with respect to the absolute temperature  $\theta$ , i.e.

$$(\mathbf{u} \otimes \mathbf{V}) : \partial_{\mathbf{FF}}^2\Psi : (\mathbf{u} \otimes \mathbf{V}) \geq 0; \quad \begin{bmatrix} \mathbf{V} \\ \delta\theta \end{bmatrix} : \begin{bmatrix} \partial_{\mathbf{E}_0\mathbf{E}_0}^2\Psi & \partial_{\mathbf{E}_0\theta}^2\Psi \\ \text{sym.} & \partial_{\theta\theta}^2\Psi \end{bmatrix} \begin{bmatrix} \mathbf{V} \\ \delta\theta \end{bmatrix} \leq 0, \quad (17)$$

which must hold for  $\forall \mathbf{u}, \mathbf{V} \in \mathbb{R}^3$ ,  $\delta\theta \in \mathbb{R}^+$ ,  $\{\mathbf{F}, \mathbf{E}_0, \theta\} \in \{\text{GL}^+(3), \mathbb{R}^3, \mathbb{R}^+\}$ . Notice that concavity with respect to  $\theta$  in (17) entails positiveness of the specific heat capacity  $c_v$  in (D.2), whereas the two previous conditions in (17) are related with the concept of material stability and hyperbolicity in the isothermal case [? ].

### 3.2. Alternative thermodynamical potentials

Provided that the Helmholtz free energy density  $\Psi(\mathbf{F}, \mathbf{E}_0, \theta)$  is concave with respect to  $\mathbf{E}_0$  and  $\theta$  (as specified by the second and third conditions in (17)), it becomes possible to define the following three alternative thermodynamic potentials via appropriate Legendre transformations

$$\begin{aligned}e(\mathbf{F}, \mathbf{D}_0, \eta) &= \inf_{\mathbf{E}_0, \theta} \{\Psi(\mathbf{F}, \mathbf{E}_0, \theta) + \mathbf{E}_0 \cdot \mathbf{D}_0 + \theta\eta\} \\ \Upsilon(\mathbf{F}, \mathbf{D}_0, \theta) &= \inf_{\mathbf{E}_0} \{\Psi(\mathbf{F}, \mathbf{E}_0, \theta) + \mathbf{E}_0 \cdot \mathbf{D}_0\} \\ \Gamma(\mathbf{F}, \mathbf{E}_0, \eta) &= \inf_{\theta} \{\Psi(\mathbf{F}, \mathbf{E}_0, \theta) + \theta\eta\},\end{aligned}\quad (18)$$

which permits to establish analogous relationships to those in (11) as

$$\begin{aligned} \mathbf{P} &= \partial_F e(\mathbf{F}, \mathbf{D}_0, \eta); & \mathbf{E}_0 &= \partial_{\mathbf{D}_0} e(\mathbf{F}, \mathbf{D}_0, \eta); & \theta &= \partial_\eta e(\mathbf{F}, \mathbf{D}_0, \eta); \\ \mathbf{P} &= \partial_F \Upsilon(\mathbf{F}, \mathbf{D}_0, \theta); & \mathbf{E}_0 &= \partial_{\mathbf{D}_0} \Upsilon(\mathbf{F}, \mathbf{D}_0, \theta); & \eta &= -\partial_\theta \Upsilon(\mathbf{F}, \mathbf{D}_0, \theta); \\ \mathbf{P} &= \partial_F \Gamma(\mathbf{F}, \mathbf{E}_0, \eta); & \mathbf{D}_0 &= -\partial_{\mathbf{E}_0} \Gamma(\mathbf{F}, \mathbf{E}_0, \eta); & \theta &= \partial_\eta \Gamma(\mathbf{F}, \mathbf{E}_0, \eta). \end{aligned} \quad (19)$$

Obviously, the three new potentials,  $e(\mathbf{F}, \mathbf{D}_0, \eta)$ ,  $\Upsilon(\mathbf{F}, \mathbf{D}_0, \theta)$  and  $\Gamma(\mathbf{F}, \mathbf{D}_0, \eta)$  need to comply with the material frame indifference condition in (12) and with the material symmetry condition in (13). Additionally, in the reference configuration, each of these potentials must comply with the conditions below

$$\begin{cases} e(\mathbf{F}, \mathbf{D}_0, \eta)|_{\mathbf{I}, \mathbf{0}, 0} = 0; & \mathbf{P}(\mathbf{F}, \mathbf{D}_0, \eta)|_{\mathbf{I}, \mathbf{0}, 0} := \partial_{\mathbf{F}} e(\mathbf{F}, \mathbf{D}_0, \eta)|_{\mathbf{I}, \mathbf{0}, 0} = \mathbf{0} \\ \mathbf{E}_0(\mathbf{F}, \mathbf{D}_0, \eta)|_{\mathbf{I}, \mathbf{0}, 0} := \partial_{\mathbf{D}_0} e(\mathbf{F}, \mathbf{D}_0, \eta)|_{\mathbf{I}, \mathbf{0}, 0} = \mathbf{0}; & \theta(\mathbf{F}, \mathbf{D}_0, \eta)|_{\mathbf{I}, \mathbf{0}, 0} := \partial_\eta e(\mathbf{F}, \mathbf{D}_0, \eta)|_{\mathbf{I}, \mathbf{0}, 0} = \theta_R \\ \Upsilon(\mathbf{F}, \mathbf{D}_0, \theta)|_{\mathbf{I}, \mathbf{0}, \theta_R} = 0; & \mathbf{P}(\mathbf{F}, \mathbf{D}_0, \theta)|_{\mathbf{I}, \mathbf{0}, \theta_R} := \partial_{\mathbf{F}} \Upsilon(\mathbf{F}, \mathbf{D}_0, \theta)|_{\mathbf{I}, \mathbf{0}, \theta_R} = \mathbf{0} \\ \mathbf{E}_0(\mathbf{F}, \mathbf{D}_0, \theta)|_{\mathbf{I}, \mathbf{0}, \theta_R} := \partial_{\mathbf{D}_0} \Upsilon(\mathbf{F}, \mathbf{D}_0, \theta)|_{\mathbf{I}, \mathbf{0}, \theta_R} = \mathbf{0}; & \eta(\mathbf{F}, \mathbf{D}_0, \theta)|_{\mathbf{I}, \mathbf{0}, \theta_R} := -\partial_\theta \Upsilon(\mathbf{F}, \mathbf{D}_0, \theta)|_{\mathbf{I}, \mathbf{0}, \theta_R} = 0 \\ \Gamma(\mathbf{F}, \mathbf{D}_0, \eta)|_{\mathbf{I}, \mathbf{0}, 0} = 0; & \mathbf{P}(\mathbf{F}, \mathbf{E}_0, \eta)|_{\mathbf{I}, \mathbf{0}, 0} := \partial_{\mathbf{F}} \Gamma(\mathbf{F}, \mathbf{E}_0, \eta)|_{\mathbf{I}, \mathbf{0}, 0} = \mathbf{0} \\ \mathbf{D}_0(\mathbf{F}, \mathbf{E}_0, \eta)|_{\mathbf{I}, \mathbf{0}, 0} := -\partial_{\mathbf{D}_0} \Gamma(\mathbf{F}, \mathbf{E}_0, \eta)|_{\mathbf{I}, \mathbf{0}, 0} = \mathbf{0}; & \theta(\mathbf{F}, \mathbf{E}_0, \eta)|_{\mathbf{I}, \mathbf{0}, 0} := \partial_\eta \Gamma(\mathbf{F}, \mathbf{E}_0, \eta)|_{\mathbf{I}, \mathbf{0}, 0} = \theta_R \end{cases} \quad (20)$$

Furthermore, provided that  $\Psi(\mathbf{F}, \mathbf{E}_0, \theta)$  is rank-one convex with respect to  $\mathbf{F}$  (i.e. first condition in (17)), the resulting thermodynamical potentials in above (18) would satisfy the following convexity/concavity properties

$$\begin{aligned} \begin{bmatrix} (\mathbf{u} \otimes \mathbf{V}) \\ \mathbf{V}_\perp \\ \delta\eta \end{bmatrix} : \begin{bmatrix} \partial_{\mathbf{FF}}^2 e & \partial_{\mathbf{FD}_0}^2 e & \partial_{\mathbf{F}\eta}^2 e \\ \partial_{\mathbf{FF}}^2 e & \partial_{\mathbf{FD}_0}^2 e & \partial_{\mathbf{F}\eta}^2 e \\ \partial_{\mathbf{FF}}^2 e & \partial_{\mathbf{FD}_0}^2 e & \partial_{\mathbf{F}\eta}^2 e \end{bmatrix} : \begin{bmatrix} (\mathbf{u} \otimes \mathbf{V}) \\ \mathbf{V}_\perp \\ \delta\eta \end{bmatrix} &\geq 0; \\ \begin{bmatrix} (\mathbf{u} \otimes \mathbf{V}) \\ \mathbf{V}_\perp \\ \text{sym.} \end{bmatrix} : \begin{bmatrix} \partial_{\mathbf{FF}}^2 \Upsilon & \partial_{\mathbf{FD}_0}^2 \Upsilon \\ \text{sym.} & \partial_{\mathbf{D}_0 \mathbf{D}_0}^2 \Upsilon \end{bmatrix} : \begin{bmatrix} (\mathbf{u} \otimes \mathbf{V}) \\ \mathbf{V}_\perp \end{bmatrix} &\geq 0; \quad \partial_{\theta\theta}^2 \Upsilon \leq 0; \\ \begin{bmatrix} (\mathbf{u} \otimes \mathbf{V}) \\ \delta\eta \\ \text{sym.} \end{bmatrix} : \begin{bmatrix} \partial_{\mathbf{FF}}^2 \Gamma & \partial_{\mathbf{F}\eta}^2 \Gamma \\ \text{sym.} & \partial_{\eta\eta}^2 \Gamma \end{bmatrix} : \begin{bmatrix} (\mathbf{u} \otimes \mathbf{V}) \\ \delta\eta \end{bmatrix} &\geq 0; \quad \mathbf{V} \cdot \partial_{\mathbf{E}_0 \mathbf{E}_0}^2 \Gamma \mathbf{V} \geq 0, \end{aligned} \quad (21)$$

which must hold for

$$\begin{aligned} \mathbf{u}, \mathbf{V}, \mathbf{V}_\perp &\in \mathbb{R}^3, \delta\eta \in \mathbb{R}, & \{\mathbf{F}, \mathbf{D}_0, \eta\} &\in \{\text{GL}^+(3), \mathbb{R}^3, \mathbb{R}\} \\ \mathbf{u}, \mathbf{V}, \mathbf{V}_\perp &\in \mathbb{R}^3, & \{\mathbf{F}, \mathbf{D}_0, \theta\} &\in \{\text{GL}^+(3), \mathbb{R}^3, \mathbb{R}^+\} \\ \mathbf{u}, \mathbf{V} &\in \mathbb{R}^3, \delta\eta \in \mathbb{R}, & \{\mathbf{F}, \mathbf{E}_0, \eta\} &\in \{\text{GL}^+(3), \mathbb{R}^3, \mathbb{R}\}, \end{aligned} \quad (22)$$

respectively, where  $\mathbf{V}_\perp$  is such that  $\mathbf{V}_\perp \cdot \mathbf{V} = 0$ . Above conditions, in conjunction with (17) dictate that the four potentials, namely  $\Psi(\mathbf{F}, \mathbf{E}_0, \theta)$ ,  $e(\mathbf{F}, \mathbf{D}_0, \eta)$ ,  $\Upsilon(\mathbf{F}, \mathbf{D}_0, \theta)$  and  $\Gamma(\mathbf{F}, \mathbf{E}_0, \theta)$ , in the vicinity of the reference configuration, namely  $\mathbf{F} \approx \mathbf{I}$ ,  $\mathbf{E}_0 \approx \mathbf{0}$  and  $\theta \approx \theta_R$ , will adopt the convexity/concavity properties displayed in Figure (2).

As discussed in [?], defining phenomenological thermodynamic potentials that must satisfy both rank-one convexity and concavity conditions-such as  $\Psi(\mathbf{F}, \mathbf{E}_0, \theta)$ ,  $\Upsilon(\mathbf{F}, \mathbf{D}_0, \theta)$ , and  $\Gamma(\mathbf{F}, \mathbf{E}_0, \eta)$ -is generally more challenging than when the potential is only required to be rank-one convex or convex with respect to all its arguments, as is the case with the internal energy  $e(\mathbf{F}, \mathbf{D}_0, \eta)$ . Motivated by this simplification, the authors in [?] aimed to define constitutive models for the internal energy of EAPs within the framework of isothermal electro-mechanics. This was achieved by extending the concept of polyconvexity, originally from hyperelasticity (purely mechanical systems), to this multi-physics context. Indeed, a sufficient condition for ensuring the rank-one convexity of  $e(\mathbf{F}, \mathbf{D}_0, \eta)$ , as shown in equation (21), can be fulfilled through

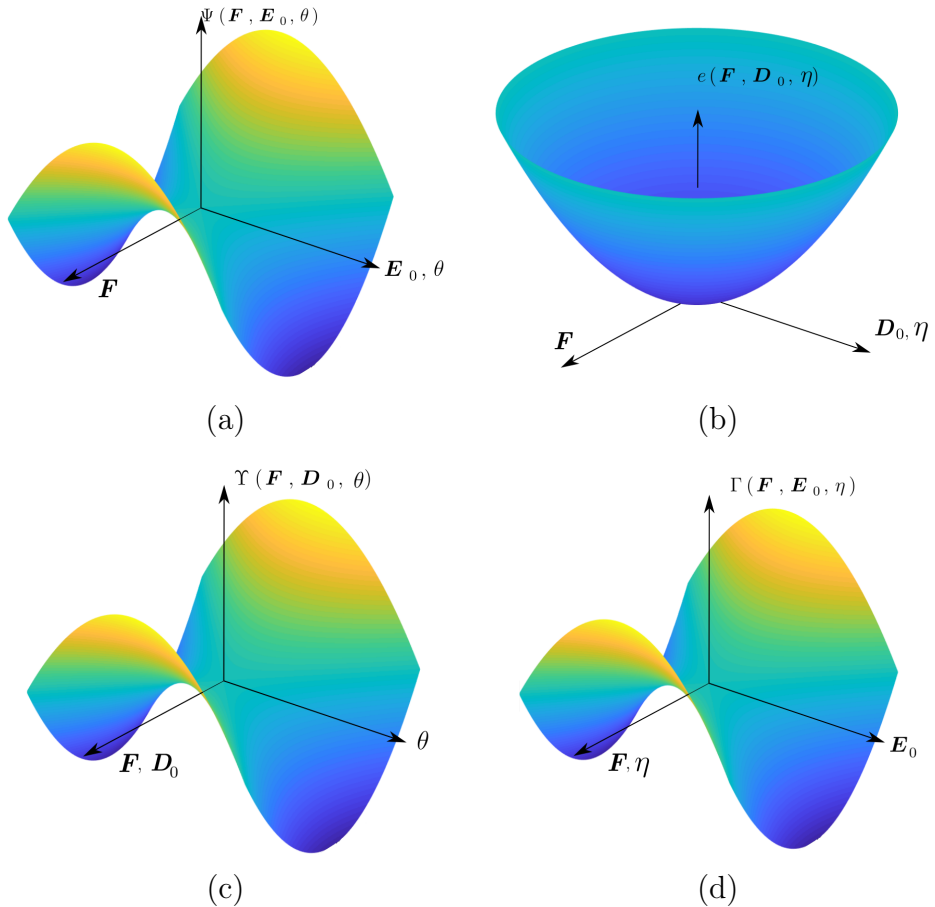


Figure 2: Convexity/concavity properties of the various thermodynamical potentials  $\Psi(\mathbf{F}, \mathbf{E}_0, \theta)$ ,  $e(\mathbf{F}, \mathbf{D}_0, \eta)$ ,  $\Upsilon(\mathbf{F}, \mathbf{D}_0, \theta)$  and  $\Gamma(\mathbf{F}, \mathbf{E}_0, \eta)$  in the vicinity of the reference configuration (i.e.  $\mathbf{F} \approx \mathbf{I}$ ,  $\mathbf{E}_0 \approx \mathbf{0}$  and  $\theta \approx \theta_R$ ). Specifically, we observe:  $\Psi(\mathbf{F}, \mathbf{E}_0, \theta)$  is convex with respect to  $\mathbf{F}$  and concave with respect to  $\{\mathbf{E}_0, \theta\}$ ;  $e(\mathbf{F}, \mathbf{D}_0, \eta)$  is convex with respect to  $\{\mathbf{F}, \mathbf{D}_0, \eta\}$ ;  $\Upsilon(\mathbf{F}, \mathbf{D}_0, \theta)$  is convex with respect to  $\{\mathbf{F}, \mathbf{D}_0\}$  and concave with respect to  $\theta$ ;  $\Gamma(\mathbf{F}, \mathbf{E}_0, \eta)$  is convex with respect to  $\{\mathbf{F}, \eta\}$  and concave with respect to  $\mathbf{E}_0$ .

the polyconvexity of  $e(\mathbf{F}, \mathbf{D}_0, \eta)$ . For this purpose, we assume the existence of a function  $\mathbb{W}$  such that:

$$\mathbb{W} : \mathrm{GL}^+(3) \times \mathrm{GL}^+(3) \times \mathbb{R}^+ \times \mathbb{R}^3 \times \mathbb{R}^3 \times \mathbb{R}, \quad (\mathbf{F}, \mathbf{H}, J, \mathbf{D}_0, \mathbf{d}, \eta) \rightarrow \mathbb{W}(\mathbf{F}, \mathbf{H}, J, \mathbf{D}_0, \mathbf{d}, \eta) \quad (23)$$

where  $\mathbf{H}$  and  $J$  are the co-factor and determinant of  $\mathbf{F}$ , defined in (1) and (2), whilst  $\mathbf{d}$  is a field obtained as  $\mathbf{d} = \mathbf{F}\mathbf{D}_0$ . Then,  $e(\mathbf{F}, \mathbf{D}_0, \eta)$  is said to be polyconvex [1, 3, 4] if it can be equivalently written as

$$e(\mathbf{F}, \mathbf{D}_0, \eta) = \mathbb{W}(\mathbf{F}, \mathbf{H}, J, \mathbf{D}_0, \mathbf{d}, \eta) \quad (24)$$

where  $\mathbb{W}(\mathbf{F}, \mathbf{H}, J, \mathbf{D}_0, \mathbf{d}, \eta)$  must be convex with respect to all its arguments. For twice-differentiable functions, convexity of  $\mathbb{W}(\mathbf{F}, \mathbf{H}, J, \mathbf{D}_0, \mathbf{d}, \eta)$  is equivalent to positive definiteness of its Hessian operator  $[\mathbb{H}_{\mathbb{W}}]$ , i.e.

$$\delta \mathcal{V}^T : [\mathbb{H}_{\mathbb{W}}] : \delta \mathcal{V} \geq 0, \quad \forall \delta \mathcal{V} = [\delta \mathbf{F} \quad \delta \mathbf{H} \quad \delta J \quad \delta \mathbf{D}_0 \quad \delta \mathbf{d} \quad \delta \eta]^T, \quad (25)$$

where the (symmetric) Hessian operator  $[\mathbb{H}_{\mathbb{W}}]$  incorporates all the second derivatives of  $\mathbb{W}$ , i.e.

$$[\mathbb{H}_{\mathbb{W}}] = \begin{bmatrix} \partial_{\mathbf{FF}}^2 \mathbb{W} & \partial_{\mathbf{FH}}^2 \mathbb{W} & \partial_{\mathbf{FJ}}^2 \mathbb{W} & \partial_{\mathbf{FD}_0}^2 \mathbb{W} & \partial_{\mathbf{Fd}}^2 \mathbb{W} & \partial_{\mathbf{F}\eta}^2 \mathbb{W} \\ & \partial_{\mathbf{HH}}^2 \mathbb{W} & \partial_{\mathbf{HJ}}^2 \mathbb{W} & \partial_{\mathbf{HD}_0}^2 \mathbb{W} & \partial_{\mathbf{Hd}}^2 \mathbb{W} & \partial_{\mathbf{H}\eta}^2 \mathbb{W} \\ & & \partial_{\mathbf{JJ}}^2 \mathbb{W} & \partial_{\mathbf{JD}_0}^2 \mathbb{W} & \partial_{\mathbf{Jd}}^2 \mathbb{W} & \partial_{\mathbf{J}\eta}^2 \mathbb{W} \\ & & & \partial_{\mathbf{D}_0\mathbf{D}_0}^2 \mathbb{W} & \partial_{\mathbf{D}_0\mathbf{d}}^2 \mathbb{W} & \partial_{\mathbf{D}_0\eta}^2 \mathbb{W} \\ & \text{sym.} & & & \partial_{\mathbf{dd}}^2 \mathbb{W} & \partial_{\mathbf{d}\eta}^2 \mathbb{W} \\ & & & & & \partial_{\eta\eta}^2 \mathbb{W} \end{bmatrix} \quad (26)$$

### 3.3. Invariant-based thermo-electro-mechanics

A simple manner to accommodate the principle of objectivity or material frame indifference and the requirement of material symmetry is through the dependence of any of the thermodynamical potentials, namely  $\Psi(\mathbf{F}, \mathbf{E}_0, \theta)$ ,  $e(\mathbf{F}, \mathbf{D}_0, \eta)$ ,  $\Upsilon(\mathbf{F}, \mathbf{D}_0, \theta)$  or  $\Gamma(\mathbf{F}, \mathbf{E}_0, \eta)$  with respect to invariants of the right Cauchy-Green deformation gradient tensor  $\mathbf{C} = \mathbf{F}^T \mathbf{F}$ ,  $\mathbf{E}_0$  or  $\mathbf{D}_0$  and also with respect to  $\theta$  or  $\eta$ . Let us denote as  $\mathbf{I}_{\Psi}$ ,  $\mathbf{I}_e$ ,  $\mathbf{I}_{\Upsilon}$  and  $\mathbf{I}_{\Gamma}$  the set of electro-mechanical objective invariants of  $\Psi(\mathbf{F}, \mathbf{E}_0, \theta)$ ,  $e(\mathbf{F}, \mathbf{D}_0, \eta)$ ,  $\Upsilon(\mathbf{F}, \mathbf{D}_0, \theta)$  or  $\Gamma(\mathbf{F}, \mathbf{E}_0, \eta)$ , respectively, required to characterise a given material symmetry group  $\mathcal{G}$ . Then, it is possible to express the four thermodynamical potentials equivalently as

$$\begin{aligned} \Psi(\mathbf{F}, \mathbf{E}_0, \theta) &= \mathbb{U}_{\Psi}(\mathbf{I}_{\Psi}(\mathbf{C}, \mathbf{E}_0), \theta); & e(\mathbf{F}, \mathbf{D}_0, \eta) &= \mathbb{U}_e(\mathbf{I}_e(\mathbf{C}, \mathbf{D}_0), \eta); \\ \Upsilon(\mathbf{F}, \mathbf{D}_0, \theta) &= \mathbb{U}_{\Upsilon}(\mathbf{I}_{\Upsilon}(\mathbf{C}, \mathbf{D}_0), \theta); & \Gamma(\mathbf{F}, \mathbf{E}_0, \eta) &= \mathbb{U}_{\Gamma}(\mathbf{I}_{\Gamma}(\mathbf{C}, \mathbf{E}_0), \eta). \end{aligned} \quad (27)$$

Application of the chain rule into equation (11) or (19) permits of obtain the first Piola-Kirchhoff stress tensor  $\mathbf{P}$ ,  $\mathbf{D}_0$  or  $\mathbf{E}_0$ , and  $\theta$  or  $\eta$  in terms of the derivatives of above invariant-based potentials with respect to their arguments

$$\begin{aligned} \mathbf{P} &= \sum_{i=1}^n \left( \partial_{I_{\Psi_i}} \mathbb{U}_{\Psi} \right) \partial_{\mathbf{F}} I_{\Psi_i}; & \mathbf{D}_0 &= - \sum_{i=1}^n \left( \partial_{I_{\Psi_i}} \mathbb{U}_{\Psi} \right) \partial_{\mathbf{E}_0} I_{\Psi_i}; & \eta &= -\partial_{\theta} \mathbb{U}_{\Psi} \\ \mathbf{P} &= \sum_{i=1}^n \left( \partial_{I_{e_i}} \mathbb{U}_e \right) \partial_{\mathbf{F}} I_{e_i}; & \mathbf{E}_0 &= \sum_{i=1}^n \left( \partial_{I_{e_i}} \mathbb{U}_e \right) \partial_{\mathbf{D}_0} I_{e_i}; & \theta &= \partial_{\eta} \mathbb{U}_e \\ \mathbf{P} &= \sum_{i=1}^n \left( \partial_{I_{\Upsilon_i}} \mathbb{U}_{\Upsilon} \right) \partial_{\mathbf{F}} I_{\Upsilon_i}; & \mathbf{E}_0 &= \sum_{i=1}^n \left( \partial_{I_{\Upsilon_i}} \mathbb{U}_{\Upsilon} \right) \partial_{\mathbf{D}_0} I_{\Upsilon_i}; & \eta &= -\partial_{\theta} \mathbb{U}_{\Upsilon} \\ \mathbf{P} &= \sum_{i=1}^n \left( \partial_{I_{\Gamma_i}} \mathbb{U}_{\Gamma} \right) \partial_{\mathbf{F}} I_{\Gamma_i}; & \mathbf{D}_0 &= - \sum_{i=1}^n \left( \partial_{I_{\Gamma_i}} \mathbb{U}_{\Gamma} \right) \partial_{\mathbf{E}_0} I_{\Gamma_i}; & \theta &= \partial_{\eta} \mathbb{U}_{\Gamma} \end{aligned} \quad (28)$$

### 3.3.1. Electro-mechanical invariants for isotropy

For the case of isotropy, the invariants required to characterise this material symmetry group for the thermodynamical potentials depending on  $\mathbf{E}_0$ , namely  $\Psi(\mathbf{F}, \mathbf{E}_0, \theta)$  and  $\Gamma(\mathbf{F}, \mathbf{E}_0, \eta)$ , and the first derivatives of the latter with respect to  $\mathbf{F}$  and  $\mathbf{E}_0$  (featuring in the definition of  $\mathbf{P}$  and  $\mathbf{D}_0$  in (28)) are

$$\begin{aligned} I_{\Psi_1} &:= \mathbf{F} : \mathbf{F} = \text{tr}(\mathbf{C}), & \partial_{\mathbf{F}} I_{\Psi_1} &= 2\mathbf{F}, & \partial_{\mathbf{D}_0} I_{\Psi_1} &= \mathbf{0} \\ I_{\Psi_2} &:= \mathbf{H} : \mathbf{H} = \text{tr}(\text{Cof}\mathbf{C}), & \partial_{\mathbf{F}} I_{\Psi_2} &= 2\mathbf{H} \times \mathbf{F}, & \partial_{\mathbf{E}_0} I_{\Psi_2} &= \mathbf{0} \\ I_{\Psi_3} &:= J = (\det \mathbf{C})^{1/2}, & \partial_{\mathbf{F}} I_{\Psi_3} &= \mathbf{H}, & \partial_{\mathbf{D}_0} I_{\Psi_3} &= 0 \\ I_{\Psi_4} &:= \mathbf{E}_0 \cdot \mathbf{E}_0, & \partial_{\mathbf{F}} I_{\Psi_4} &= \mathbf{0}, & \partial_{\mathbf{E}_0} I_{\Psi_4} &= 2\mathbf{E}_0 \\ I_{\Psi_5} &:= \mathbf{H}\mathbf{E}_0 \cdot \mathbf{H}\mathbf{E}_0 = \mathbf{E}_0 \cdot \text{Cof}\mathbf{C}\mathbf{E}_0, & \partial_{\mathbf{F}} I_{\Psi_5} &= (2\mathbf{H}\mathbf{E}_0 \otimes \mathbf{E}_0) \times \mathbf{F}, & \partial_{\mathbf{E}_0} I_{\Psi_5} &= 2\text{Cof}\mathbf{C}\mathbf{E}_0 \end{aligned} \quad (29)$$

with  $I_{\Psi_i} = I_{\Gamma_i}$ , for  $i = \{1, \dots, 5\}$ . On the other hand, for the thermodynamical potentials depending on  $\mathbf{D}_0$ , namely  $e(\mathbf{F}, \mathbf{D}_0, \eta)$  and  $\Upsilon(\mathbf{F}, \mathbf{D}_0, \theta)$ , the invariants and their first derivatives with respect to  $\mathbf{F}$  and  $\mathbf{D}_0$  (featuring in the definition of  $\mathbf{P}$  and  $\mathbf{E}_0$  in (28)) have been chosen to be

$$\begin{aligned} I_{e_1} &:= \mathbf{F} : \mathbf{F} = \text{tr}(\mathbf{C}), & \partial_{\mathbf{F}} I_{e_1} &= 2\mathbf{F}, & \partial_{\mathbf{D}_0} I_{e_1} &= \mathbf{0} \\ I_{e_2} &:= \mathbf{H} : \mathbf{H} = \text{tr}(\text{Cof}\mathbf{C}), & \partial_{\mathbf{F}} I_{e_2} &= 2\mathbf{H} \times \mathbf{F}, & \partial_{\mathbf{D}_0} I_{e_2} &= \mathbf{0} \\ I_{e_3} &:= J = (\det \mathbf{C})^{1/2}, & \partial_{\mathbf{F}} I_{e_3} &= \mathbf{H}, & \partial_{\mathbf{D}_0} I_{e_3} &= 0 \\ I_{e_4} &:= \mathbf{D}_0 \cdot \mathbf{D}_0, & \partial_{\mathbf{F}} I_{e_4} &= \mathbf{0}, & \partial_{\mathbf{D}_0} I_{e_4} &= 2\mathbf{D}_0 \\ I_{e_5} &:= \mathbf{F}\mathbf{D}_0 \cdot \mathbf{F}\mathbf{D}_0 = \mathbf{D}_0 \cdot \mathbf{C}\mathbf{D}_0, & \partial_{\mathbf{F}} I_{e_5} &= 2\mathbf{F}\mathbf{D}_0 \otimes \mathbf{D}_0, & \partial_{\mathbf{D}_0} I_{e_5} &= 2\mathbf{C}\mathbf{D}_0, \end{aligned} \quad (30)$$

with  $I_{e_i} = I_{\Upsilon_i}$ , for  $i = \{1, \dots, 5\}$ .

### 3.3.2. Electro-mechanical invariants for transversely isotropy

In the context of transverse isotropy, a preferred direction  $\mathbf{N}$  emerges, perpendicular to the material's plane of isotropy, imparting anisotropic characteristics. Our focus centers on the material symmetry group  $\mathcal{D}_{\infty h}$  [?], where the structural tensor takes the form  $\mathbf{N} \otimes \mathbf{N}$ . This group is distinct from  $\mathcal{C}_{\infty}$ , also present in transversely isotropic materials, characterized by the structural vector  $\mathbf{N}$  and encompassing the potential for piezoelectricity. The  $\mathcal{D}_{\infty h}$  group, beyond the invariants  $\{I_1, I_2, I_3, I_4, I_5\}$  in (29), is distinguished by three additional invariants, which for the case of the thermodynamical potentials  $\Psi(\mathbf{F}, \mathbf{E}_0, \theta)$  and  $\Gamma(\mathbf{F}, \mathbf{E}_0, \eta)$  are detailed below

$$\begin{aligned} I_{\Psi_6} &= \mathbf{F}\mathbf{N} \cdot \mathbf{F}\mathbf{N} = \text{tr}(\mathbf{CN} \otimes \mathbf{C}), & \partial_{\mathbf{F}} I_{\Psi_6} &= 2\mathbf{FN} \otimes \mathbf{N}, & \partial_{\mathbf{E}_0} I_{\Psi_6} &= \mathbf{0} \\ I_{\Psi_7} &= \mathbf{HN} \cdot \mathbf{HN} = \text{tr}(\text{Cof}\mathbf{C}), & \partial_{\mathbf{F}} I_{\Psi_7} &= 2(\mathbf{HN} \otimes \mathbf{N}) \times \mathbf{F}, & \partial_{\mathbf{E}_0} I_{\Psi_7} &= \mathbf{0} \\ I_{\Psi_8} &= (\mathbf{E}_0 \cdot \mathbf{N})^2, & \partial_{\mathbf{F}} I_{\Psi_8} &= \mathbf{0}, & \partial_{\mathbf{E}_0} I_{\Psi_8} &= 2(\mathbf{E}_0 \cdot \mathbf{N})\mathbf{N}, \end{aligned} \quad (31)$$

with  $I_{\Psi_i} = I_{\Gamma_i}$ , for  $i = \{1, \dots, 8\}$ . On the other hand, for the thermodynamical potentials depending on  $\mathbf{D}_0$ , namely  $e(\mathbf{F}, \mathbf{D}_0, \eta)$  and  $\Upsilon(\mathbf{F}, \mathbf{D}_0, \theta)$ , the invariants and their first derivatives with respect to  $\mathbf{F}$  and  $\mathbf{D}_0$  (featuring in the definition of  $\mathbf{P}$  and  $\mathbf{E}_0$  in (28)), in addition to those in (30), have been chosen to be

$$\begin{aligned} I_{\Psi_6} &= \mathbf{FN} \cdot \mathbf{FN} = \text{tr}(\mathbf{CN} \otimes \mathbf{C}), & \partial_{\mathbf{F}} I_{\Psi_6} &= 2\mathbf{FN} \otimes \mathbf{N}, & \partial_{\mathbf{D}_0} I_{\Psi_6} &= \mathbf{0} \\ I_{\Psi_7} &= \mathbf{HN} \cdot \mathbf{HN} = \text{tr}(\text{Cof}\mathbf{C}), & \partial_{\mathbf{F}} I_{\Psi_7} &= 2(\mathbf{HN} \otimes \mathbf{N}) \times \mathbf{F}, & \partial_{\mathbf{D}_0} I_{\Psi_7} &= \mathbf{0} \\ I_{\Psi_8} &= (\mathbf{D}_0 \cdot \mathbf{N})^2, & \partial_{\mathbf{F}} I_{\Psi_8} &= \mathbf{0}, & \partial_{\mathbf{D}_0} I_{\Psi_8} &= 2(\mathbf{D}_0 \cdot \mathbf{N})\mathbf{N}, \end{aligned} \quad (32)$$

with  $I_{e_i} = I_{\Upsilon_i}$ , for  $i = \{1, \dots, 8\}$ .

### 3.4. The ground truth thermo-electro-mechanical Helmholtz free energy free density

In this study, we will calibrate our neural network-based constitutive models using a series of in-silico datasets derived from various ground truth constitutive models. Each of these models will be formulated based on a Helmholtz free energy density that shares a common structural framework, as established by the seminal work of XX in the domain of thermomechanics, and further extended by XX in the context of thermo-electromechanics. Consequently, all ground truth models will be defined in accordance with the following decomposition:

$$\Psi(\mathbf{F}, \mathbf{E}_0, \theta) = \mathcal{F}(\theta) \left( \Psi_m(\mathbf{F}) + \Psi_{em}(\mathbf{F}, \mathbf{E}_0) \right) + \Psi_\theta(\theta) + \left( 1 - \frac{\theta}{\theta_R} \right) \Gamma_R(J), \quad (33)$$

- The sum of  $\Psi_m(\mathbf{F})$  and  $\Psi_{em}(\mathbf{F}, \mathbf{E}_0)$  corresponds with the Helmholtz free energy density in particular isothermal case when  $\theta = \theta_R$ .
- $\Gamma_R(J)$  corresponds with the thermodynamical potential  $\Gamma(\mathbf{F}, \mathbf{E}_0, \eta)$  at the reference temperature, i.e.  $\theta = \theta_R$ . In general,  $\Gamma_R$  could be a function of both  $\mathbf{F}$  and  $\mathbf{E}_0$ . However, following XX, we only allow for a dependence of  $\Gamma_R$  with respect to the volumetric part of  $\mathbf{F}$  according to

$$\Gamma_R(J) = \alpha_0 \kappa_0 (J - 1) \theta_R \quad (34)$$

where  $\alpha_0$  and  $\kappa_0$  refer to the thermal expansion coefficient and the bulk modulus of the material in the reference configuration.

- The function  $\mathcal{F}(\theta)$  is introduced to incorporate a nonlinear dependence of stresses with respect to the thermal field. Following XX, we advocate for the following definition of  $\mathcal{F}(\theta)$

$$\mathcal{F}(\theta) = \left( \frac{\theta}{\theta_R} + g(\theta) - g(\theta_R) + \partial_\theta g|_{\theta_R} (\theta_R - \theta) \right) \quad (35)$$

where  $g(\theta)$  is a nonlinear function of  $\theta$ . In this work, we have made use of the following definition for  $g(\theta)$

$$g(\theta) = b \left( \frac{\theta}{\theta_R} \right)^a \quad (36)$$

The nonlinearity of stresses with respect to the thermal field can indeed be observed computing the second derivative of  $\mathbf{P}$  (11) with respect to  $\theta$ , yielding

$$\partial_{\theta\theta}^2 \mathbf{P} = \mathcal{F}''(\theta) \left( \partial_{\mathbf{F}} \Psi_m(\mathbf{F}) + \partial_{\mathbf{F}} \Psi_{em}(\mathbf{F}, \mathbf{E}_0) \right) \neq \mathbf{0} \iff \mathcal{F}''(\theta) \neq 0 \quad (37)$$

Provided that  $\mathcal{F}(\theta)'' = g(\theta)''$  is a nonlinear function, in general its second derivative with respect to  $\theta$  would not vanish and hence,  $\mathbf{P}$  will have a nonlinear character with respect to  $\theta$ . Figure 3<sub>a</sub> illustrates the nonlinear behaviour of  $\mathbf{P}$  for various values of the coefficients  $a$  and  $b$  in the function  $g(\theta)$  in (36), having fixed  $\mathbf{F}$  and  $\mathbf{E}_0$  according to

$$\mathbf{F} = \begin{bmatrix} 1.8 & 0 & 0 \\ 0 & 1 & 0 \\ 0 & 0 & 1/1.8 \end{bmatrix}; \quad \mathbf{E}_0 = \mathbf{0} \quad (38)$$

- The purely temperature dependent contribution  $\Psi_\theta(\theta)$  is defined as

$$\Psi_\theta = c_{vR} \left( \theta - \theta_R - \theta \log \frac{\theta}{\theta_R} \right) \quad (39)$$

where  $c_{vR}$  represents the specific heat capacity at the reference configuration. At any other configuration, the specific heat capacity  $c_v(\mathbf{F}, \mathbf{E}_0, \theta)$  is obtained by means of equation (D.2), yielding

$$\begin{aligned} c_v(\mathbf{F}, \mathbf{E}_0, \theta) &= -\theta \left( \Psi_m(\mathbf{F}) + \Psi_{em}(\mathbf{F}, \mathbf{E}_0) \right) \mathcal{F}''(\theta) - \theta \partial_{\theta\theta}^2 \Psi_\theta \\ &= -\theta \left( \Psi_m(\mathbf{F}) + \Psi_{em}(\mathbf{F}, \mathbf{E}_0) \right) g''(\theta) + c_{vR}, \end{aligned} \quad (40)$$

where use of (35) has been made in (40). Substituting at the reference configuration, i.e.  $\{\mathbf{F}, \mathbf{E}_0, \theta\} = \{\mathbf{I}, \mathbf{0}, \theta_R\}$ , the specific heat capacity coincides indeed with  $c_{vR}$ , i.e.

$$c_v|_{\mathbf{I}, \mathbf{0}, \theta_R} = -\theta_R \underbrace{\left( \Psi_m(\mathbf{F})|_{\mathbf{I}} + \Psi_{em}(\mathbf{F}, \mathbf{E}_0)|_{\mathbf{I}, \mathbf{0}} \right)}_{=0} g''(\theta)|_{\theta_R} + c_{vR} \quad (41)$$

where the isothermal electro-mechanical Helmholtz energy density (underbraced term) must vanish by construction in the reference configuration, hence obtaining  $c_v|_{\mathbf{I}, \mathbf{0}, \theta_R} = c_{vR}$ . It is worth noticing from equation (40) that the model advocated for allows for a nonlinear dependence of the specific heat capacity  $c_v$  with respect to the deformation and electric field, and also with respect to temperature. This combined nonlinear dependence is reflected in Figure 3b, where the deformation gradient tensor  $\mathbf{F}$  and electric field  $\mathbf{E}_0$  have been fixed to the same values as in equation (38).

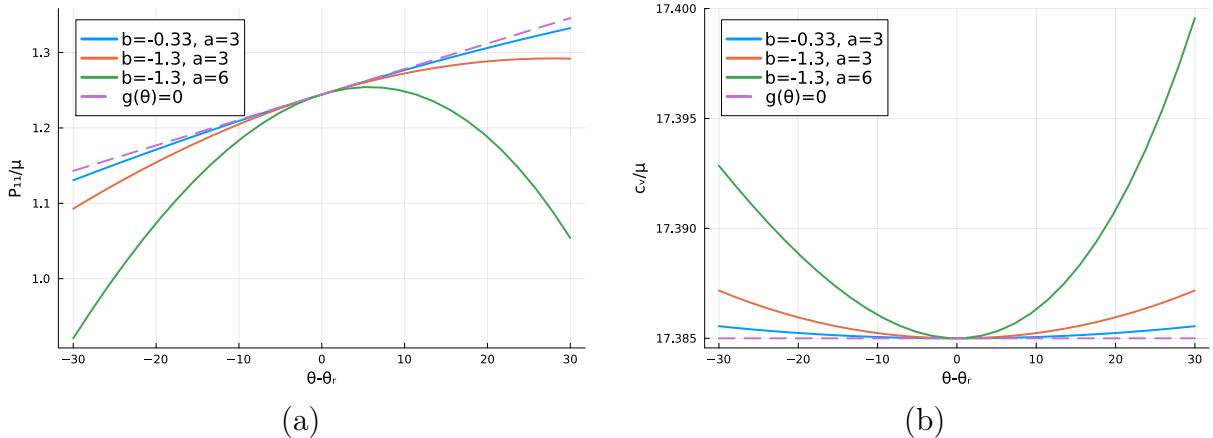


Figure 3: a) Nonlinear behaviour of stress (component 11 of  $\mathbf{P}$ ) with respect to temperature; b) Nonlinear behaviour of  $c_v$  with respect to  $\theta$ . In both cases  $\mathbf{F}$  and  $\mathbf{E}_0$  have been fixed to the values given in (38) where the purely mechanical and electro-mechanical isothermal potential,  $\Psi_m$  and  $\Psi_{em}$  correspond with a Mooney-Rivlin model and an ideal dielectric elastomer model, respectively.

### 3.5. Specific forms of $\Psi_m(\mathbf{F})$ and $\Psi_{em}(\mathbf{F}, \mathbf{E}_0)$

In the generic expression of the Helmholtz energy density,  $\Psi(\mathbf{F}, \mathbf{E}_0, \theta)$ , as presented in equation (33), we have systematically defined all terms except for  $\Psi_m(\mathbf{F})$  and  $\Psi_{em}(\mathbf{F}, \mathbf{E}_0)$ . For these two potentials, we have explored a broad spectrum of models that characterize the constitutive behavior of ideal dielectric elastomers under isothermal conditions. Specifically, for the purely mechanical contribution  $\Psi_m(\mathbf{F})$ , we have examined various hyperelastic potentials listed in Table 1, which include: Mooney-Rivlin model; Quadratic Mooney-Rivlin model; Gent model; Yeoh

Mechanical isothermal Helmholtz free energy $\Psi_m$																										
Name of the model	Invariant representation																									
Mooney-Rivlin (MR)	$\mathbb{U}_\Psi = \frac{\mu_1}{2} (I_{\Psi_1} - 3) + \frac{\mu_2}{2} (I_{\Psi_2} - 3) - (\mu_1 + 2\mu_2) \ln(I_{\Psi_3}) + \frac{\lambda}{2} (I_{\Psi_3} - 1)^2$																									
	<table border="1"> <thead> <tr> <th>Parameter:</th><th><math>\mu_1</math></th><th><math>\mu_2</math></th><th><math>\lambda</math></th><th><math>\varepsilon</math></th><th></th><th></th><th></th></tr> </thead> <tbody> <tr> <td>Value:</td><td>0.5</td><td>0.5</td><td>5</td><td>1</td><td></td><td></td><td></td></tr> </tbody> </table>							Parameter:	$\mu_1$	$\mu_2$	$\lambda$	$\varepsilon$				Value:	0.5	0.5	5	1						
Parameter:	$\mu_1$	$\mu_2$	$\lambda$	$\varepsilon$																						
Value:	0.5	0.5	5	1																						
Quadratic MR (QMR)	$\mathbb{U}_\Psi = \frac{\mu_1}{2} (I_{\Psi_1})^2 + \frac{\mu_2}{2} (I_{\Psi_2})^2 - 6(\mu_1 + 2\mu_2) \ln(I_{\Psi_3}) + \frac{\lambda}{2} (I_{\Psi_3} - 1)^2$																									
	<table border="1"> <thead> <tr> <th>Parameter:</th><th><math>\mu_1</math></th><th><math>\mu_2</math></th><th><math>\lambda</math></th><th><math>\varepsilon</math></th><th></th><th></th><th></th></tr> </thead> <tbody> <tr> <td>Value:</td><td>0.5</td><td>0.5</td><td>5</td><td>1</td><td></td><td></td><td></td></tr> </tbody> </table>							Parameter:	$\mu_1$	$\mu_2$	$\lambda$	$\varepsilon$				Value:	0.5	0.5	5	1						
Parameter:	$\mu_1$	$\mu_2$	$\lambda$	$\varepsilon$																						
Value:	0.5	0.5	5	1																						
Gent (G)	$\mathbb{U}_\Psi = -\frac{\mu}{2} J_m \ln \left( 1 - \frac{I_{\Psi_1} - 3}{J_m} \right) - \mu \ln(I_{\Psi_3}) + \frac{\lambda}{2} (I_{\Psi_3} - 1)^2$																									
	<table border="1"> <thead> <tr> <th>Parameter:</th><th><math>\mu</math></th><th><math>J_m</math></th><th><math>\lambda</math></th><th><math>\varepsilon</math></th><th></th><th></th><th></th></tr> </thead> <tbody> <tr> <td>Value:</td><td>1</td><td>19</td><td>5</td><td>1</td><td></td><td></td><td></td></tr> </tbody> </table>							Parameter:	$\mu$	$J_m$	$\lambda$	$\varepsilon$				Value:	1	19	5	1						
Parameter:	$\mu$	$J_m$	$\lambda$	$\varepsilon$																						
Value:	1	19	5	1																						
Yeoh (Y)	$\mathbb{U}_\Psi = C_{10} (I_{\Psi_1} - 3) + C_{20} (I_{\Psi_1} - 3)^2 + C_{30} (I_{\Psi_1} - 3)^3 - 2C_{10} \ln(I_{\Psi_3}) + \frac{\lambda}{2} (I_{\Psi_3} - 1)^2$																									
	<table border="1"> <thead> <tr> <th>Parameter:</th><th><math>C_{10}</math></th><th><math>C_{20}</math></th><th><math>C_{30}</math></th><th><math>\lambda</math></th><th><math>\varepsilon</math></th><th></th><th></th></tr> </thead> <tbody> <tr> <td>Value:</td><td>1</td><td>1</td><td>1</td><td>5</td><td>1</td><td></td><td></td></tr> </tbody> </table>							Parameter:	$C_{10}$	$C_{20}$	$C_{30}$	$\lambda$	$\varepsilon$			Value:	1	1	1	5	1					
Parameter:	$C_{10}$	$C_{20}$	$C_{30}$	$\lambda$	$\varepsilon$																					
Value:	1	1	1	5	1																					
Arruda-Boyce (AB)	$\mathbb{U}_\Psi = a_1 \left( \beta(I_{\Psi_1}) \lambda_c(I_{\Psi_1}) - a_2 \ln \left( \frac{\sinh(\beta(I_{\Psi_1}))}{\beta(I_{\Psi_1})} \right) \right) - A \ln(I_{\Psi_3}) + \frac{\lambda}{2} (I_{\Psi_3} - 1)^2 + B$ $\lambda_c(I_{\Psi_1}) = \sqrt{\frac{1}{3}} \sqrt{I_{\Psi_1}}; \quad \mathcal{L}^{-1}(x) = \frac{3x - x^3}{1 - x^2}; \quad \beta(I_1) = \mathcal{L}^{-1}\left(\frac{\lambda_c(I_{\Psi_1})}{a_2}\right)$																									
	<table border="1"> <thead> <tr> <th>Parameter:</th><th><math>a_1</math></th><th><math>a_2</math></th><th><math>\lambda</math></th><th><math>\varepsilon</math></th><th></th><th></th><th></th></tr> </thead> <tbody> <tr> <td>Value:</td><td>2.1899</td><td><math>\sqrt{6}</math></td><td>4.9159</td><td>1</td><td></td><td></td><td></td></tr> </tbody> </table>							Parameter:	$a_1$	$a_2$	$\lambda$	$\varepsilon$				Value:	2.1899	$\sqrt{6}$	4.9159	1						
Parameter:	$a_1$	$a_2$	$\lambda$	$\varepsilon$																						
Value:	2.1899	$\sqrt{6}$	4.9159	1																						
Trans. Isotropy (TI)	$\mathbb{U}_\Psi = \frac{\mu_1}{2} (I_{\Psi_1} - 3) + \frac{\mu_2}{2} (I_{\Psi_2} - 3) - (\mu_1 + 2\mu_2 + \mu_3) \ln(I_{\Psi_3}) + \frac{\lambda}{2} (I_{\Psi_3} - 1)^2 + \frac{\mu_3}{2\alpha} ((I_{\Psi_6})^\alpha - 1) + \frac{\mu_3}{2\beta} ((I_{\Psi_7})^\beta - 1)$																									
	<table border="1"> <thead> <tr> <th>Parameter:</th><th><math>\mu_1</math></th><th><math>\mu_2</math></th><th><math>\mu_3</math></th><th><math>\lambda</math></th><th><math>\alpha</math></th><th><math>\beta</math></th><th><math>\varepsilon</math></th><th><math>\mathbf{N}</math></th></tr> </thead> <tbody> <tr> <td>Value:</td><td>0.5</td><td>0.5</td><td>7.5</td><td>5</td><td>2</td><td>2</td><td>1</td><td><math>\frac{1}{\sqrt{3}} [1 \ 1 \ 1]^T</math></td></tr> </tbody> </table>								Parameter:	$\mu_1$	$\mu_2$	$\mu_3$	$\lambda$	$\alpha$	$\beta$	$\varepsilon$	$\mathbf{N}$	Value:	0.5	0.5	7.5	5	2	2	1	$\frac{1}{\sqrt{3}} [1 \ 1 \ 1]^T$
Parameter:	$\mu_1$	$\mu_2$	$\mu_3$	$\lambda$	$\alpha$	$\beta$	$\varepsilon$	$\mathbf{N}$																		
Value:	0.5	0.5	7.5	5	2	2	1	$\frac{1}{\sqrt{3}} [1 \ 1 \ 1]^T$																		

Table 1: The various models used for the isothermal mechanical contribution  $\Psi_m(\mathbf{F})$  in (33).

model; Arruda-Boyce model; Hyperelastic potentials for transverse isotropy. Table 1 presents the values of the material parameters employed in defining each of the aforementioned models.

With regards to the electro-mechanical contribution  $\Psi_{em}(\mathbf{F}, \mathbf{E}_0)$ , we have considered: Ideal dielectric elastomer; Model with electric saturation, employed by some authors to account for the saturation effects associated with hard inclusions that exhibit electric saturation. Both models and the material parameters used in their definition can be seen in Table 2.

Electro-mechanical isothermal Helmholtz free energy $\Psi_{em}$														
Name of the model	Invariant representation													
Ideal dielectric (ID)	$\mathbb{U}_\Psi = \frac{\mu_1}{2} (I_{\Psi_1} - 3) + \frac{\mu_2}{2} (I_{\Psi_2} - 3) - (\mu_1 + 2\mu_2) \ln(I_{\Psi_3}) + \frac{\lambda}{2} (I_{\Psi_3} - 1)^2$													
	<table border="1"> <thead> <tr> <th>Parameter:</th><th><math>\mu_1</math></th><th><math>\mu_2</math></th><th><math>\lambda</math></th><th><math>\varepsilon</math></th></tr> </thead> <tbody> <tr> <td>Value:</td><td>0.5</td><td>0.5</td><td>5</td><td>1</td></tr> </tbody> </table>				Parameter:	$\mu_1$	$\mu_2$	$\lambda$	$\varepsilon$	Value:	0.5	0.5	5	1
Parameter:	$\mu_1$	$\mu_2$	$\lambda$	$\varepsilon$										
Value:	0.5	0.5	5	1										
Electric Saturation (ES)	$\mathbb{U}_\Psi = \frac{\mu_1}{2} (I_{\Psi_1})^2 + \frac{\mu_2}{2} (I_{\Psi_2})^2 - 6(\mu_1 + 2\mu_2) \ln(I_{\Psi_3}) + \frac{\lambda}{2} (I_{\Psi_3} - 1)^2$													
	<table border="1"> <thead> <tr> <th>Parameter:</th><th><math>\mu_1</math></th><th><math>\mu_2</math></th><th><math>\lambda</math></th><th><math>\varepsilon</math></th></tr> </thead> <tbody> <tr> <td>Value:</td><td>0.5</td><td>0.5</td><td>5</td><td>1</td></tr> </tbody> </table>				Parameter:	$\mu_1$	$\mu_2$	$\lambda$	$\varepsilon$	Value:	0.5	0.5	5	1
Parameter:	$\mu_1$	$\mu_2$	$\lambda$	$\varepsilon$										
Value:	0.5	0.5	5	1										

Table 2: The two models used for the isothermal electro-mechanical contribution  $\Psi_{em}(\mathbf{F}, \mathbf{E}_0)$  in (33).

## 4. Physics-augmented neural networks constitutive models

In the preceding section, we introduced the general form of the analytical Helmholtz free energy density, which serves as the foundation for generating in-silico data in this section. The primary goal here is to generate such data with Helmholtz free energy densities that are decomposed as per equation (33), depending on  $\mathbf{F}, \mathbf{E}_0, \theta$ . This approach aims to facilitate the construction of neural network surrogates with the capability to depend on the sets  $\{\mathbf{F}, \mathbf{E}_0, \theta\}$ ,  $\{\mathbf{F}, \mathbf{D}_0, \eta\}$ ,  $\{\mathbf{F}, \mathbf{D}_0, \theta\}$ , or  $\{\mathbf{F}, \mathbf{E}_0, \eta\}$ , as outlined in Section 3.2. These surrogates are consistently denoted as  $\Psi_{nn}$ ,  $e_{nn}$ ,  $\Upsilon_{nn}$ , or  $\Gamma_{nn}$ , respectively, in alignment with the potentials described in Section 3.2.

Crucially, to ensure compliance with fundamental physical principles, such as material frame indifference and material symmetry, we follow an invariant formulation for these potentials, as detailed in Section 3.3. All of this is mathematically encapsulated in equation (42), i.e

Ground truth model in equation (33)	Family of data-driven neural network thermodynamical potentials	
$\Psi(\mathbf{F}, \mathbf{E}_0, \theta)$	$\begin{cases} \Psi_{nn}(\mathbf{F}, \mathbf{E}_0, \theta, \mathcal{W}) = \mathbb{U}_{\Psi nn}(I_{\Psi_1}, \dots, I_{\Psi_{n_{\text{inv}}}}, \theta) \\ e_{nn}(\mathbf{F}, \mathbf{D}_0, \eta, \mathcal{W}) = \mathbb{U}_{e nn}(I_{e_1}, \dots, I_{e_{n_{\text{inv}}}}, \eta) \\ \Upsilon_{nn}(\mathbf{F}, \mathbf{D}_0, \theta, \mathcal{W}) = \mathbb{U}_{\Upsilon nn}(I_{\Upsilon_1}, \dots, I_{\Upsilon_{n_{\text{inv}}}}, \theta) \\ \Gamma_{nn}(\mathbf{F}, \mathbf{E}_0, \eta, \mathcal{W}) = \mathbb{U}_{\Gamma nn}(I_{\Gamma_1}, \dots, I_{\Gamma_{n_{\text{inv}}}}, \eta) \end{cases}$	(42)

In equation (42),  $\mathcal{W}$  represents the parameters of the neural network, which encompass

$$\mathcal{W} = \{\mathbf{W}_1, \dots, \mathbf{W}_{n_{L+1}}, \mathbf{b}_1, \dots, \mathbf{b}_{n_{L+1}}\}, \quad (43)$$

where  $\mathbf{W}_i$  and  $\mathbf{b}_i$  represent the weights and biases associated with layer  $i$ . As standard in neural networks, for an architecture with  $n_{L+1}$  layers, the inputs  $\mathbf{A}_h$  of layer  $h$  is obtained through the following expression

$$\mathbf{A}_h = \sigma_h(\mathbf{W}_h \mathbf{A}_{h-1} + \mathbf{b}_h); \quad h = \{1, \dots, n_{L+1}\} \quad (44)$$

where

$$\mathbf{W}_h \in \mathbb{R}^{n_h \times n_{h-1}}; \quad \mathbf{b}_h \in \mathbb{R}^{n_h} \quad (45)$$

where

$$n_0 = n_{\text{inv}} + 1; \quad n_{L+1} = 1 \quad (46)$$

where  $n_{\text{inv}} = 5$  or  $n_{\text{inv}} = 8$  for isotropy or transverse isotropy, respectively. Furthermore, the vectors  $\mathbf{A}_h$ , for  $h = L + 1$  represents the predicted neural network model whereas for  $h = 0$ , it represents the input of the model, namely

$$\begin{aligned} \mathbf{A}_{L+1} &= \Psi_{nn}(\mathbf{F}, \mathbf{E}_0, \theta, \mathcal{W}); & \mathbf{A}_0 &= [I_{\Psi_1} \quad I_{\Psi_2} \quad \dots \quad I_{\Psi_n} \quad \theta] \\ \mathbf{A}_{L+1} &= e_{nn}(\mathbf{F}, \mathbf{D}_0, \eta, \mathcal{W}); & \mathbf{A}_0 &= [I_{e_1} \quad I_{e_2} \quad \dots \quad I_{e_n} \quad \eta] \\ \mathbf{A}_{L+1} &= \Upsilon_{nn}(\mathbf{F}, \mathbf{D}_0, \theta, \mathcal{W}); & \mathbf{A}_0 &= [I_{\Upsilon_1} \quad I_{\Upsilon_2} \quad \dots \quad I_{\Upsilon_n} \quad \theta] \\ \mathbf{A}_{L+1} &= \Gamma_{nn}(\mathbf{F}, \mathbf{E}_0, \eta, \mathcal{W}); & \mathbf{A}_0 &= [I_{\Gamma_1} \quad I_{\Gamma_2} \quad \dots \quad I_{\Gamma_n} \quad \eta] \end{aligned} \quad (47)$$

In addition,  $\sigma_h$  represents the activation function of layer  $h$ . In our work we have made use of Softplus activation functions, except for the last layer, where we use the identity function, namely

$$\sigma_h(x) = \log(1 + e^x), \quad h = \{1, \dots, n_L\}; \quad \sigma_{n_{L+1}}(x) = x \quad (48)$$

#### 4.1. Sobolev-type calibration strategy 1

We begin by describing the fundamental aspects of this strategy (Section 4.1.1), and later, we describe the in-silico data generation strategy used in order to calibrated the models according to this strategy, carried out in Section 4.1.3.

##### 4.1.1. Fundamental aspects of the strategy

In this approach, four distinct types of neural network models, namely  $\Psi_{nn}(\mathbf{F}, \mathbf{E}_0, \theta, \mathcal{W})$ ,  $e_{nn}(\mathbf{F}, \mathbf{D}_0, \eta, \mathcal{W})$ ,  $\Upsilon_{nn}(\mathbf{F}, \mathbf{D}_0, \theta, \mathcal{W})$  or  $\Gamma_{nn}(\mathbf{F}, \mathbf{E}_0, \eta, \mathcal{W})$ , are developed with the specific objective of minimizing the discrepancy between:

- the derivatives  $\{\partial_{\mathbf{F}}\Psi_{nn}, -\partial_{\mathbf{E}_0}\Psi_{nn}, -\partial_{\theta}\Psi_{nn}\}$  and  $\{\mathbf{P}, \mathbf{D}_0, \eta\} := \{\partial_{\mathbf{F}}\Psi, -\partial_{\mathbf{E}_0}\Psi, -\partial_{\theta}\Psi\}$
- the derivatives  $\{\partial_{\mathbf{F}}e_{nn}, \partial_{\mathbf{D}_0}e_{nn}, \partial_{\eta}e_{nn}\}$  and  $\{\mathbf{P}, \mathbf{E}_0, \theta\} := \{\partial_{\mathbf{F}}\Psi, \mathbf{E}_0, \theta\}$
- the derivatives  $\{\partial_{\mathbf{F}}\Upsilon_{nn}, \partial_{\mathbf{D}_0}\Upsilon_{nn}, -\partial_{\theta}\Upsilon_{nn}\}$  and  $\{\mathbf{P}, \mathbf{E}_0, \eta\} := \{\partial_{\mathbf{F}}\Psi, \mathbf{E}_0, -\partial_{\eta}\Psi\}$
- the derivatives  $\{\partial_{\mathbf{F}}\Gamma_{nn}, -\partial_{\mathbf{E}_0}\Gamma_{nn}, \partial_{\eta}\Gamma_{nn}\}$  and  $\{\mathbf{P}, \mathbf{D}_0, \theta\} := \{\partial_{\mathbf{F}}\Psi, -\partial_{\mathbf{E}_0}\Psi, \theta\}$

showcasing that, regardless of the neural network surrogate employed, the underlying ground truth model remains a Helmholtz free energy density  $\Psi(\mathbf{F}, \mathbf{E}_0, \theta)$  as formulated in equation (33). This is illustrated schematically in Figure 4. To accomplish this objective, we define the corresponding Sobolev-type loss functions, with their specific expressions provided in Table 3.

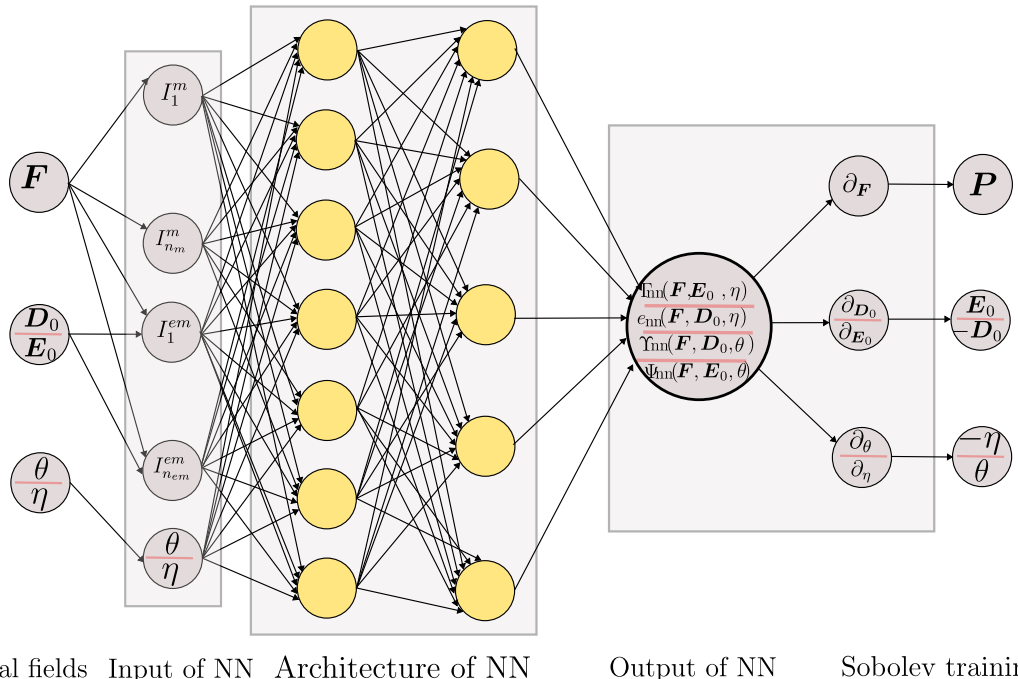


Figure 4: Simplified structure of the neural network architecture used for calibration of the four neural network-based surrogates i.e.  $\Psi_{nn}$ ,  $e_{nn}$ ,  $\Upsilon_{nn}$  or  $\Gamma_{nn}$ , for the case of Sobolev-type training strategy 1.

##### 4.1.2. Polyconvexity of neural network-based potentials

Sections 3.1 and 3.2 described the desired convexity/convexity conditions that the four possible neural network-based thermodynamical potentials, namely  $\Psi(\mathbf{F}, \mathbf{E}_0, \theta)$ ,  $e(\mathbf{F}, \mathbf{D}_0, \eta)$ ,  $\Upsilon(\mathbf{F}, \mathbf{D}_0, \theta)$  or  $\Gamma(\mathbf{F}, \mathbf{E}_0, \theta)$  should satisfy. Enforcing simultaneous convexity and convexity across multiple physics, as required for the three potentials  $\Psi(\mathbf{F}, \mathbf{E}_0, \theta)$ ,  $\Upsilon(\mathbf{F}, \mathbf{D}_0, \theta)$  or  $\Gamma(\mathbf{F}, \mathbf{E}_0, \theta)$ , presents a complex challenge. This difficulty arises whether the model is derived from a phenomenological explicit representation or constructuted using neural network frameworks. However, the direct imposition of convexity exclusively, or more specifically, polyconvexity in the sense of equation

$\mathcal{L}(\mathbf{W})$	
$\Psi_{nn}$	$\beta_1 \frac{\sum_{i=1}^{n_d} \ \partial_{\mathbf{F}} \Psi^i - \partial_{\mathbf{F}} \Psi_{nn}(\mathbf{X}^i, \mathbf{W})\ ^2}{\sum_{i=1}^{n_d} \ \partial_{\mathbf{F}} \Psi^i\ ^2} + \beta_2 \frac{\sum_{i=1}^{n_d} \ \partial_{\mathbf{E}_0} \Psi^i - \partial_{\mathbf{E}_0} \Psi_{nn}(\mathbf{X}^i, \mathbf{W})\ ^2}{\sum_{i=1}^{n_d} \ \partial_{\mathbf{E}_0} \Psi^i\ ^2}$ $+ \beta_3 \frac{\sum_{i=1}^{n_d} (\partial_{\theta} \Psi^i - \partial_{\theta} \Psi_{nn}(\mathbf{X}^i, \mathbf{W}))^2}{\sum_{i=1}^{n_d} (\partial_{\theta} \Psi^i)^2}$
$e_{nn}$	$\beta_1 \frac{\sum_{i=1}^{n_d} \ \partial_{\mathbf{F}} \Psi^i - \partial_{\mathbf{F}} e_{nn}(\mathbf{X}^i, \mathbf{W})\ ^2}{\sum_{i=1}^{n_d} \ \partial_{\mathbf{F}} \Psi^i\ ^2} + \beta_2 \frac{\sum_{i=1}^{n_d} \ \mathbf{E}_0^i - \partial_{\mathbf{D}_0} e_{nn}(\mathbf{X}^i, \mathbf{W})\ ^2}{\sum_{i=1}^{n_d} \ \mathbf{E}_0^i\ ^2}$ $+ \beta_3 \frac{\sum_{i=1}^{n_d} (\theta^i - \partial_{\eta} e_{nn}(\mathbf{X}^i, \mathbf{W}))^2}{\sum_{i=1}^{n_d} (\theta^i)^2}$
$\Upsilon_{nn}$	$\frac{\sum_{i=1}^{n_d} \ \partial_{\mathbf{F}} \Psi^i - \partial_{\mathbf{F}} \Upsilon_{nn}(\mathbf{X}^i, \mathbf{W})\ ^2}{\sum_{i=1}^{n_d} \ \partial_{\mathbf{F}} \Psi^i\ ^2} + \frac{\sum_{i=1}^{n_d} \ \mathbf{E}_0^i - \partial_{\mathbf{D}_0} \Upsilon_{nn}(\mathbf{X}^i, \mathbf{W})\ ^2}{\sum_{i=1}^{n_d} \ \mathbf{E}_0^i\ ^2}$ $+ \frac{\sum_{i=1}^{n_d} (\partial_{\theta} \Psi^i - \partial_{\theta} \Upsilon_{nn}(\mathbf{X}^i, \mathbf{W}))^2}{\sum_{i=1}^{n_d} (\partial_{\theta} \Psi^i)^2}$
$\Gamma_{nn}$	$\frac{\sum_{i=1}^{n_d} \ \partial_{\mathbf{F}} \Psi^i - \partial_{\mathbf{F}} \Gamma_{nn}(\mathbf{X}^i, \mathbf{W})\ ^2}{\sum_{i=1}^{n_d} \ \partial_{\mathbf{F}} \Psi^i\ ^2} + \frac{\sum_{i=1}^{n_d} \ \partial_{\mathbf{E}_0} \Psi^i - \partial_{\mathbf{E}_0} \Gamma_{nn}(\mathbf{X}^i, \mathbf{W})\ ^2}{\sum_{i=1}^{n_d} \ \partial_{\mathbf{E}_0} \Psi^i\ ^2}$ $+ \frac{\sum_{i=1}^{n_d} (\theta^i - \partial_{\eta} \Gamma_{nn}(\mathbf{X}^i, \mathbf{W}))^2}{\sum_{i=1}^{n_d} (\theta^i)^2}$

Table 3: Loss functions  $\mathcal{L}(\mathbf{W})$  used for the calibration of the various type of neural network-based surrogate potentials, i.e.  $\Psi_{nn}$ ,  $e_{nn}$ ,  $\Upsilon_{nn}$  or  $\Gamma_{nn}$ , for the case of Sobolev-type training strategy 1. All the potentials have been calibrated with data obtained from Helmholtz free energy density ground truth models, i.e.  $\Psi$ . The index  $i$  represents in-silico data number  $i$ , and  $n_d$  the number of data used for calibration.

(24), proves to be more tractable. Building on the work of XX and extending it from electro-mechanics to the thermo-electro-mechanical context, a sufficient condition to ensure polyconvexity of the neural network-based potential  $e_{nn}(\mathbf{F}, \mathbf{D}_0, \eta)$  is the positiveness of the weights  $\mathbf{W}_h$  and the monotonically increasing nature of the activation functions, namely

$$(\mathbf{W}_h)_{ij} > 0; \quad \sigma'_h(x) > 0, \forall x; \quad h = \{1, \dots, n_{L+1}\} \quad (49)$$

Notice that the first condition can be imposed as a penalty term in the objective function, leading to the augmented objective function  $\tilde{\mathcal{L}}(\mathbf{W})$  defined as

$$\tilde{\mathcal{L}}(\mathbf{W}) = \mathcal{L}(\mathbf{W}) + \frac{\kappa}{2} \sum_i \left( \min((\mathbf{W}_v)_i, 0) \right)^2 \quad (50)$$

where  $\mathcal{L}(\mathbf{W})$  is defined as in Table 3,  $\mathbf{W}_v$  represents the concatenation of all vectorized weights  $\mathbf{W}_h$ ,  $h = \{1, \dots, n_{L+1}\}$ , and  $\kappa$ , the penalty parameter. Furthermore, notice that increasing monotonicity is satisfied by the activation functions chosen in equation (48). In this work, we will explore the accuracy of neural network-based  $e_{nn}(\mathbf{F}, \mathbf{D}_0, \eta)$  potentials with and without the additional penalty term enforcing the polyconvexity condition. This will be further discussed in Section 6.1.3.

#### 4.1.3. In-silico data generation strategy

In this section, we present the procedure used for generating synthetic data for the training strategy denoted as strategy 1. For that, we have made use of the generic form of the Helmholtz free energy density in equation (33), and a variety of models for the isothermal purely mechanical and electro-mechanical contributions  $\Psi_m(\mathbf{F})$  (see Table 1) and  $\Psi_{em}(\mathbf{F}, \mathbf{E}_0)$  (refer to Table 2).

To acquire the dataset, we have adhered to the procedure outlined in [?], extended to the coupled context of thermo-electro-mechanics. The deformation gradient tensor  $\mathbf{F}$  is parameterized via a chosen set of deviatoric directions, amplitudes, and Jacobians ( $J$ , i.e., the determinant of  $\mathbf{F}$ ). The process of generating sample points for deviatoric directions, amplitudes, and Jacobians is elucidated in Algorithm 1. Similarly, the electric displacement  $\mathbf{E}_0$  (for the neural network-based potentials  $\Psi_{nn}(\mathbf{F}, \mathbf{E}_0, \theta)$  and  $\Upsilon_{nn}(\mathbf{F}, \mathbf{E}_0, \eta)$ ) or  $\mathbf{D}_0$  (for the neural network-based potentials  $e_{nn}(\mathbf{F}, \mathbf{D}_0, \eta)$  and  $\Gamma_{nn}(\mathbf{F}, \mathbf{D}_0, \theta)$ ) is also parametrised in terms of unitary directions and amplitudes. Concerning the deviatoric directions for  $\mathbf{F}$ , denoted as  $\mathbf{V}_F$  we formulate them using a spherical parametrization in  $\mathbb{R}^5$ , precisely representing these directions using five pertinent angular measures ( $\phi_1, \phi_2, \phi_3, \phi_4, \phi_5 \in [0, 2\pi] \times [0, \pi] \times [0, \pi] \times [0, \pi] \times [0, \pi]$ ) within this 5-dimensional space. For the directions employed for the parametrisation of  $\mathbf{E}_0$  or  $\mathbf{D}_0$  (depending on the dependence on the electrical physics of the neural network-based potential), denoted as  $\mathbf{V}_{E_0}$  or  $\mathbf{V}_{D_0}$ , respectively, these are created using a spherical parametrization in  $\mathbb{R}^3$ , using as angular measures  $(\theta, \psi) \in [0, 2\pi] \times [0, \pi]$ , namely

$$\mathbf{V}_F^i = \begin{bmatrix} \cos \phi_1^i \\ \sin \phi_1^i \cos \phi_2^i \\ \sin \phi_1^i \sin \phi_2^i \cos \phi_3^i \\ \sin \phi_1^i \sin \phi_2^i \sin \phi_3^i \cos \phi_4^i \\ \sin \phi_1^i \sin \phi_2^i \sin \phi_3^i \sin \phi_4^i \end{bmatrix}; \quad 1 \leq i \leq n_{V_F}; \quad \mathbf{V}_{E_0}^i = \begin{bmatrix} \cos \psi_1^i \sin \psi_2^i \\ \sin \psi_1^i \sin \psi_2^i \\ \cos \psi_2^i \end{bmatrix}; \quad 1 \leq i \leq n_{V_{E_0}} \quad (51)$$

Once the sample is generated following Algorithm 1, the reconstruction of the deformation gradient tensor  $\mathbf{F}$  and of  $\mathbf{D}_0$  becomes possible at each of the sampling points. This reconstruction process is demonstrated in Algorithm 2, where  $\Psi$  represents the basis for symmetric and traceless tensors (refer to Appendix ?? for details on  $\Psi$ ). For the temperature field  $\theta$ , data generation has been carried out by predefining the maximum difference with respect to the reference temperature  $\theta_R$ . This approach establishes the lower and upper bounds  $\theta_R - \Delta\theta$  and  $\theta_R + \Delta\theta$ . Consequently, the data for this field is generated either uniformly distributed within this interval or randomly sampled across the defined range.

---

**Algorithm 1** Pseudo-code for sample generation

---

1: Generate deformation gradient tensors  $\mathbf{F}$  according to:

- 1: Set the number of amplitudes, directions and determinants:  $\{n_{\mathbf{t}_F}, n_{\mathbf{V}_F}, n_{\mathbf{J}_F}\}$ ;
- 2: Initialise a vector of Latin Hypercube Sampled angles:  $\phi_1 = [0, 2\pi]_{n_{\mathbf{V}_F} \times 1}$  and  $\phi_{2,\dots,4} = [0, \pi]_{n_{\mathbf{V}_F} \times 1}$ ;
- 3: Construct the directions,  $\mathbf{V}_F$ , using  $\phi_1, \dots, \phi_4$  by means of an extended Spherical parametrisation in  $\mathbb{R}^5$  - detailed in (51);
- 4: Evaluate the deformation gradient tensors,  $\mathbf{F}$  - detailed in Algorithm 2;

5: Generate electric field vectors  $\mathbf{E}_0$  (or  $\mathbf{D}_0$ ) according to:

- 1: Set the amplitudes and directions:  $\{n_{\mathbf{t}_{E_0}}, n_{\mathbf{V}_{E_0}}\}$ ;
- 2: Initialise a vector of Latin Hypercube Sampled angles:  $\psi_1 = [0, 2\pi]_{n_{\mathbf{V}_{E_0}} \times 1}$  and  $\psi_2 = [0, \pi]_{n_{\mathbf{V}_{E_0}} \times 1}$ ;
- 3: Construct the directions,  $\mathbf{V}_{E_0}$  (or  $\mathbf{V}_{D_0}$ ), using  $\psi_1, \psi_2$  by means of a Spherical parametrisation in  $\mathbb{R}^3$ ;
- 4: Evaluate the deformation  $\mathbf{E}_0$  (or  $\mathbf{D}_0$ ) - detailed in Algorithm 2;

5: Generate temperature data  $\theta$  (or entropy  $\eta$ ) according to:

- 1: Set the maximum temperature difference with respect to  $\theta_R$ , denoted  $\Delta\theta$ . Then define the minimum and maximum values of  $\theta$ :  $\theta_R - \Delta\theta$  and  $\theta_R + \Delta\theta$ ; For  $\eta$ -based potentials, set  $\eta_{\min}$  and  $\eta_{\max}$
- 2: Set number of temperatures  $n_\theta$  (or  $n_\eta$ );
- 3: Generate  $n_\theta$  uniformly distributed temperature (or randomly) in the interval  $(\theta_R - \Delta\theta, \theta_R + \Delta\theta)$ ; For  $\eta$ -based potentials, the interval is  $(\eta_{\min}, \eta_{\max})$

4: Generate combination of data of  $\{\mathbf{F}, \mathbf{E}_0, \theta\}$  (or any other combination, for instance  $\{\mathbf{F}, \mathbf{D}_0, \eta\}$ )

---

**Algorithm 2** Pseudo-code for construction of the set of deformation gradient tensors and electric fields  $\mathbf{E}_0$  (similarly for  $\mathbf{D}_0$ )

---

```

1: for  $i = 1 : n_{\mathbf{V}_F}$  do
2:   for  $j = 1 : n_J$  do
3:     for  $k = 1 : n_{t_F}$  do
4:        $\mathbf{F} = J_j^{1/3} \exp ([\mathbf{t}_F]_k [\sum_{m=1}^5 [\mathbf{V}_F^i]_m \Psi_m])$ ;
5:     end for
6:   end for
7: end for
8: for  $i = 1 : n_{\mathbf{V}_{E_0}}$  do
9:   for  $j = 1 : n_{t_{E_0}}$  do
10:     $\mathbf{E}_0 = [\mathbf{t}_{E_0}]_j \mathbf{V}_{E_0}^i$ ;
11:   end for
12: end for

```

---

## 4.2. Sobolev-type calibration strategy 2

The calibration approach outlined in Section 4.1, referred to as calibration strategy 1, is characterized by its remarkable flexibility—enabling the calibration of four distinct types of thermodynamic potentials—and its robustness, as demonstrated in the numerical examples section. However, this approach is subject to criticism when applied to scenarios involving data generated in real-world conditions, as opposed to an in-silico process. While calibration strategy 1 is well-suited for data generated in-silico, as is the case in this study, its applicability may be severely limited when dealing with laboratory-derived data. The primary challenge arises from the requirement for data across six quantities:  $\{\mathbf{F}, \mathbf{E}_0, \theta, \mathbf{P}, \mathbf{D}_0, \eta\}$ . Of these, entropy ( $\eta$ ) cannot be directly measured in a laboratory setting, which significantly impairs the feasibility of this calibration strategy in practical, real-world scenarios.

To address this limitation, we have developed an alternative strategy that can be applied to both in-silico and experimentally generated data. The key aspect of this approach lies in substituting the only non-measurable field within  $\{\mathbf{F}, \mathbf{E}_0, \theta, \mathbf{P}, \mathbf{D}_0, \eta\}$ , namely  $\eta$ , with other thermophysical properties that can be directly measured in a laboratory setting. This modification enhances the versatility of the calibration process, making it applicable to real-world experimental data as well as computationally generated scenarios. A suitable physical property to replace  $\eta$  is the specific heat capacity  $c_v$  (see equation (D.2)).

As discussed in Section 3.4, specifically for the generic Helmholtz free energy density considered in this study,  $c_v$  may exhibit a nonlinear dependence on the fields fields  $\{\mathbf{F}, \mathbf{E}_0, \theta\}$ , as highlighted in the experimental work of XX. Therefore, we consider incorporating data values for  $c_v$  at a set of points  $\mathcal{G}_{c_v} = \{\mathbf{X}^1, \dots, \mathbf{X}^{n_{c_v}}\}$ , which includes the reference configuration  $\mathbf{X}^1 = \{\mathbf{I}, \mathbf{0}, \theta_R\}$  as well as other possible scenarios  $\mathbf{X}^i = \{\mathbf{F}^i, \mathbf{E}_0^i, \theta^i\}$ , with  $n_{c_v}$  the number of data points within the set  $\mathcal{G}_{c_v}$ . However, the available experimental data for  $c_v$ , is typically limited to the reference configuration. To better align with conditions more reflective of the experimental setup, we choose to include only the specific heat capacity  $c_v$  data corresponding to the reference configuration, i.e.,  $\mathcal{G}_{c_v} = \mathbf{X}^1$ . Additionally, while entropy  $\eta$  cannot be directly measured, it is known to vanish in the reference configuration (see equation (14)). Thus, this condition can also be incorporated into the calibration strategy.

Notice that this new approach introduces notable differences in the calibration of the potentials that do depend on  $\theta$  (i.e  $\Psi_{nn}(\mathbf{F}, \mathbf{E}_0, \theta)$  and  $\Upsilon_{nn}(\mathbf{F}, \mathbf{D}_0, \theta)$ ) and those which depend on  $\eta$  (i.e  $e_{nn}(\mathbf{F}, \mathbf{D}_0, \eta)$  and  $\Gamma_{nn}(\mathbf{F}, \mathbf{E}_0, \eta)$ ). The main difference resides in the fact that temperature is data which can be measured and therefore, is available in the calibration (for  $\Psi_{nn}(\mathbf{F}, \mathbf{E}_0, \theta)$  and  $\Upsilon_{nn}(\mathbf{F}, \mathbf{D}_0, \theta)$ ). However, we assume in this approach that the entropy  $\eta$  is not measurable and therefore, not readily available. Consequently, the potentials  $e_{nn}(\mathbf{F}, \mathbf{D}_0, \eta)$  and  $\Gamma_{nn}(\mathbf{F}, \mathbf{E}_0, \eta)$  must be calibrated in the absence of any information or data regarding the third argument,  $\eta$ . This inherent limitation necessitates a distinct treatment for the calibration strategy, differentiating between those potentials that depend on  $\theta$  (namely,  $\Psi_{nn}(\mathbf{F}, \mathbf{E}_0, \theta)$  and  $\Upsilon_{nn}(\mathbf{F}, \mathbf{D}_0, \theta)$ ) and those that depend on  $\eta$  ( $e_{nn}(\mathbf{F}, \mathbf{D}_0, \eta)$  and  $\Gamma_{nn}(\mathbf{F}, \mathbf{E}_0, \eta)$ ).

### 4.2.1. Mathematical formulation of the strategy: potentials depending upon $\theta$

For the temperature dependent potentials, i.e.  $\Psi_{nn}(\mathbf{F}, \mathbf{E}_0, \theta, \mathbf{W})$  and  $\Upsilon_{nn}(\mathbf{F}, \mathbf{D}_0, \theta, \mathbf{W})$ , this alternative and more physically oriented calibration approach, the specific objective is to minimize the discrepancy between:

- $\Psi_{nn}$   $\left\{ \begin{array}{l} \text{the derivatives } \{\partial_{\mathbf{F}}\Psi_{nn}, -\partial_{\mathbf{E}_0}\Psi_{nn}\} \text{ and } \{\mathbf{P}, \mathbf{D}_0\} := \{\partial_{\mathbf{F}}\Psi, -\partial_{\mathbf{E}_0}\Psi\} \\ \text{the fields } \{-\theta\partial_{\theta\theta}^2\Psi_{nn}, -\partial_\theta\Psi_{nn}|_{\mathbf{I}, \mathbf{0}, \theta_R}\} \text{ and } \{c_v, \eta|_{\mathbf{I}, \mathbf{0}, \theta_R}\} := \{-\theta\partial_{\theta\theta}^2\Psi, -\partial_\theta\Psi|_{\mathbf{I}, \mathbf{0}, \theta_R}\} \\ \{\mathbf{F}, \mathbf{E}_0, \theta\} \text{ are data} \end{array} \right.$

- $\Upsilon_{nn}$  the derivatives  $\{\partial_{\mathbf{F}} \Upsilon_{nn}, \partial_{\mathbf{D}_0} \Upsilon_{nn}\}$  and  $\{\mathbf{P}, \mathbf{E}_0\} := \{\partial_{\mathbf{F}} \Psi, \mathbf{E}_0\}$   
the fields  $\{-\theta \partial_{\theta\theta}^2 \Upsilon_{nn}, -\partial_{\theta} \Upsilon_{nn}|_{\mathbf{I}, \mathbf{0}, \theta_R}\}$  and  $\{c_v, \eta|_{\mathbf{I}, \mathbf{0}, \theta_R}\} := \{-\theta \partial_{\theta\theta}^2 \Psi, -\partial_{\theta} \Psi|_{\mathbf{I}, \mathbf{0}, \theta_R}\}$   
 $\{\mathbf{F}, \mathbf{D}_0, \theta\}$  are data

This is illustrated schematically in Figure 5. Notice that, unlike in the preceding calibration strategy, the unavailability of  $\eta$  prevents us to minimise the difference between  $\theta$  and the derivatives of the two potentials with respect to  $\theta$ , namely  $-\partial_{\theta} \Psi_{nn}$  and  $-\partial_{\theta} \Upsilon_{nn}$ . Instead, we have incorporated  $c_v$  and  $\partial_{\theta} \Psi_{nn}|_{\mathbf{I}, \mathbf{0}, \theta_R}$  (or  $\partial_{\theta} \Upsilon_{nn}|_{\mathbf{I}, \mathbf{0}, \theta_R}$ ) in the minimisation problem. This is reflected in the loss function observed in Table 4.

$\mathcal{L}(\mathbf{W})$	
$\Psi_{nn}$	$\beta_1 \frac{\sum_{i=1}^{n_d} \ \partial_{\mathbf{F}} \Psi^i - \partial_{\mathbf{F}} \Psi_{nn}(\mathbf{X}^i, \mathbf{W})\ ^2}{\sum_{i=1}^{n_d} \ \partial_{\mathbf{F}} \Psi^i\ ^2} + \beta_2 \frac{\sum_{i=1}^{n_d} \ \partial_{\mathbf{E}_0} \Psi^i - \partial_{\mathbf{E}_0} \Psi_{nn}(\mathbf{X}^i, \mathbf{W})\ ^2}{\sum_{i=1}^{n_d} \ \partial_{\mathbf{E}_0} \Psi^i\ }$ $+ \beta_3 \frac{\sum_{i=1}^{n_{cv}} \left( \theta^i \partial_{\theta\theta}^2 \Psi^i - \theta \partial_{\theta\theta}^2 \Psi_{nn}(\mathbf{X}^i, \mathbf{W}) \right)^2}{\sum_{i=1}^{n_d} (\theta^i \partial_{\theta\theta}^2 \Psi^i)^2} + \beta_4 \left( \partial_{\theta} \Psi_{nn}(\mathbf{X}^1, \mathbf{W}) _{\mathbf{I}, \mathbf{0}, \theta_R} \right)^2$
$\Upsilon_{nn}$	$\beta_1 \frac{\sum_{i=1}^{n_d} \ \partial_{\mathbf{F}} \Psi^i - \partial_{\mathbf{F}} \Upsilon_{nn}(\mathbf{X}^i, \mathbf{W})\ ^2}{\sum_{i=1}^{n_d} \ \partial_{\mathbf{F}} \Psi^i\ ^2} + \beta_2 \frac{\sum_{i=1}^{n_d} \ \mathbf{E}_0^i - \partial_{\mathbf{D}_0} \Upsilon_{nn}(\mathbf{X}^i, \mathbf{W})\ ^2}{\sum_{i=1}^{n_d} \ \mathbf{E}_0^i\ ^2}$ $+ \beta_3 \frac{\sum_{i=1}^{n_{cv}} \left( \theta^i \partial_{\theta\theta}^2 \Psi^i - \theta \partial_{\theta\theta}^2 \Upsilon_{nn}(\mathbf{X}^i, \mathbf{W}) \right)^2}{\sum_{i=1}^{n_d} (\theta^i \partial_{\theta\theta}^2 \Psi^i)^2} + \beta_4 \left( \partial_{\theta} \Upsilon_{nn}(\mathbf{X}^1, \mathbf{W}) _{\mathbf{I}, \mathbf{0}, \theta_R} \right)^2$

Table 4: Loss functions  $\mathcal{L}(\mathbf{W})$  used for the calibration of  $\theta$ -based neural network-based surrogate potentials, i.e.  $\Psi_{nn}$ ,  $\Upsilon_{nn}$ , for the case of Sobolev-type training strategy 2 described in Section 4.2.1. All the potentials have been calibrated with data obtained from Helmholtz free energy density ground truth models, i.e.  $\Psi$ . The index  $i$  represents in-silico data number  $i$ , and  $n_d$  the number of data used for calibration, whereas  $n_{cv}$  represents the number of data used for the measurement/evaluation of  $c_v$ .

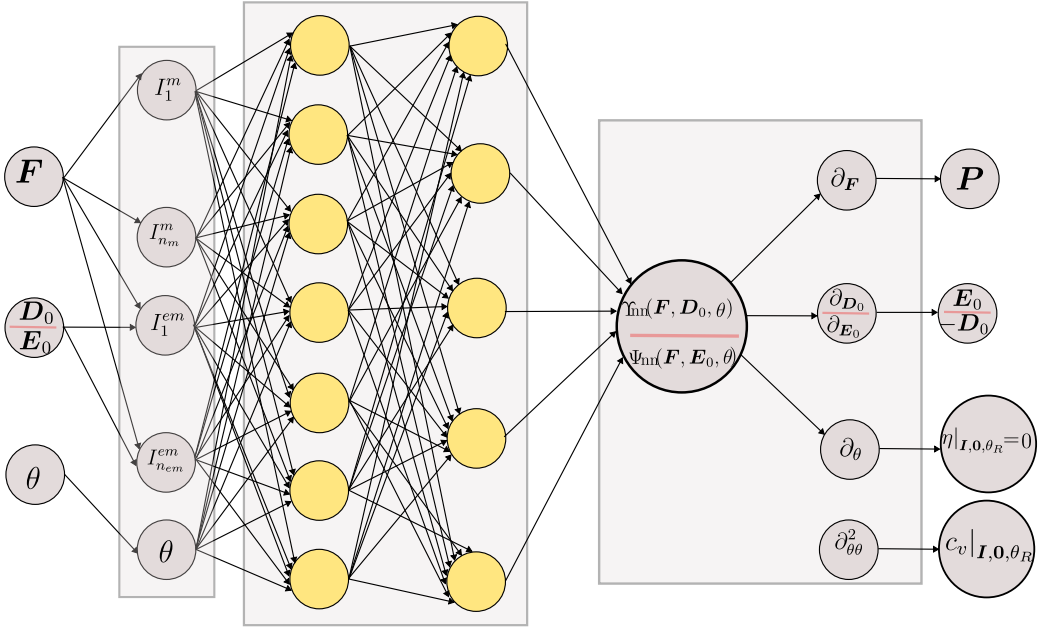


Figure 5: Simplified structure of the neural network architecture used for calibration of the  $\theta$ -based network-based surrogate potentials i.e.  $\Psi_{nn}$ ,  $\Gamma_{nn}$ , for the case of Sobolev-type training strategy 2 in Section 4.2.1.

#### 4.2.2. Mathematical formulation of the strategy: potentials depending upon $\eta$

For the two  $\eta$ -based potentials, specifically  $e(\mathbf{F}, \mathbf{D}_0, \eta)$  and  $\Gamma(\mathbf{F}, \mathbf{E}_0, \eta)$ , the second calibration strategy introduces a distinct differentiation compared to the  $\theta$ -based potentials discussed in Section 4.2.1. The key distinction lies in the fact that one of the inputs to these potentials, the entropy  $\eta$ , is not directly available from the given data. Instead, what is provided is the temperature, which corresponds to the derivative of both potentials with respect to  $\eta$ . Consequently,  $\eta$  must be determined implicitly through the nonlinear relationships presented in the third column of the first and third rows of equation (19). This relationship can be mathematically reformulated as:

$$\begin{aligned} &\text{Given } \{\mathbf{F}, \mathbf{D}_0, \theta\}, \text{ solve } \eta \text{ from: } \theta = \partial_\eta e_{nn}(\mathbf{F}, \mathbf{D}_0, \eta) \\ &\text{Given } \{\mathbf{F}, \mathbf{E}_0, \theta\}, \text{ solve } \eta \text{ from: } \theta = \partial_\eta \Gamma_{nn}(\mathbf{F}, \mathbf{E}_0, \eta) \end{aligned} \quad (52)$$

For these entropy-based dependent potentials, i.e.  $e_{nn}(\mathbf{F}, \mathbf{D}_0, \theta, \mathcal{W})$  and  $\Gamma_{nn}(\mathbf{F}, \mathbf{E}_0, \theta, \mathcal{W})$ , this alternative and more physically oriented calibration approach, the specific objective is to satisfy the implicit relationship in (52) whilst minimizing the discrepancy between:

- $e_{nn}$   $\left\{ \begin{array}{l} \text{the derivatives } \{\partial_{\mathbf{F}} e_{nn}, \partial_{\mathbf{D}_0} e_{nn}, \partial_\eta e_{nn}\} \text{ and } \{\mathbf{P}, \mathbf{D}_0, \theta\} := \{\partial_{\mathbf{F}} \Psi, \mathbf{D}_0, \theta\} \\ \text{the field } \frac{\theta}{\partial_{\theta\theta}^2 e} \text{ and } c_v := -\theta \Psi_{\theta\theta}^2 \\ \{\mathbf{F}, \mathbf{D}_0\} \text{ are data} \\ \eta \text{ is not data and it is obtained implicitly from } \theta = \partial_\eta e_{nn}(\mathbf{F}, \mathbf{D}_0, \eta) \end{array} \right.$
- $\Gamma_{nn}$   $\left\{ \begin{array}{l} \text{the derivatives } \{\partial_{\mathbf{F}} \Gamma_{nn}, -\partial_{\mathbf{E}_0} \Gamma_{nn}, \partial_\eta \Gamma_{nn}\} \text{ and } \{\mathbf{P}, \mathbf{E}_0, \theta\} := \{\partial_{\mathbf{F}} \Psi, -\partial_{\mathbf{E}_0} \Psi, \theta\} \\ \text{the field } \frac{\theta}{\partial_{\theta\theta}^2 \Gamma} \text{ and } c_v := -\theta \Psi_{\theta\theta}^2 \\ \{\mathbf{F}, \mathbf{D}_0\} \text{ are data} \\ \eta \text{ is not data and it is obtained implicitly from } \theta = \partial_\eta \Gamma_{nn}(\mathbf{F}, \mathbf{E}_0, \eta) \end{array} \right.$

A second distinguishing feature of the second calibration approach applied to  $\eta$ -based potentials again arises from the fact that one of the inputs, specifically  $\eta$ , is not directly available from

the data set. In particular, when solving, for example, using a Newton-Raphson numerical scheme to iteratively resolve equation (52), certain convexity and stability conditions must be satisfied to ensure the existence of a solution. These conditions are inherently embedded within equation (21), necessitating the convexity of both potentials  $e_{nn}$  and  $\Gamma_{nn}$  with respect to  $\eta$ , namely:

$$\partial_{\eta\eta}^2 e_{nn}(\mathbf{F}, \mathbf{D}_0, \eta) > 0; \quad \partial_{\eta\eta}^2 \Gamma_{nn}(\mathbf{F}, \mathbf{E}_0, \eta) > 0 \quad (53)$$

We found that the numerical solution of (52) benefits from the imposition of the condition in the reference configuration in equation 20, namely

$$\partial_\eta e(\mathbf{F}, \mathbf{D}_0, \eta)|_{\mathbf{I}, \mathbf{0}, 0} = \theta_R; \quad \partial_\eta \Gamma(\mathbf{F}, \mathbf{E}_0, \eta)|_{\mathbf{I}, \mathbf{0}, 0} = \theta_R \quad (54)$$

To inherently satisfy both conditions (54) and (53) within the neural network-based potentials  $e_{nn}$  and  $\Gamma_{nn}$ , we propose the formulation of modified potentials, denoted as  $\tilde{e}_{nn}$  and  $\tilde{\Gamma}_{nn}$ .

$$\begin{aligned} \tilde{e}_{nn}(\mathbf{F}, \mathbf{D}_0, \eta) &= \underbrace{e_{nn}(\mathbf{F}, \mathbf{D}_0, \eta)}_{\text{Neural network model}} + \underbrace{\left( \theta_R - \partial_\eta e_{nn}(\mathbf{F}, \mathbf{D}_0, \eta)|_{\mathbf{I}, \mathbf{0}, 0} \right) \eta}_{\text{Condition enforcement in reference conf.}} + \underbrace{\alpha_{\text{stb}} \frac{\theta_R}{2c_{vR}} \eta^2}_{\text{Stabilizing term}} \\ \tilde{\Gamma}_{nn}(\mathbf{F}, \mathbf{E}_0, \eta) &= \underbrace{\Gamma_{nn}(\mathbf{F}, \mathbf{E}_0, \eta)}_{\text{Neural network model}} + \underbrace{\left( \theta_R - \partial_\eta \Gamma_{nn}(\mathbf{F}, \mathbf{E}_0, \eta)|_{\mathbf{I}, \mathbf{0}, 0} \right) \eta}_{\text{Condition enforcement in reference conf.}} + \underbrace{\alpha_{\text{stb}} \frac{\theta_R}{2c_{vR}} \eta^2}_{\text{Stabilizing term}} \end{aligned} \quad (55)$$

In fact, evaluation of the first and second derivative with respect to  $\eta$  for both modified potentials in (55) yields

$$\begin{aligned} \partial_\eta &\Rightarrow \begin{cases} \partial_\eta \tilde{e}_{nn}(\mathbf{F}, \mathbf{D}_0, \eta) = \partial_\eta e_{nn}(\mathbf{F}, \mathbf{D}_0, \eta) + \theta_R - \partial_\eta e_{nn}(\mathbf{F}, \mathbf{D}_0, \eta)|_{\mathbf{I}, \mathbf{0}, 0} + \alpha_{\text{stb}} \frac{\theta_R}{c_{vR}} \eta \\ \partial_\eta \tilde{\Gamma}_{nn}(\mathbf{F}, \mathbf{E}_0, \eta) = \partial_\eta \Gamma_{nn}(\mathbf{F}, \mathbf{E}_0, \eta) + \theta_R - \partial_\eta \Gamma_{nn}(\mathbf{F}, \mathbf{E}_0, \eta)|_{\mathbf{I}, \mathbf{0}, 0} + \alpha_{\text{stb}} \frac{\theta_R}{c_{vR}} \eta \end{cases} \\ \partial_{\eta\eta}^2 &\Rightarrow \begin{cases} \partial_{\eta\eta}^2 \tilde{e}_{nn}(\mathbf{F}, \mathbf{D}_0, \eta) = \partial_{\eta\eta}^2 e_{nn}(\mathbf{F}, \mathbf{D}_0, \eta) + \underbrace{\alpha_{\text{stb}} \frac{\theta_R}{c_{vR}}}_{>0} \\ \partial_{\eta\eta}^2 \tilde{\Gamma}_{nn}(\mathbf{F}, \mathbf{E}_0, \eta) = \partial_{\eta\eta}^2 \Gamma_{nn}(\mathbf{F}, \mathbf{E}_0, \eta) + \underbrace{\alpha_{\text{stb}} \frac{\theta_R}{c_{vR}}}_{>0} \end{cases} \end{aligned} \quad (56)$$

Clearly, evaluation of the first derivative in (56) in the reference configuration for both potentials leads to the satisfaction of the condition in equation (54), namely

$$\begin{aligned} \partial_\eta \tilde{e}_{nn}(\mathbf{F}, \mathbf{D}_0, \eta)|_{\mathbf{I}, \mathbf{0}, 0} &= \partial_\eta e_{nn}(\mathbf{F}, \mathbf{D}_0, \eta)|_{\mathbf{I}, \mathbf{0}, 0} + \theta_R - \partial_\eta e_{nn}(\mathbf{F}, \mathbf{D}_0, \eta)|_{\mathbf{I}, \mathbf{0}, 0} = \theta_R \\ \partial_\eta \tilde{\Gamma}_{nn}(\mathbf{F}, \mathbf{E}_0, \eta)|_{\mathbf{I}, \mathbf{0}, 0} &= \partial_\eta \Gamma_{nn}(\mathbf{F}, \mathbf{E}_0, \eta)|_{\mathbf{I}, \mathbf{0}, 0} + \theta_R - \partial_\eta \Gamma_{nn}(\mathbf{F}, \mathbf{E}_0, \eta)|_{\mathbf{I}, \mathbf{0}, 0} = \theta_R \end{aligned} \quad (57)$$

To examine the second derivative in (56), it becomes evident that while the second term is positive, there is no guarantee that the overall derivative, specifically  $\partial_{\eta\eta}^2 \tilde{e}_{nn}(\mathbf{F}, \mathbf{D}_0, \eta)$  and  $\partial_{\eta\eta}^2 \tilde{\Gamma}_{nn}(\mathbf{F}, \mathbf{E}_0, \eta)$ , will be positive. The positivity of these derivatives is contingent upon the chosen value of the stabilizing parameter  $\alpha_{\text{stb}}$ . Based on our empirical observations, we have determined that setting  $\alpha_{\text{stb}} = 0.25$  suffices to prevent numerical instabilities during the solution of equation (52).

The calibration method for the  $\eta$ -based potentials outlined above is depicted schematically in Figure 6. To achieve the primary goal of this calibration approach, we define the associated Sobolev-type loss functions, with their specific formulations detailed in Table 5.

$$\mathcal{L}(\mathbf{W})$$

$e_{nn}$ $\beta_1 \frac{\sum_{i=1}^{n_d} \ \partial_{\mathbf{F}} \Psi^i - \partial_{\mathbf{F}} e_{nn}(\mathbf{X}^i, \mathbf{W})\ ^2}{\sum_{i=1}^{n_d} \ \partial_{\mathbf{F}} \Psi^i\ ^2} + \beta_2 \frac{\sum_{i=1}^{n_d} \ \mathbf{E}_0^i - \partial_{\mathbf{D}_0} e_{nn}(\mathbf{X}^i, \mathbf{W})\ ^2}{\sum_{i=1}^{n_d} \ \mathbf{E}_0^i\ ^2} \quad \mathbf{X}^i = \{\mathbf{F}^i, -\partial_{\mathbf{E}_0} \Psi^i, -\partial_{\theta} \Psi^i\}$ $+ \beta_3 \frac{\sum_{i=1}^{n_d} (\theta^i - \partial_{\eta} e_{nn}(\mathbf{X}^i, \mathbf{W}))^2}{\sum_{i=1}^{n_d} (\theta^i)^2}$	$\Gamma_{nn}$ $\beta_1 \frac{\sum_{i=1}^{n_d} \ \partial_{\mathbf{F}} \Psi^i - \partial_{\mathbf{F}} \Gamma_{nn}(\mathbf{X}^i, \mathbf{W})\ ^2}{\sum_{i=1}^{n_d} \ \partial_{\mathbf{F}} \Psi^i\ ^2} + \beta_2 \frac{\sum_{i=1}^{n_d} \ \partial_{\mathbf{E}_0} \Psi^i - \partial_{\mathbf{E}_0} \Gamma_{nn}(\mathbf{X}^i, \mathbf{W})\ ^2}{\sum_{i=1}^{n_d} \ \partial_{\mathbf{E}_0} \Psi^i\ ^2} \quad \mathbf{X}^i = \{\mathbf{F}^i, \mathbf{E}_0^i, -\partial_{\theta} \Psi^i\}$ $+ \beta_3 \frac{\sum_{i=1}^{n_d} (\theta^i - \partial_{\eta} \Gamma_{nn}(\mathbf{X}^i, \mathbf{W}))^2}{\sum_{i=1}^{n_d} (\theta^i)^2}$
---	--

Table 5: Loss functions  $\mathcal{L}(\mathbf{W})$  used for the calibration of  $\eta$ -based neural network-based surrogate potentials, i.e.  $e_{nn}$ ,  $\Gamma_{nn}$ , for the case of Sobolev-type training strategy 2 described in Section 4.2.2. All the potentials have been calibrated with data obtained from Helmholtz free energy density ground truth models, i.e.  $\Psi$ . The index  $i$  represents in-silico data number  $i$ , and  $n_d$  the number of data used for calibration, whereas  $n_{cv}$  represents the number of data used for the measurement/evaluation of  $c_v$ .

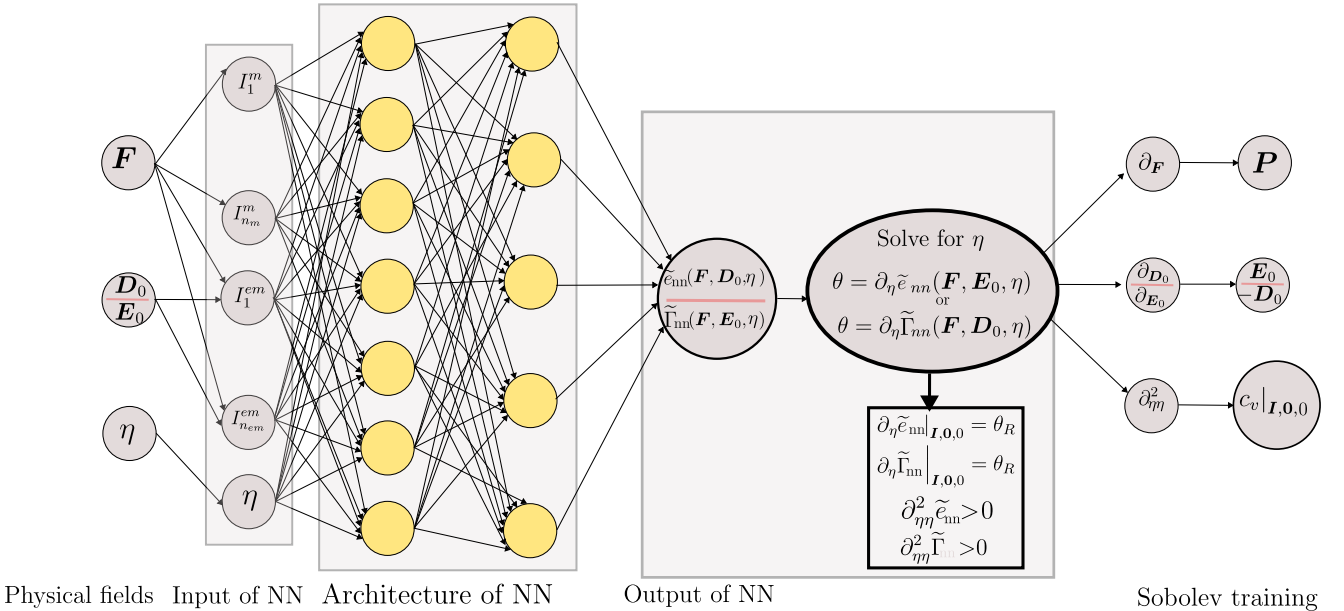


Figure 6: Simplified structure of the neural network architecture used for calibration of the  $\eta$ -based network-based surrogate potentials i.e.  $e_{nn}$ ,  $\Gamma_{nn}$ , for the case of Sobolev-type training strategy 2 in Section 4.2.2. Enforcement of conditions (53) and (54) is carried out through the modifications in equation (55).

#### 4.2.3. In-silico data generation strategy

In this section, we briefly described the procedure used for generating synthetic data for the calibration strategy denoted as strategy 2. The procedure is entirely the same as for strategy 1, summarised in Algorithm 1. The generation of deformation gradient tensors (step 1 in Algorithm 1) and electric fields  $\mathbf{E}_0$  or electric displacement fields  $\mathbf{D}_0$  (step 2 in Algorithm 1) is entirely the same as for strategy 1 in Algorithm 1. The main difference lies with regards step 3 in Algorithm 1. We summarise for convenience the steps followed in the data generation procedure for calibration strategy 1, and supplement those for calibration strategy 2, permitting a direct comparison between both strategies:

##### Data generation strategy 1:

- For  $\theta$ -based potentials, i.e.  $\Psi_{nn}(\mathbf{F}, \mathbf{E}_0, \theta)$  or  $\Upsilon_{nn}(\mathbf{F}, \mathbf{D}_0, \theta)$ , fields  $\{\mathbf{F}, \mathbf{E}_0, \theta\}$  or  $\{\mathbf{F}, \mathbf{D}_0, \theta\}$ , respectively, are generated as input data according to Algorithm 1. Evaluation of the model permits then to synthetically generate the work conjugate fields  $\{\mathbf{P}, \mathbf{D}_0, \eta\}$  or  $\{\mathbf{P}, \mathbf{E}_0, \eta\}$ , respectively, as output variables.
- For  $\eta$ -based potentials, i.e.  $e(\mathbf{F}, \mathbf{D}_0, \eta)$  and  $\Gamma(\mathbf{F}, \mathbf{E}_0, \eta)$ , the process is the opposite:  $\{\mathbf{F}, \mathbf{D}_0, \eta\}$  or  $\{\mathbf{F}, \mathbf{E}_0, \eta\}$ , respectively, are generated as input data according to Algorithm 1. Evaluation of the model permits then to synthetically generate the work conjugate fields  $\{\mathbf{P}, \mathbf{E}_0, \theta\}$  or  $\{\mathbf{P}, \mathbf{D}_0, \theta\}$ , respectively, as output variables.

##### Data generation strategy 2:

- For  $\theta$ -based potentials, i.e.  $\Psi_{nn}(\mathbf{F}, \mathbf{E}_0, \theta)$  or  $\Upsilon_{nn}(\mathbf{F}, \mathbf{D}_0, \theta)$ , data for fields  $\{\mathbf{F}, \mathbf{E}_0, \theta\}$  or  $\{\mathbf{F}, \mathbf{D}_0, \theta\}$ , respectively, are generated as input data according to Algorithm 1. Then, the fields  $\{\mathbf{P}, \mathbf{D}_0\}$  or  $\{\mathbf{P}, \mathbf{E}_0\}$  (generated as synthetic data through direct evaluation of the analytical model or through experiments), respectively, are considered as output variables. The entropy field  $\eta$  is discarded (for synthetic approaches) or directly not available (for experimental procedures). In addition, data for the specific heat capacity  $c_v$  is needed (see Section 4.2.1).
- For  $\eta$ -based potentials, i.e.  $e(\mathbf{F}, \mathbf{D}_0, \eta)$  and  $\Gamma(\mathbf{F}, \mathbf{E}_0, \eta)$ , data for fields  $\{\mathbf{F}, \mathbf{D}_0, \theta\}$  or  $\{\mathbf{F}, \mathbf{E}_0, \theta\}$ , respectively, are generated according to Algorithm 1. Out of the three fields, only two  $\{\mathbf{F}, \mathbf{D}_0\}$  or  $\{\mathbf{F}, \mathbf{E}_0\}$ , respectively, are considered to be input variables. The third field, namely  $\theta$ , is used to solve implicitly the entropy field  $\eta$  according to (52). Then, the fields  $\{\mathbf{P}, \mathbf{D}_0\}$  or  $\{\mathbf{P}, \mathbf{E}_0\}$  (generated as synthetic data through direct evaluation of the analytical model or through experiments), respectively, are considered as output variables in conjunction with  $\theta$ . In addition, data for the specific heat capacity  $c_v$  is needed (see Section 4.2.1).

## 5. Finite Element implementation of nonlinear thermo-electro-mechanics

### 5.1. Continuum formulation

An objective of this study is to integrate neural network-based potentials, calibrated using the strategies outlined in Section 4, into a Finite Element computational framework for the numerical modeling of the governing equations presented in (3), (4) and (5). It is assumed that, irrespective of the chosen thermodynamic potential—whether it be  $\Psi(\mathbf{F}, \mathbf{E}_0, \theta)$ ,  $e(\mathbf{F}, \mathbf{D}_0, \eta)$ ,  $\Gamma(\mathbf{F}, \mathbf{E}_0, \eta)$ , or  $\Upsilon(\mathbf{F}, \mathbf{D}_0, \theta)$ —the corresponding Helmholtz potential,  $\Psi(\mathbf{F}, \mathbf{E}_0, \theta)$ , can always be derived via an appropriate Legendre transformation (as shown in equation (18)). Based on this, the weak forms of the governing equations (3), (4) and (5) can be formulated as follows:

$$\begin{aligned}
\mathcal{W}_\phi &= \int_{\mathcal{B}_0} \rho_0 \dot{\mathbf{v}} \cdot \mathbf{w}_\phi dV + \int_{\mathcal{B}_0} \partial_{\mathbf{F}} \Psi : \partial_{\mathbf{X}} \mathbf{w}_\phi dV - \int_{\mathcal{B}_0} \mathbf{f}_0 \cdot \mathbf{w}_\phi dV - \int_{\partial_t \mathcal{B}_0} \mathbf{t}_0 \cdot \mathbf{w}_\phi dA = 0; \\
\mathcal{W}_\varphi &= - \int_{\mathcal{B}_0} \partial_{\mathbf{D}_0} \Psi \cdot \partial_{\mathbf{X}} w_\varphi dV + \int_{\mathcal{B}_0} \rho_0^e w_\varphi dV + \int_{\partial_\omega \mathcal{B}_0} \omega_0^e \cdot w_\varphi dA = 0; \\
\mathcal{W}_\theta &= - \int_{\mathcal{B}_0} \theta (\partial_\theta \dot{\Psi}) w_\theta dV - \int_{\mathcal{B}_0} \mathbf{Q} \cdot \nabla_0 w_\theta dV - \int_{\mathcal{B}_0} R_\theta w_\theta dV - \int_{\partial_Q \mathcal{B}_0} Q_\theta w_\theta dA = 0,
\end{aligned} \tag{58}$$

where  $\{\phi, \varphi, \theta\} \in \mathbb{V}^\phi \times \mathbb{V}^\varphi \times \mathbb{V}^\theta$  and  $\{\mathbf{w}_\phi, w_\varphi, w_\theta\} \in \mathbb{V}_0^\phi \times \mathbb{V}_0^\varphi \times \mathbb{V}_0^{\theta 4}$ , with

$$\begin{aligned}
\mathbb{V}^\phi &= \{\phi : \mathcal{B}_0 \rightarrow \mathbb{R}^3; (\phi)_i \in H^1(\mathcal{B}_0)\}; & \mathbb{V}_0^\phi &= \{\forall \phi \in \mathbb{V}^\phi; \phi = \mathbf{0} \text{ on } \partial_\phi \mathcal{B}_0\} \\
\mathbb{V}^\varphi &= \{\varphi : \mathcal{B}_0 \rightarrow \mathbb{R}; \varphi \in H^1(\mathcal{B}_0)\}; & \mathbb{V}_0^\varphi &= \{\forall \varphi \in \mathbb{V}^\varphi; \varphi = 0 \text{ on } \partial_\varphi \mathcal{B}_0\} \\
\mathbb{V}^\theta &= \{\theta : \mathcal{B}_0 \rightarrow \mathbb{R}; \theta \in H^1(\mathcal{B}_0)\}; & \mathbb{V}_0^\theta &= \{\forall \theta \in \mathbb{V}^\theta; \theta = 0 \text{ on } \partial_\theta \mathcal{B}_0\}.
\end{aligned} \tag{59}$$

As standard in finite elements, the domain  $\mathcal{B}_0$  described in Section 2.1 and representing a thermo-elastic continuum is sub-divided into a finite set of non-overlapping elements  $e \in \mathbb{E}$  such that

$$\mathcal{B}_0 \approx \mathcal{B}_0^h = \bigcup_{e \in \mathbb{E}} \mathcal{B}_0^e. \tag{60}$$

The unknown fields  $\{\phi, \varphi, \theta\}$  in the weak forms  $\mathcal{W}_\phi$ ,  $\mathcal{W}_\varphi$  and  $\mathcal{W}_\theta$  in (58) are discretised employing the following functional spaces  $\mathbb{V}^{\phi^h} \times \mathbb{V}^{\varphi^h} \times \mathbb{V}^{\theta^h}$  defined as

$$\begin{aligned}
\mathbb{V}^{\phi^h} &= \{\phi \in \mathbb{V}^\phi; \phi^h|_{\mathcal{B}_0^e} = \sum_{a=1}^{n_{\text{node}}^\phi} N_a^\phi \phi_a\}; & \mathbb{V}^{\varphi^h} &= \{\varphi \in \mathbb{V}^\varphi; \varphi^h|_{\mathcal{B}_0^e} = \sum_{a=1}^{n_{\text{node}}^\varphi} N_a^\varphi \varphi_a\}; \\
\mathbb{V}^{\theta^h} &= \{\theta \in \mathbb{V}^\theta; \theta^h|_{\mathcal{B}_0^e} = \sum_{a=1}^{n_{\text{node}}^\theta} N_a^\theta \theta_a\},
\end{aligned} \tag{61}$$

where for any field  $\mathbf{Y} \in \{\phi, \varphi, \theta\}$ ,  $n_{\text{node}}^\mathbf{Y}$  denotes the number of nodes per element of the discretisation associated with the field  $\mathbf{Y}$  and  $N_a^\mathbf{Y} : \mathcal{B}_0^e \rightarrow \mathbb{R}$ , the  $a^{\text{th}}$  shape function used for the interpolation of  $\mathbf{Y}$ . In addition,  $\mathbf{Y}_a$  represents the value of the field  $\mathbf{Y}$  at the  $a^{\text{th}}$  node of a given finite element. Similarly, following a Bubnov-Galerkin approach, the functional spaces for the test functions  $\{\mathbf{w}_\phi, w_\varphi, w_\theta\} \in \mathbb{V}_0^{\phi^h} \times \mathbb{V}_0^{\varphi^h} \times \mathbb{V}_0^{\theta^h}$  are defined as

$$\begin{aligned}
\mathbb{V}_0^{\phi^h} &= \{\forall \phi \in \mathbb{V}^{\phi^h}; \phi = \mathbf{0} \text{ on } \partial_\phi \mathcal{B}_0\}; & \mathbb{V}_0^{\varphi^h} &= \{\forall \varphi \in \mathbb{V}^{\varphi^h}; \varphi = 0 \text{ on } \partial_\varphi \mathcal{B}_0\}; \\
\mathbb{V}_0^{\theta^h} &= \{\forall \theta \in \mathbb{V}^{\theta^h}; \theta = 0 \text{ on } \partial_\theta \mathcal{B}_0\}.
\end{aligned} \tag{62}$$

We have made use of a mid point time integrator where the time derivatives  $\dot{\mathbf{v}}$  and  $\dot{\eta}$  are replaced by the discrete counterparts according to

$$\dot{\mathbf{v}} = \frac{\Delta \mathbf{v}}{\Delta t}; \quad \dot{\eta} = \frac{\Delta \eta}{\Delta t}, \tag{63}$$

where

$$\Delta \mathbf{v} = \mathbf{v} - \mathbf{v}_n; \quad \Delta \eta = \eta - \eta_n \tag{64}$$

---

<sup>4</sup>Notice in that  $\phi$  must satisfy in addition the condition  $J > 0$  a.e.

where  $\bullet_n$  stands for the value of a field  $\bullet$  in the previous time step, and with  $\Delta t$  the time step size used for the discretization. Furthermore, the velocity field is related with the deformed mapping  $\phi$  through the following relationship

$$\frac{\Delta\phi}{\Delta t} = \mathbf{v}_{n+1/2}. \quad (65)$$

where, for any field  $\bullet$ ,  $\bullet_{n+1/2}$  stands for

$$\bullet_{n+1/2} = \bullet + \bullet_n \quad (66)$$

Consideration of the functional spaces for  $\{\phi, \varphi, \theta\}$  and  $\{\mathbf{w}_\phi, w_\varphi, w_\theta\}$  in (61) and (62) enables to obtain the semi-discrete version of  $\{\mathcal{W}_\phi, \mathcal{W}_\varphi, \mathcal{W}_\theta\}$  in (58) in terms of their associated elemental residual contributions, namely

$$\mathcal{W}_\phi = \sum_{e=1}^N \mathbf{w}_{\phi_a} \cdot \mathbf{R}_{a,e}^\phi; \quad \mathcal{W}_\varphi = \sum_{e=1}^N w_{\varphi_a} \cdot \mathbf{R}_{a,e}^\varphi; \quad \mathcal{W}_\theta = \sum_{e=1}^N w_{\theta_a} R_{a,e}^\theta, \quad (67)$$

where  $N$  denotes the number of elements for the underlying discretisation. The residual contributions  $\mathbf{R}_{a,e}^\phi$  and  $R_{a,e}^\theta$  can be expressed as<sup>5</sup>

$$\begin{aligned} \mathbf{R}_{a,e}^\phi &= \int_{\mathcal{B}_0^e} \rho_0 N_a^a \left( 2 \frac{\Delta\phi}{\Delta t^2} - 2 \frac{\mathbf{v}_n}{\Delta t} \right) dV + \int_{\mathcal{B}_0^e} (\partial_{\mathbf{F}} \Psi)_{n+1/2} \nabla_0 N_a^\phi dV - \int_{\mathcal{B}_0^e} N_a^\phi \mathbf{f}_{0_{n+1/2}} dV; \\ \mathbf{R}_{a,e}^\varphi &= - \int_{\mathcal{B}_0^e} (\partial_{\mathbf{E}_0} \Psi)_{n+1/2} \nabla_0 N_a^\varphi dV + \int_{\mathcal{B}_0^e} N_a^\varphi \rho_{0_{n+1/2}}^e dV; \\ R_{a,e}^\theta &= - \int_{\mathcal{B}_0} \frac{\theta_{n+1/2} \Delta (\partial_\theta \Psi)}{\Delta t} N_a^\theta dV - \int_{\mathcal{B}_0} \mathbf{Q}_{n+1/2} \cdot \nabla_0 N_a^\theta dV - \int_{\mathcal{B}_0} R_{\theta n+1/2} N_a^\theta dV. \end{aligned} \quad (68)$$

where use of equation (63) has been made of in the inertial term of the residual  $\mathbf{R}_{a,e}^\phi$  in (68)<sub>a</sub>. A consistent linearisation of the nonlinear residual contributions (68) has been used in this work. Some details of this linearization can be found in the subsequent section

### 5.1.1. Relationship between first and second derivatives of $\Psi(\mathbf{F}, \mathbf{E}_0, \theta)$ and alternative potentials

The coupled weak forms presented in equation (58) and their residuals in (68) are expressed in terms of the derivatives of the Helmholtz potential,  $\Psi(\mathbf{F}, \mathbf{E}_0, \theta)$ . However, the fundamental thermodynamic potential governing the constitutive model can alternatively be one of the three other thermodynamic potentials:  $e(\mathbf{F}, \mathbf{D}_0, \eta)$ ,  $\Gamma(\mathbf{F}, \mathbf{E}_0, \eta)$ , or  $\Upsilon(\mathbf{F}, \mathbf{D}_0, \theta)$ . In such cases, the derivatives in (58) and (68), specifically  $\{\partial_{\mathbf{F}} \Psi, \partial_{\mathbf{E}_0} \Psi, \partial_\theta \Psi\}$ , must be redefined in terms of these alternative potentials. This is accomplished through the appropriate Legendre transformation (refer to (18)).

This transformation is not only essential for obtaining the first derivatives but is also crucial for deriving the second derivatives of  $\Psi(\mathbf{F}, \mathbf{E}_0, \theta)$ , i.e., the components of its Hessian, when the primary thermodynamic potential is either  $e(\mathbf{F}, \mathbf{D}_0, \eta)$ ,  $\Gamma(\mathbf{F}, \mathbf{E}_0, \eta)$ , or  $\Upsilon(\mathbf{F}, \mathbf{D}_0, \theta)$ . The following sections will detail the procedures for relating both the first derivatives of  $\Psi(\mathbf{F}, \mathbf{E}_0, \theta)$  and the components of its Hessian to their respective counterparts in the potentials  $e(\mathbf{F}, \mathbf{D}_0, \eta)$ ,  $\Gamma(\mathbf{F}, \mathbf{E}_0, \eta)$ , or  $\Upsilon(\mathbf{F}, \mathbf{D}_0, \theta)$ .

---

<sup>5</sup>For simplicity, the external contributions on the boundary of the continuum and associated with  $\mathbf{t}_0$  and  $\mathbf{Q}_\theta$  have not been included in (68).

### 5.1.2. Potential $\Upsilon$

In this case we consider the case when the underlying thermo-electro-mechanical constitutive model is  $\Upsilon(\mathbf{F}, \mathbf{D}_0, \theta)$ . The Legendre transformation in equation (18)<sub>b</sub> implies that the field  $\mathbf{D}_0 := -\partial_{\mathbf{E}_0}\Psi$  must be considered as a function of the fields  $\{\mathbf{F}, \mathbf{E}_0, \theta\}$ , namely

$$\Upsilon = \Upsilon(\mathbf{F}, \mathbf{D}_0(\mathbf{F}, \mathbf{E}_0, \theta), \theta) \quad (69)$$

and then,  $\mathbf{D}_0 := -\partial_{\mathbf{E}_0}\Psi$  is implicitly solved from this equation

$$\mathbf{E}_0 = \partial_{\mathbf{D}_0}\Upsilon(\mathbf{F}, \mathbf{D}_0(\mathbf{F}, \mathbf{E}_0, \theta), \theta) \quad (70)$$

Once  $\mathbf{D}_0 := -\partial_{\mathbf{E}_0}\Psi$  is obtained,  $\mathbf{P} := \partial_{\mathbf{F}}\Psi$  and  $\eta := -\partial_{\theta}\Psi$  can be obtained as

$$\begin{aligned} \partial_{\mathbf{F}}\Psi(\mathbf{F}, \mathbf{E}_0, \theta) &= \partial_{\mathbf{F}}\Upsilon(\mathbf{F}, \mathbf{D}_0(\mathbf{F}, \mathbf{E}_0, \theta), \theta); \\ \partial_{\theta}\Psi(\mathbf{F}, \mathbf{E}_0, \theta) &= \partial_{\theta}\Upsilon(\mathbf{F}, \mathbf{D}_0(\mathbf{F}, \mathbf{E}_0, \theta), \theta); \end{aligned} \quad (71)$$

The components of the Hessian operator of  $\Psi(\mathbf{F}, \mathbf{E}_0, \theta)$ , needed for the consistent linearization of (68) can then be related to the components of the Hessian operator of  $\Upsilon$  by considering  $\mathbf{D}_0$  as a function of  $\{\mathbf{F}, \mathbf{E}_0, \theta\}$ , as in (69), yielding the following relationships

$$\begin{aligned} \partial_{\mathbf{FF}}^2\Psi &= \partial_{\mathbf{FF}}^2\Upsilon - \partial_{\mathbf{FD}_0}^2\Upsilon \cdot \partial_{\mathbf{E}_0\mathbf{F}}\Psi; & \partial_{\mathbf{FE}_0}^2\Psi &= -\partial_{\mathbf{FD}_0}^2\Upsilon \cdot \partial_{\mathbf{E}_0\mathbf{E}_0}\Psi; & \partial_{\mathbf{F}\theta}^2\Psi &= \partial_{\mathbf{F}\theta}^2\Upsilon - \partial_{\mathbf{FD}_0}^2\Upsilon \cdot \partial_{\mathbf{E}_0\theta}\Psi \\ \partial_{\mathbf{E}_0\mathbf{F}}^2\Psi &= \left(\partial_{\mathbf{E}_0\mathbf{F}}^2\Psi\right)^T; & \partial_{\mathbf{E}_0\mathbf{E}_0}^2\Psi &= -\left(\partial_{\mathbf{D}_0\mathbf{D}_0}^2\Upsilon\right)^{-1}; & \partial_{\mathbf{E}_0\theta}^2\Psi &= \left(\partial_{\theta\mathbf{E}_0}^2\Psi\right)^T \\ \partial_{\theta\mathbf{F}}^2\Psi &= \left(\partial_{\theta\mathbf{F}}^2\Psi\right)^T; & \partial_{\theta\mathbf{E}_0}^2\Psi &= -\partial_{\theta\mathbf{D}_0}^2\Upsilon \cdot \partial_{\mathbf{E}_0\mathbf{E}_0}\Psi; & \partial_{\theta\theta}^2\Psi &= \partial_{\theta\theta}^2\Upsilon - \partial_{\theta\mathbf{D}_0}^2\Upsilon \cdot \partial_{\mathbf{E}_0\theta}\Psi \end{aligned} \quad (72)$$

### 5.1.3. Potential $\Gamma$

Let us know consider the case when the underlying thermo-electro-mechanical constitutive model is  $\Gamma(\mathbf{F}, \mathbf{E}_0, \eta)$ . In this case, the Legendre transformation in equation (18)<sub>c</sub> implies that the field  $\eta := -\partial_{\theta}\Psi$  must be considered as a function of the fields  $\{\mathbf{F}, \mathbf{E}_0, \theta\}$ , namely

$$\Gamma = \Gamma(\mathbf{F}, \mathbf{E}_0, \eta(\mathbf{F}, \mathbf{E}_0, \theta)) \quad (73)$$

and then,  $\eta := -\partial_{\theta}\Psi$  is implicitly solved from this equation

$$\theta = \partial_{\theta}\Gamma(\mathbf{F}, \mathbf{E}_0, \eta(\mathbf{F}, \mathbf{E}_0, \theta)) \quad (74)$$

Once  $\eta := -\partial_{\theta}\Psi$  is obtained,  $\mathbf{P} = \partial_{\mathbf{F}}\Psi$  and  $\mathbf{D}_0 = -\partial_{\mathbf{E}_0}\Psi$  can be obtained as

$$\begin{aligned} \partial_{\mathbf{F}}\Psi(\mathbf{F}, \mathbf{E}_0, \theta) &= \partial_{\mathbf{F}}\Gamma(\mathbf{F}, \mathbf{D}_0, \eta(\mathbf{F}, \mathbf{E}_0, \theta)); \\ \partial_{\mathbf{E}_0}\Psi(\mathbf{F}, \mathbf{E}_0, \theta) &= \partial_{\mathbf{E}_0}\Gamma(\mathbf{F}, \mathbf{D}_0, \eta(\mathbf{F}, \mathbf{E}_0, \theta)); \end{aligned} \quad (75)$$

The components of the Hessian operator of  $\Psi(\mathbf{F}, \mathbf{E}_0, \theta)$ , needed for the consistent linearization of (68) can then be related to the components of the Hessian operator of  $\Gamma$  by considering  $\eta$  as a function of  $\{\mathbf{F}, \mathbf{E}_0, \theta\}$ , as in (73), yielding the following relationships

$$\begin{aligned} \partial_{\mathbf{FF}}^2\Psi &= \partial_{\mathbf{FF}}^2\Gamma - \partial_{\mathbf{F}\eta}^2\Gamma \cdot \partial_{\theta\mathbf{F}}\Psi; & \partial_{\mathbf{FE}_0}^2\Psi &= \partial_{\mathbf{FE}_0}^2\Gamma - \partial_{\mathbf{F}\eta}^2\Gamma \cdot \partial_{\theta\mathbf{E}_0}\Psi; & \partial_{\mathbf{F}\theta}^2\Psi &= -\partial_{\mathbf{F}\eta}^2\Gamma \cdot \partial_{\theta\theta}\Psi \\ \partial_{\mathbf{E}_0\mathbf{F}}^2\Psi &= \left(\partial_{\mathbf{E}_0\mathbf{F}}^2\Psi\right)^T; & \partial_{\mathbf{E}_0\mathbf{E}_0}^2\Psi &= -\partial_{\mathbf{E}_0\mathbf{E}_0}^2\Gamma - \partial_{\mathbf{E}_0\eta}^2\Gamma \cdot \partial_{\theta\mathbf{E}_0}\Psi; & \partial_{\mathbf{E}_0\theta}^2\Psi &= -\partial_{\mathbf{E}_0\eta}^2\Gamma \cdot \partial_{\theta\theta}\Psi \\ \partial_{\theta\mathbf{F}}^2\Psi &= \left(\partial_{\theta\mathbf{F}}^2\Psi\right)^T; & \partial_{\theta\mathbf{E}_0}^2\Psi &= \left(\partial_{\theta\mathbf{E}_0}^2\Psi\right)^T; & \partial_{\theta\theta}^2\Psi &= -\left(\partial_{\eta\eta}^2\Gamma\right)^{-1} \end{aligned} \quad (76)$$

### 5.1.4. Potential $e$

Finally, let us consider the case when the underlying thermo-electro-mechanical constitutive model is  $e(\mathbf{F}, \mathbf{D}_0, \eta)$ . In this case, the Legendre transformation in equation (18)<sub>a</sub> implies that both fields  $\mathbf{D}_0 := -\partial_{\mathbf{E}_0}\Psi$  and  $\eta := -\partial_\theta\Psi$  must be considered as functions of the fields  $\{\mathbf{F}, \mathbf{E}_0, \theta\}$ , namely

$$e = e(\mathbf{F}, \mathbf{D}_0(\mathbf{F}, \mathbf{E}_0, \theta), \eta(\mathbf{F}, \mathbf{E}_0, \theta)) \quad (77)$$

and then,  $\mathbf{D}_0 := -\partial_{\mathbf{E}_0}\Psi$  and  $\eta := -\partial_\theta\Psi$  are simultaneously implicitly solved from these equations

$$\begin{aligned} \mathbf{E}_0 &= \partial_{\mathbf{D}_0}e(\mathbf{F}, \mathbf{D}_0(\mathbf{F}, \mathbf{E}_0, \theta), \eta(\mathbf{F}, \mathbf{E}_0, \theta)); \\ \theta &= \partial_\eta e(\mathbf{F}, \mathbf{D}_0(\mathbf{F}, \mathbf{E}_0, \theta), \eta(\mathbf{F}, \mathbf{E}_0, \theta)) \end{aligned} \quad (78)$$

Once  $\mathbf{D}_0 := -\partial_{\mathbf{E}_0}\Psi$  and  $\eta := -\partial_\theta\Psi$  are obtained,  $\mathbf{P} = \partial_{\mathbf{F}}\Psi$  can be obtained as

$$\partial_{\mathbf{F}}\Psi(\mathbf{F}, \mathbf{E}_0, \theta) = \partial_{\mathbf{F}}e(\mathbf{F}, \mathbf{D}_0(\mathbf{F}, \mathbf{E}_0, \theta), \eta(\mathbf{F}, \mathbf{E}_0, \theta)). \quad (79)$$

The components of the Hessian operator of  $\Psi(\mathbf{F}, \mathbf{E}_0, \theta)$ , needed for the consistent linearization of (68) can then be related to the components of the Hessian operator of  $e$  by considering  $\mathbf{D}_0$  and  $\eta$  as functions of  $\{\mathbf{F}, \mathbf{E}_0, \theta\}$ , as in (77), yielding the following relationships

$$\begin{aligned} \partial_{\mathbf{FF}}^2\Psi &= \partial_{\mathbf{FF}}^2e - \partial_{\mathbf{FD}_0}^2e \cdot \partial_{\mathbf{E}_0\mathbf{F}}\Psi - \partial_{\mathbf{F}\eta}^2e \cdot \partial_{\theta\mathbf{F}}\Psi; & \partial_{\mathbf{FE}_0}^2\Psi &= -\partial_{\mathbf{FD}_0}^2e \cdot \partial_{\mathbf{E}_0\mathbf{E}_0}\Psi - \partial_{\mathbf{F}\eta}^2e \cdot \partial_{\theta\mathbf{E}_0}\Psi; \\ \partial_{\mathbf{F}\theta}^2\Psi &= -\partial_{\mathbf{FD}_0}^2e \cdot \partial_{\mathbf{E}_0\theta}\Psi - \partial_{\mathbf{F}\eta}^2e \cdot \partial_{\theta\theta}\Psi; & \partial_{\mathbf{E}_0\mathbf{F}}^2\Psi &= \left(\partial_{\mathbf{FE}_0}^2\Psi\right)^T; \\ \partial_{\theta\mathbf{F}}^2\Psi &= \left(\partial_{\mathbf{F}\theta}^2\Psi\right)^T; & \begin{bmatrix} \partial_{\mathbf{E}_0\mathbf{E}_0}^2\Psi & \partial_{\mathbf{E}_0\theta}^2\Psi \\ \partial_{\theta\mathbf{E}_0}^2\Psi & \partial_{\theta\theta}^2\Psi \end{bmatrix} &= -\begin{bmatrix} \partial_{\mathbf{D}_0\mathbf{D}_0}^2e & \partial_{\mathbf{D}_0\eta}^2e \\ \partial_{\eta\mathbf{D}_0}^2e & \partial_{\eta\eta}^2e \end{bmatrix}^{-1} \end{aligned} \quad (80)$$

## 6. Calibration and validation of the thermodynamic potentials

This section presents the calibration results for various types of neural network-based thermodynamic potentials, namely  $\Psi_{nn}$ ,  $e_{nn}$ ,  $\Gamma_{nn}$  and  $\Upsilon_{nn}$ , calibrated according to both calibration strategies described in Sections 4.1 and 4.2.

### 6.1. Calibration strategy 1

We begin showing the calibration results by using Sobolev-type calibration strategy 1.

#### 6.1.1. Neural network architecture's influence: $\Psi_{nn}$ neural network-based ground truth models

The objective of this preliminary study is to investigate a specific neural network-based thermodynamic potential, namely  $\Psi_{nn}(\mathbf{F}, \mathbf{E}_0, \theta)$ . Our focus is to assess how variations in the neural network architecture influence the accuracy of the potential's calibration. The network architecture is characterized by the number of layers,  $n_L + 1$ , and an equal number of neurons per layer, denoted as  $n_n$ . By varying these parameters, we track the  $R^2$  values of the second-order derivatives of the potential— $R^2$  in the derivatives of the potential, namely  $R^2(\partial_{\mathbf{F}}^2\Psi_{nn})$ ,  $R^2(\partial_{\mathbf{E}_0}^2\Psi_{nn})$  and  $R^2(\partial_\theta^2\Psi_{nn})$ —for both training and testing datasets. It is important to note that the training data, used for calibrating the potential across all architectures, constitutes 20% of the testing dataset.

Table 8 shows the results obtained for the calibrated models  $\Psi_{nn}$ , not only across different neural network architectures but also when employing the various models described in Section 3.5. These models represent both the purely mechanical and electro-mechanical contributions of the ground truth Helmholtz strain energy model used for the calibration of all the potentials. The results obtained in this table indicate that in general, the optimization algorithm used for the calibration of the models (Adam algorithm with a learning rate of 0.001) attains a very satisfactory local minimum.

	$n_L + 1$	2	3	4	2	3	4
	$n_n$	8	8	8	16	16	16
<b>MRI/D</b>	$R^2(\partial_F \Psi)$	0.9994	0.9999	0.9999	0.9998	0.9999	0.9999
	$R^2(\partial_{E_0} \Psi)$	0.9999	0.9999	0.99999	0.9999	0.9999	0.9999
	$R^2(\partial_\theta \Psi)$	0.9999	0.9999	0.9999	0.9999	0.9999	0.9999
<b>QMRI/D</b>	$R^2(\partial_F \Psi)$	0.9989	0.9989	0.9999	0.9999	0.9999	0.9999
	$R^2(\partial_{E_0} \Psi)$	0.9995	0.9996	0.9999	0.9999	0.9999	0.9999
	$R^2(\partial_\theta \Psi)$	0.9999	0.9999	0.99999	0.9999	0.9999	0.9999
<b>Y/D</b>	$R^2(\partial_F \Psi)$	0.9992	0.9999	0.9999	0.9999	0.9999	0.9999
	$R^2(\partial_{E_0} \Psi)$	0.9994	0.9999	0.9999	0.9999	0.9999	0.9999
	$R^2(\partial_\theta \Psi)$	0.9999	0.9999	0.99999	0.9999	0.9999	0.9999
<b>G/D</b>	$R^2(\partial_F \Psi)$	0.9999	0.9998	0.9998	0.9998	0.9998	0.9999
	$R^2(\partial_{E_0} \Psi)$	0.9999	0.9999	0.9999	0.9999	0.9999	0.9999
	$R^2(\partial_\theta \Psi)$	0.9999	0.9999	0.99999	0.9999	0.9999	0.9999
<b>TI/D</b>	$R^2(\partial_F \Psi)$	0.9996	0.9996	0.9999	0.9999	0.9999	0.9999
	$R^2(\partial_{E_0} \Psi)$	0.9994	0.9992	0.9999	0.9999	0.9999	0.9999
	$R^2(\partial_\theta \Psi)$	0.9999	0.9999	0.99999	0.9999	0.9999	0.9999
<b>MR/ES</b>	$R^2(\partial_F \Psi)$	0.9996	0.9995	0.9995	0.9999	0.9998	0.9999
	$R^2(\partial_{E_0} \Psi)$	0.9998	0.9998	0.9998	0.9999	0.9998	0.9999
	$R^2(\partial_\theta \Psi)$	0.9999	0.9999	0.99999	0.9999	0.9999	0.9999

Table 6: **Calibration Strategy 1.** Values of the  $R^2(\partial_F \Psi)$ ,  $R^2(\partial_{E_0} \Psi)$  and  $R^2(\partial_\theta \Psi)$  obtained in the calibration of  $\Psi_{nn}$  (hence using the training dataset) using the purely mechanical (in red) and electro-mechanical (in blue) contributions of the ground truth Helmholtz strain energy model used for the calibration.

Importantly, the calibrated models  $\Psi_{nn}(\mathbf{F}, \mathbf{E}_0, \theta)$  have been evaluated against an independent dataset not included in the original training set. This larger dataset, referred to as the test dataset, has been used to assess the performance of all the ground truth models considered, utilizing a specific neural network architecture. In this study, we have focused on models comprising five layers with eight neurons per layer. The correlation results, presented in Figure 7, demonstrate the calibrated models' robust capability to accurately predict the responses of the ground truth models across a significantly broader dataset than the training set.

We conducted additional testing of the calibrated models in scenarios beyond those included in the training set. It is important to note that both the training and testing sets were generated using a similar in-silico data generation strategy, as outlined in Section 4.1.3 and based on the methodology of [? ]. Our objective is to further evaluate the calibrated potentials using a distinct data generation strategy, in which the deformation gradient tensor and the electric field are defined according to

$$\mathbf{F} = \begin{bmatrix} \lambda & \gamma & 0 \\ 0 & \lambda & 0 \\ 0 & 0 & 1/\lambda^2 \end{bmatrix}; \quad 1 \leq \lambda \leq 1.8; \quad \mathbf{E}_0 = \begin{bmatrix} \alpha \\ \alpha \\ 0 \end{bmatrix} \quad 0 \leq \alpha \leq 1.5\sqrt{\frac{\mu}{\varepsilon}} \quad (81)$$

The objective is to assess the agreement between the derivatives of the calibrated model,  $\Psi_{nn}(\mathbf{F}, \mathbf{E}_0, \theta)$ , and those of the ground truth model across various temperature values for the specified experimental setup. Figure 8 illustrates this comparison, focusing on the neural network-based potential  $\Psi_{nn}(\mathbf{F}, \mathbf{E}_0, \theta)$  and a single ground truth constitutive model. The figure demonstrates a remarkable alignment between the calibrated and ground truth models, highlighting the calibrated model's capacity to accurately predict the ground truth response, even in scenarios outside its training domain.

### 6.1.2. Generalization results for all the thermodynamical potentials

In the previous section, we focused exclusively on the calibration of Helmholtz-type neural network-based potentials, specifically  $\Psi_{nn}(\mathbf{F}, \mathbf{E}_0, \theta)$ . The objective of this section, however, is to demonstrate that, while we have primarily considered a Helmholtz-type ground truth potential  $\Psi(\mathbf{F}, \mathbf{E}_0, \theta)$ , we can successfully calibrate neural network-based potentials corresponding to alternative formulations, namely  $e_{nn}(\mathbf{F}, \mathbf{D}_0, \eta)$ ,  $\Upsilon_{nn}(\mathbf{F}, \mathbf{D}_0, \theta)$  and  $\Gamma_{nn}(\mathbf{F}, \mathbf{E}_0, \eta)$ , as outlined in Section 4.1.1. To illustrate this capability, we consider the following case:

- fixed neural network architecture with 4 hidden layers and 8 neurons
- ground truth model with  $\Psi_m$  corresponding with a Mooney-Rivlin model and  $\Psi_{em}$  with an ideal dielectric model.

Under such scenario, Figure 9 presents the correlation results for the test dataset, which is larger than the training dataset, for the four potentials, namely  $\Psi_{nn}(\mathbf{F}, \mathbf{E}_0, \theta)$ ,  $e_{nn}(\mathbf{F}, \mathbf{D}_0, \eta)$ ,  $\Upsilon_{nn}(\mathbf{F}, \mathbf{D}_0, \theta)$  and  $\Gamma_{nn}(\mathbf{F}, \mathbf{E}_0, \eta)$ . The figure demonstrates an excellent agreement between the predictions made by the calibrated potentials and the ground truth model, confirming the reliability of the calibrated models in predicting the behavior of the ground truth.

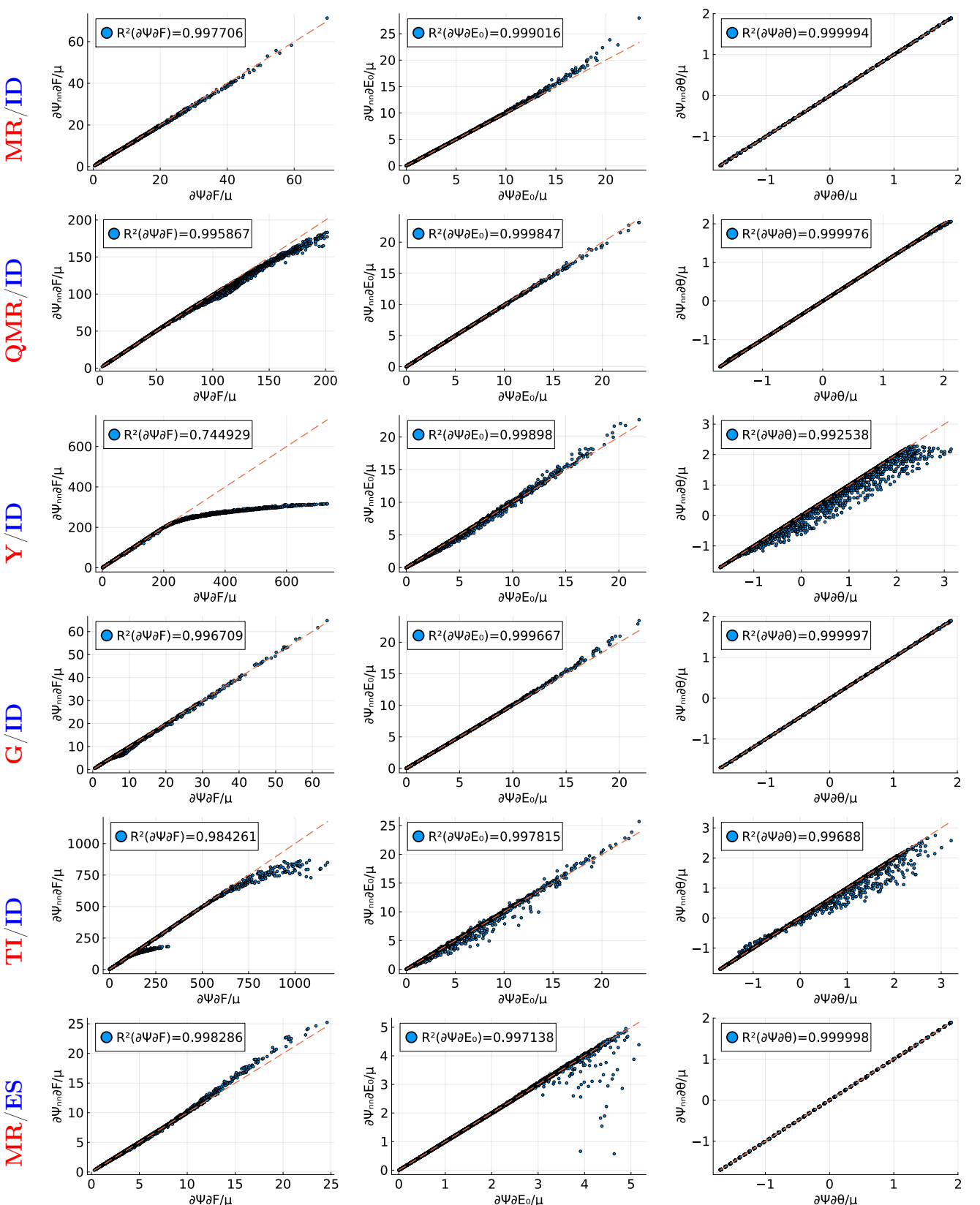


Figure 7: **Calibration Strategy 1.** Correlation of prediction  $\{\partial_F\Psi_{nn}, \partial_{E_0}\Psi_{nn}, \partial_\theta\Psi_{nn}\}$  and testing data  $\{\partial_F\Psi, \partial_{E_0}\Psi, \partial_\theta\Psi\}$  using the purely mechanical (in red) and electro-mechanical (in blue) contributions of the ground truth Helmholtz strain energy model used for the calibration. The training data represents a subset of the testing data containing the 20% of the data in the latter. In all cases we have considered an architecture of 4 layers and 8 neurons per layer.

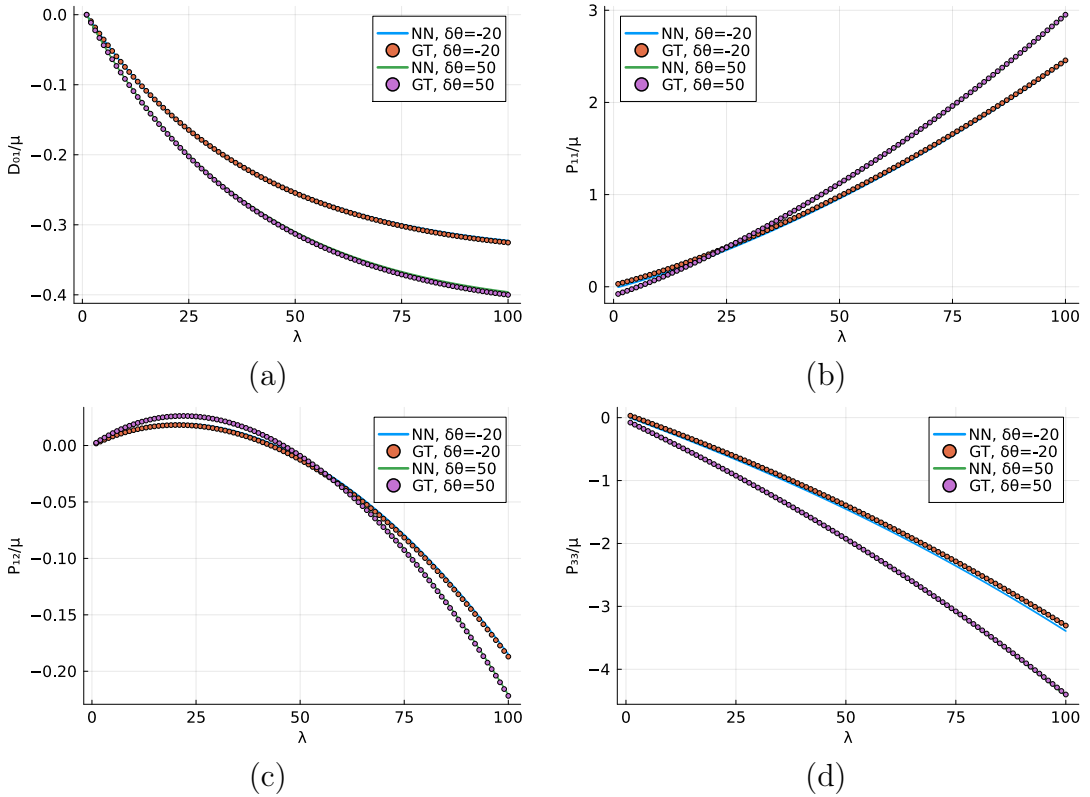


Figure 8: **Calibration Strategy 1.** Prediction of calibrated model  $\Psi_{nn}(\mathbf{F}, \mathbf{E}_0, \theta)$  and ground truth model across various temperature values for the experimental setup in (81). The ground truth model  $\Psi(\mathbf{F}, \mathbf{E}_0, \theta)$  considers a Mooney-Rivlin model for the mechanical contribution, i.e.  $Psi_m$  and an ideal dielectric model for the electro-mechanical contribution, i.e.  $\Psi_{em}$ .

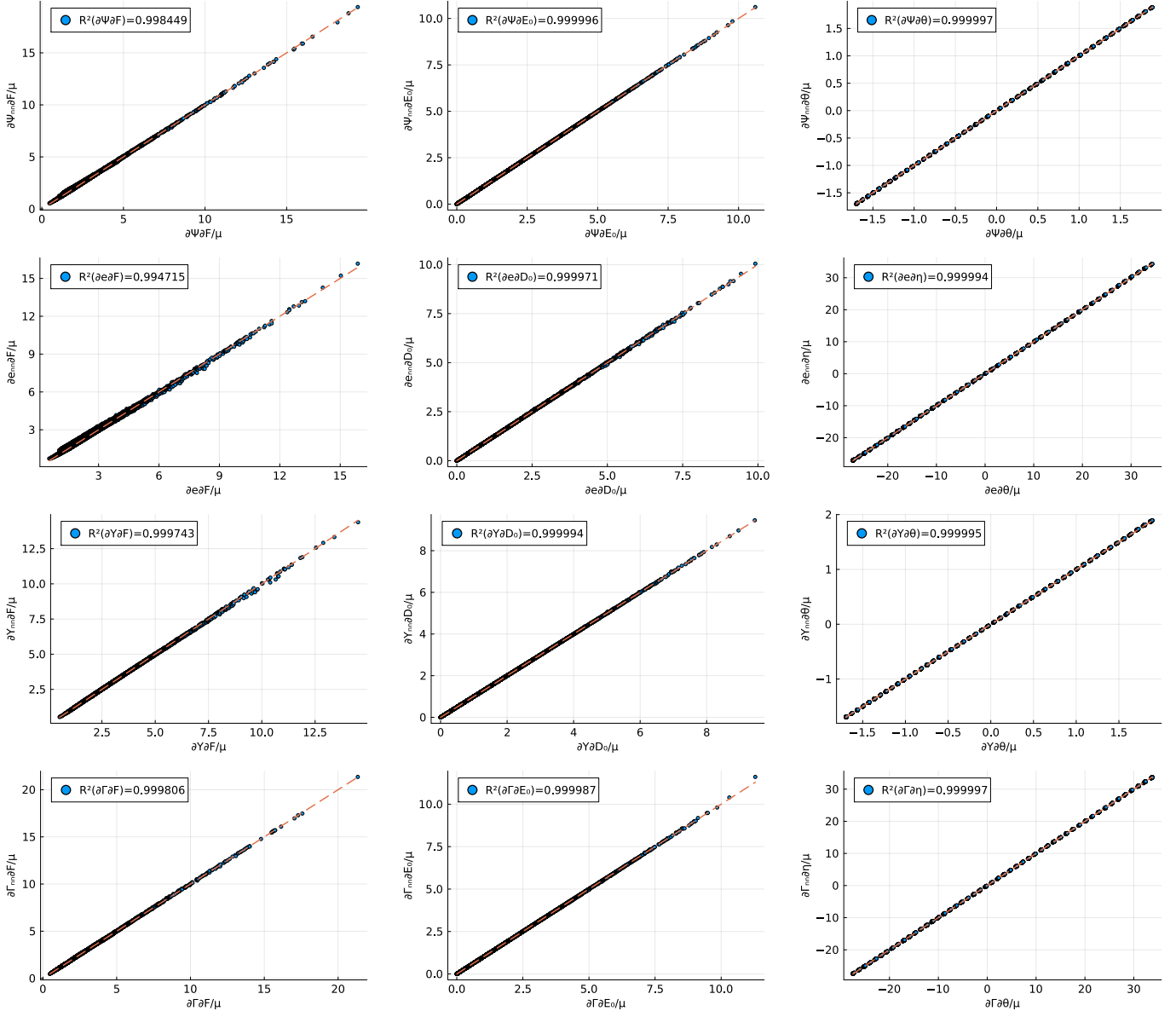


Figure 9: **Calibration Strategy 1.** Correlation of prediction ,  $\{\partial_F\Psi_{nn}, \partial_{E_0}\Psi_{nn}, \partial_\theta\Psi_{nn}\}$ ,  $\{\partial_F e_{nn}, \partial_{D_0}d_{nn}, \partial_\eta e_{nn}\}$ ,  $\{\partial_F Y_{nn}, \partial_{D_0}Y_{nn}, \partial_\theta Y_{nn}\}$  and  $\{\partial_F \Gamma_{nn}, \partial_{E_0}\Gamma_{nn}, \partial_\theta \Gamma_{nn}\}$  and their testing data counterparts. In all cases we have considered an architecture of 4 layers and 8 neurons per layer.

### 6.1.3. Polyconvex calibration

#### STUDY OF POLYCONVEXITY FOR POTENTIAL e

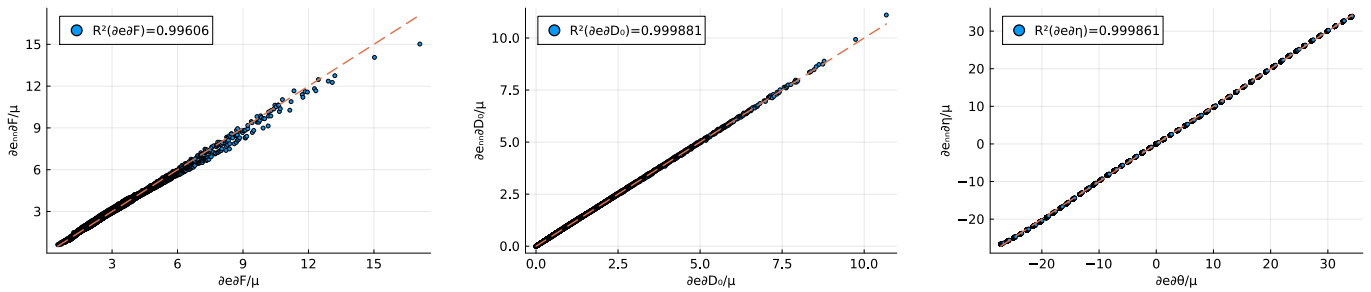


Figure 10: Calibration Strategy 1.

### 6.1.4. Generalization to unseen experiments

## 6.2. Calibration strategy 2: $\theta$ -based potentials

### 6.2.1. Neural network architecture's influence: $\Psi_{nn}$ neural network-based ground truth models

	$n_L + 1$	1	2	3	4	5	1	2	3	4	5
	$n_n$	8	8	8	8	8	16	16	16	16	16
MB/ ID	$R^2(\partial_F \Psi)$	1	1	1	1	1	1	1	1	1	1
	$R^2(\partial_F \Psi)$	1	1	1	1	1	1	1	1	1	1
	$R^2(\partial_F \Psi)$	1	1	1	1	1	1	1	1	1	1
QMR/ ID	$R^2(\partial_F \Psi)$	1	1	1	1	1	1	1	1	1	1
	$R^2(\partial_F \Psi)$	1	1	1	1	1	1	1	1	1	1
	$R^2(\partial_F \Psi)$	1	1	1	1	1	1	1	1	1	1
Y/ ID	$R^2(\partial_F \Psi)$	1	1	1	1	1	1	1	1	1	1
	$R^2(\partial_F \Psi)$	1	1	1	1	1	1	1	1	1	1
	$R^2(\partial_F \Psi)$	1	1	1	1	1	1	1	1	1	1
G/ ID	$R^2(\partial_F \Psi)$	1	1	1	1	1	1	1	1	1	1
	$R^2(\partial_F \Psi)$	1	1	1	1	1	1	1	1	1	1
	$R^2(\partial_F \Psi)$	1	1	1	1	1	1	1	1	1	1
TI/ ID	$R^2(\partial_F \Psi)$	1	1	1	1	1	1	1	1	1	1
	$R^2(\partial_F \Psi)$	1	1	1	1	1	1	1	1	1	1
	$R^2(\partial_F \Psi)$	1	1	1	1	1	1	1	1	1	1
MR/ ES	$R^2(\partial_F \Psi)$	1	1	1	1	1	1	1	1	1	1
	$R^2(\partial_F \Psi)$	1	1	1	1	1	1	1	1	1	1
	$R^2(\partial_F \Psi)$	1	1	1	1	1	1	1	1	1	1

Table 7

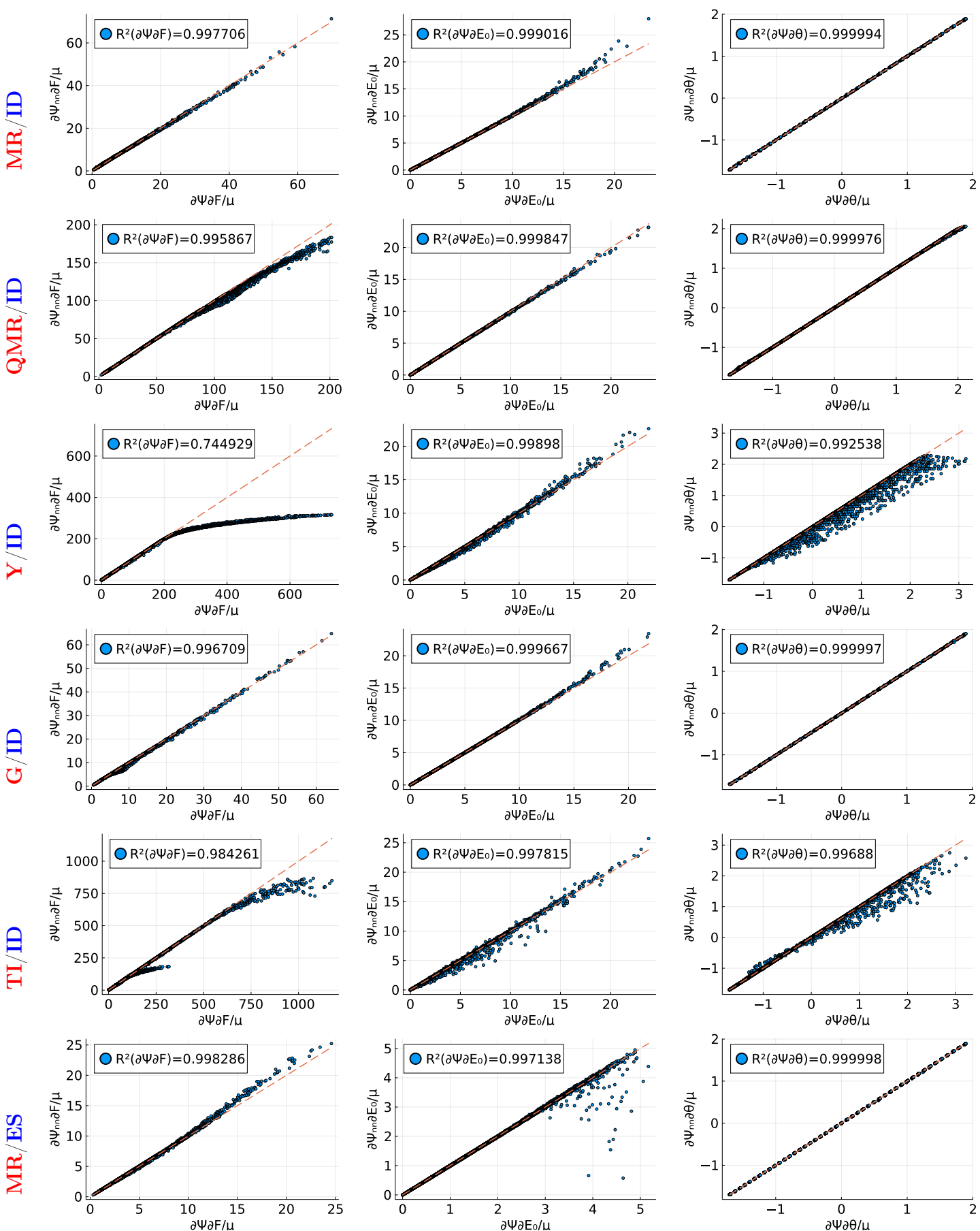


Figure 11

### 6.2.2. Generalization results for $\Upsilon(\mathbf{F}, \mathbf{D}_0, \theta)$

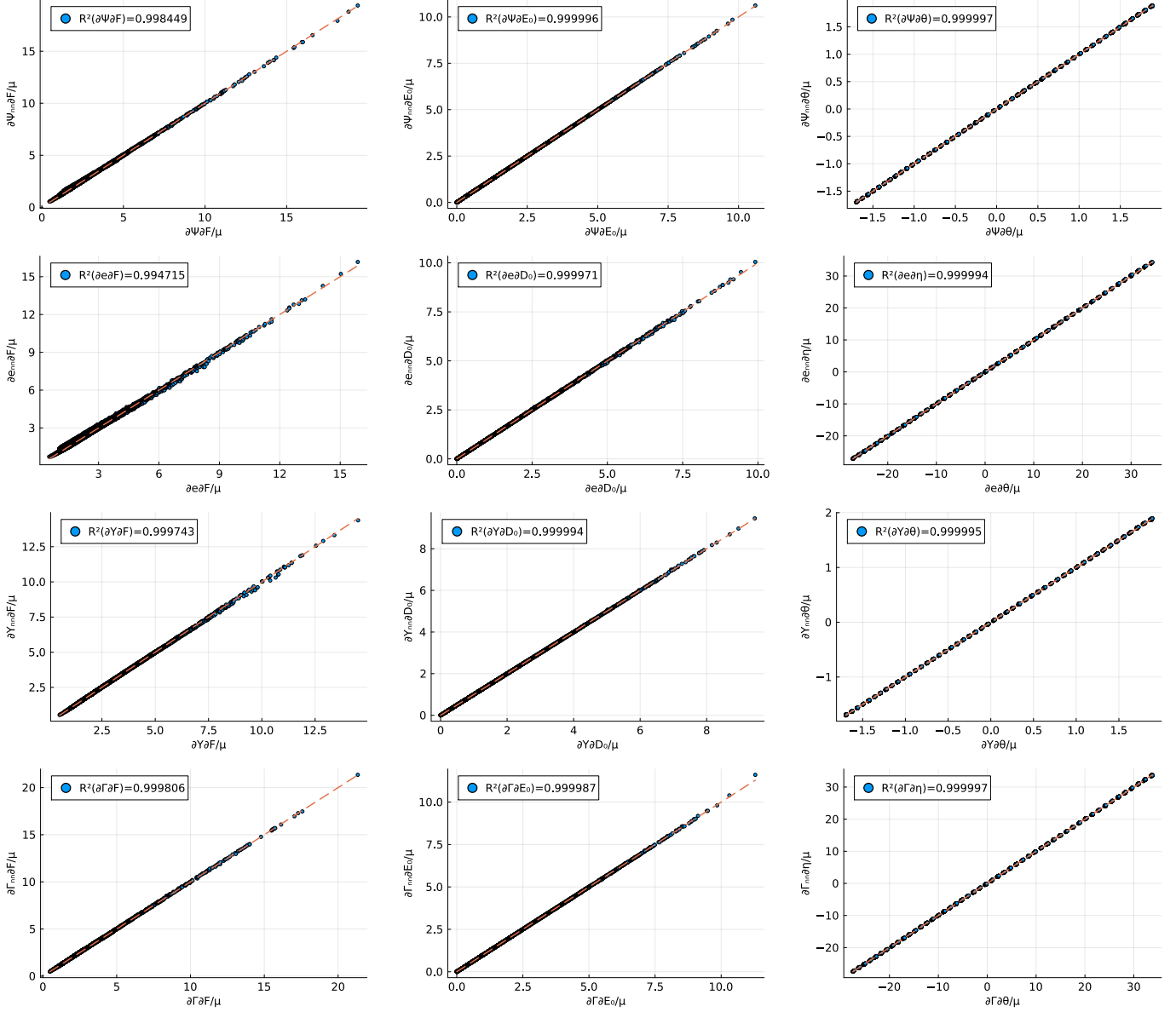


Figure 12: Numerical example 1. Evolution of: (a) angular momentum  $\mathbf{J}$ , (b) linear momentum  $\mathbf{L}$ , (c) global entropy  $\tilde{\eta} = \int_{\mathcal{B}_0} \eta dV$ , (d) Hamiltonian  $\mathcal{H}$  in (??), (e) increment of Hamiltonian  $\Delta\mathcal{H}$  for both the Mid-Point and the new EM time integrator. Finally, (f), zoomed detail of the increment of the Hamiltonian  $\Delta\mathcal{H}$  for the new EM time integrator. Results obtained for **Mesh2** with  $\alpha_{CFL} = 2.2955$  ( $\Delta t = 0.2$  s).

### 6.3. Calibration strategy 2: $\eta$ -based potentials

#### 6.3.1. Neural network architecture's influence: $e_{nn}$ neural network-based ground truth models

	$n_L + 1$	1	2	3	4	5	1	2	3	4	5
	$n_n$	8	8	8	8	8	16	16	16	16	16
<b>MR/ID</b>	$R^2(\partial_F \Psi)$	1	1	1	1	1	1	1	1	1	1
	$R^2(\partial_F \Psi)$	1	1	1	1	1	1	1	1	1	1
	$R^2(\partial_F \Psi)$	1	1	1	1	1	1	1	1	1	1
<b>QMR/ID</b>	$R^2(\partial_F \Psi)$	1	1	1	1	1	1	1	1	1	1
	$R^2(\partial_F \Psi)$	1	1	1	1	1	1	1	1	1	1
	$R^2(\partial_F \Psi)$	1	1	1	1	1	1	1	1	1	1
<b>Y/ID</b>	$R^2(\partial_F \Psi)$	1	1	1	1	1	1	1	1	1	1
	$R^2(\partial_F \Psi)$	1	1	1	1	1	1	1	1	1	1
	$R^2(\partial_F \Psi)$	1	1	1	1	1	1	1	1	1	1
<b>G/ID</b>	$R^2(\partial_F \Psi)$	1	1	1	1	1	1	1	1	1	1
	$R^2(\partial_F \Psi)$	1	1	1	1	1	1	1	1	1	1
	$R^2(\partial_F \Psi)$	1	1	1	1	1	1	1	1	1	1
<b>TI/ID</b>	$R^2(\partial_F \Psi)$	1	1	1	1	1	1	1	1	1	1
	$R^2(\partial_F \Psi)$	1	1	1	1	1	1	1	1	1	1
	$R^2(\partial_F \Psi)$	1	1	1	1	1	1	1	1	1	1
<b>MR/ES</b>	$R^2(\partial_F \Psi)$	1	1	1	1	1	1	1	1	1	1
	$R^2(\partial_F \Psi)$	1	1	1	1	1	1	1	1	1	1
	$R^2(\partial_F \Psi)$	1	1	1	1	1	1	1	1	1	1

Table 8

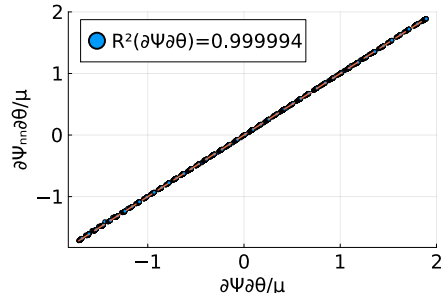
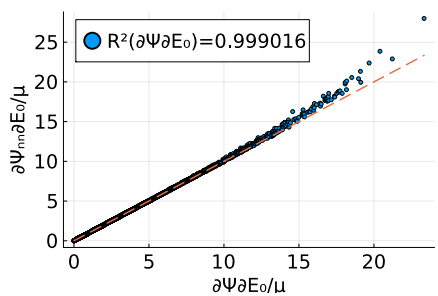
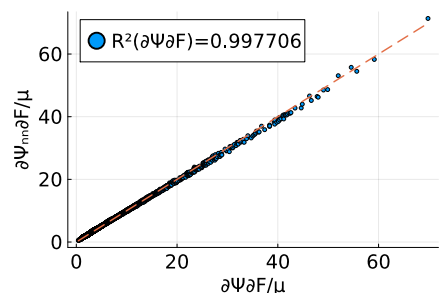


Figure 13

## 6.4. Finite Element numerical experiments

The objective of this section is to study the performance of the newly proposed EM time integration scheme presented in equation (??) in a variety of challenging examples, with the aim of comparing the long-term stability of the new time integrator against that of the classical midpoint rule.

### 6.4.1. Numerical Example 1

The objectives of this example are:

- **O1** To carry out a thorough analysis of the stability and robustness of the proposed EM time integrator comparing it against of the mid-point rule time integrator as a function of the Courant-Friedrich-Lowy number for the case of Finite Element  $h$ -refinement.
- **O2** For a given level of spatial discretisation refinement and time step, to compare the thermodynamical consistency of the proposed time integrator to that of the mid-point time integrator.

The geometry for the problem is displayed in Figure 14. The L-shaped solid is subjected to an external torque induced by a pair of forces  $\mathbf{F}_1(t)$  and  $\mathbf{F}_2(t)$  acting on two of the boundary faces (refer to Figure 14), defined as

$$\mathbf{F}_2(t) = -\mathbf{F}_1(t); \quad \mathbf{F}_1(t) = \begin{bmatrix} 256/9 \\ 512/9 \\ 768/9 \end{bmatrix} f(t); \quad f(t) = \begin{cases} t & 0 \leq t < 2.5 \text{ s}, \\ 5 - t & 2.5 \text{ s} \leq t < 5 \text{ s} \\ 0 & t \geq 5 \text{ s}. \end{cases} \quad (82)$$

In addition, initial distribution of temperature on the solid is

$$\theta(\mathbf{X})|_{t=0} = \begin{cases} T_1 & Z = L_Z, \\ T_2 & X = L_X; \\ \theta_R & \text{elsewhere.} \end{cases} \quad T_1 = 300 \text{ K}; \quad T_2 = 250 \text{ K}. \quad (83)$$

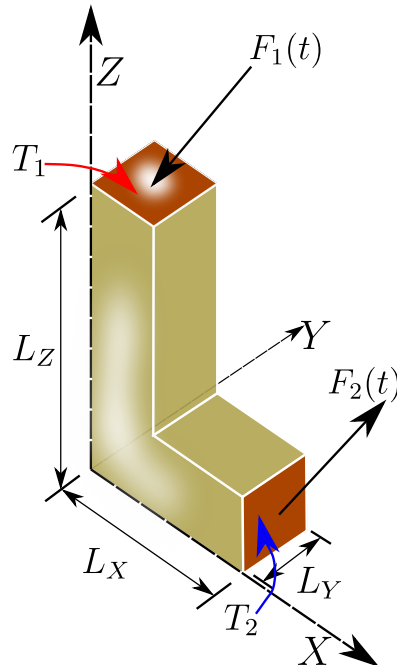


Figure 14: Numerical example 1. Geometry and general setting.

In order to establish a quantitative comparison with the results provided in Reference [14], we use in this example the constitutive model considered therein. This can be expressed in terms of the following additive decomposition,

$$\widetilde{W}(\mathbf{C}, \mathbf{G}, C, \theta) = \widetilde{W}_m(\mathbf{C}, \mathbf{G}, C) + \widetilde{W}_\theta(\theta) - (\theta - \theta_R)\widetilde{\eta}_R(C), \quad (84)$$

where each of the contributions in (84) is defined as

$$\begin{aligned} \widetilde{W}_m(\mathbf{C}, \mathbf{G}, C) &= \frac{\mu_1}{2}\text{tr}\mathbf{C} + \frac{\mu_2}{2}\text{tr}\mathbf{G} - (\mu_1 + 2\mu_2)\ln C^{1/2} + \frac{\lambda}{2}(C^{1/2} - 1)^2; \\ \widetilde{W}_\theta(\theta) &= c_v \left( \theta - \theta_R - \theta \ln \frac{\theta}{\theta_R} \right); \quad \widetilde{\eta}_R(C) = -3\beta(a(C^{1/2} - 1) - bC^{-1/2}). \end{aligned} \quad (85)$$

The thermal conductivity tensor is particularised for the case of isotropy, whereby it can be expressed in terms of the scalar conductivity field  $k$ , i.e.  $\mathbf{k} = k\mathbf{I}$ . The value of all the relevant material and geometrical parameters in this example can be found in Table 9.

Table 9: Numerical example 1. Geometrical parameters (see Figure 14) and material parameters (see (85)).

<b>Geometrical parameters</b>	$L_X$	6	m	
	$L_Y$	3	m	
	$L_Z$	10	m	
<b>Material parameters</b>	$\mu_1$	1646,7	Pa	
	$\mu_2$	332,5	Pa	
	$\lambda$	0	Pa	
	$c_v$	100	$\text{JK}^{-1}\text{m}^{-3}$	(Specific heat capacity)
	$\theta_R$	293.15	K	(Reference temperature)
	$\beta$	$2,233 \times 10^{-4}$	$\text{K}^{-1}$	
	$a$	$\mu_1 + 2\mu_2$	Pa	
	$b$	0	Pa	
	$k$	10	$\text{WK}^{-1}\text{m}^{-1}$	(Thermal conductivity)
	$\rho_0$	100	$\text{kg/m}^3$	(Material density)

Four different levels of  $h$ -refinement will be considered in this example. These can be observed in Figure 15. A course, medium, fine and ultra fine finite element meshes (denoted as **Mesh1**, **Mesh2**, **Mesh3** and **Mesh4**, respectively) have been considered. With regards to objective **O1**, we recall that the Courant-Friedrichs-Lowy number (denoted hereby as  $\alpha_{CFL}$ ) is defined as

$$\alpha_{CFL} = c_p \frac{\Delta t}{h}; \quad c_p = \sqrt{\frac{\lambda_R + 2\mu_R}{\rho_0}}, \quad (86)$$

where  $\Delta t$  denotes the time step used in the simulations and  $h$  the characteristic size of the finite element mesh, and  $c_p$  the longitudinal wave speed in the reference configuration ( $\nabla_0 \phi = \mathbf{I}$ ,  $\theta = \theta_R$ ). For hexahedral meshes, we consider  $h$  to be related to the volume of the element  $e$  in the mesh (i.e.  $V_e$ ) and to the order of the Finite Element interpolation  $q$  (i.e.  $q = 1$  for  $Q_1$  elements,  $q = 2$  for  $Q_2$  elements, etc.) as

$$h = \left( \frac{\min_e V_e}{q^3} \right)^{1/3}; \quad 1 \leq e \leq N, \quad (87)$$

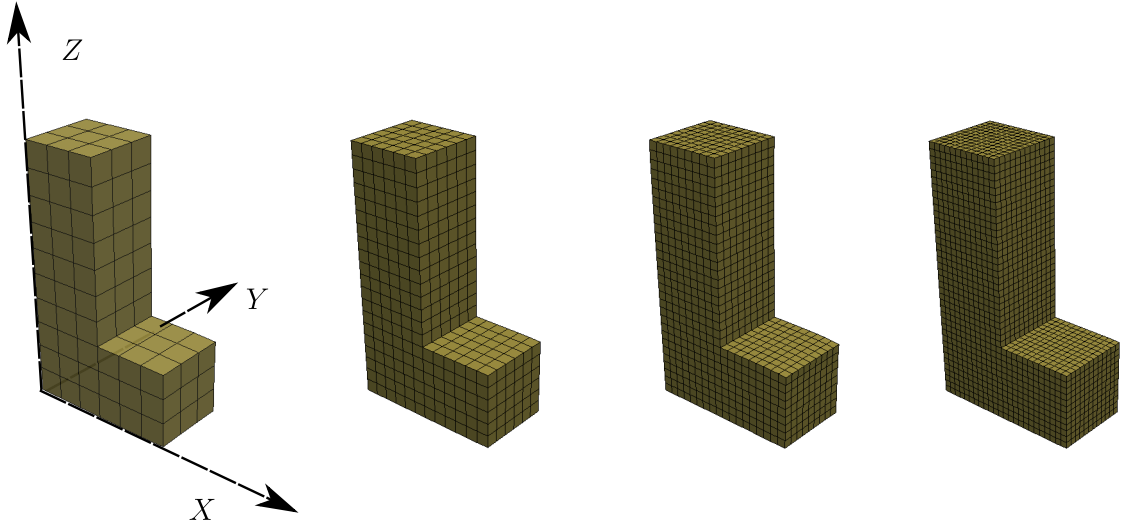


Figure 15: Numerical example 1.  $h$ -refinement used in the study.  $Q_1-Q_1$  finite element discretisation for both spatial geometry  $\phi$  and temperature  $\theta$ . From left to right: **Mesh1** (with  $\{672, 224\}$  dofs for  $\{\phi, \theta\}$ ); **Mesh2** (refinement of  $\times 2$  in every direction with respect to **Mesh1**, yielding  $\{3822, 1274\}$  dofs for  $\{\phi, \theta\}$ ); **Mesh3** (refinement of  $\times 3$  in every direction with respect to **Mesh1**, yielding  $\{12000, 4000\}$  dofs for  $\{\phi, \theta\}$ ); **Mesh4** (refinement of  $\times 4$  in every direction with respect to **Mesh1**, yielding  $\{25350, 8450\}$  dofs for  $\{\phi, \theta\}$ ).

where  $N$  denotes the number of elements for the underlying discretisation. Figure 16<sub>a</sub> shows the final time instant  $T_{final}$  for which the proposed EM time integrator fails, that is, [the time step for which the convergence of the iterative Newton-Raphson algorithm is not achieved \[19, 20\]](#), for different values of the  $\alpha_{CFL}$  number and for the four levels of  $h$ -refinement displayed in Figure 15. Clearly, for large values of the  $\alpha_{CFL}$  number, the new EM time integrator becomes unstable at smaller values of  $T_{final}$ , as expected.

Figure 16<sub>b</sub> sheds light with regards to the relative stability of the proposed EM time integrator with respect to that of the classical mid-point time integrator. Specifically, this figure shows the difference between the final time instant for which the proposed EM time integrator and the mid-point rule become unstable. This has been denoted in that figure as  $\Delta T_{final}$ . [Contrary to the EM time integrator, for the mid-point integrator, the lack of convergence of the Newton-Raphson is always preceded by an uncontrollable growth of the Hamiltonian over the previous time steps.](#) Positive values of  $\Delta T_{final}$  imply that the proposed time integrator becomes unstable at later time instants, and viceversa. It is worth noticing that beyond  $\alpha_{CFL} \geq 5 - 10$ ,  $\Delta T_{final}$  adopts negative values. This indicates that the size of the time step  $\Delta t$  cannot be chosen arbitrarily large, expecting an improved robustness and stability of the EM time integrator with respect to the classical mid-point rule. In fact our numerical study suggests that  $\Delta t$  must be chosen such that  $\alpha_{CFL} \leq 5$  in order to guarantee a higher stability and robustness in the long term.

With regards to objective **O2**, we use in this study the computational domain defined by **Mesh2** (see Figure 15) and a value of  $\alpha_{CFL}$  of  $\alpha_{CFL} = 2.2955$ . It can be seen that for both the new EM time integrator and the mid-point rule the angular momentum  $\mathbf{J}$  remains constant beyond  $t \geq 5$  s, when the external applied pair of forces vanishes. In addition, the linear momentum  $\mathbf{L}$  is zero for the entire simulation. Another interesting variable of interest is the global entropy ( $\tilde{\eta} = \int_{\mathcal{B}_0} \eta dV$ ), which increases over time for the entire simulation for both time integrators. Furthermore, the Hamiltonian  $\mathcal{H}$  is displayed. The zoomed detail perfectly shows the sudden increase in the Hamiltonian  $\mathcal{H}$  prior to the instability when using the mid-point rule. The increase of the Hamiltonian  $\Delta\mathcal{H} = \mathcal{H}_{n+1} - \mathcal{H}_n$  (normalised with respect to the maximum historic value of  $\mathcal{H}$  in absolute value) is also displayed. It can be seen that the new EM time integrator preserves  $\mathcal{H}$  (beyond  $t \geq 5$  s) as it has been designed specifically with that purpose, whereas the mid-point rule does not.

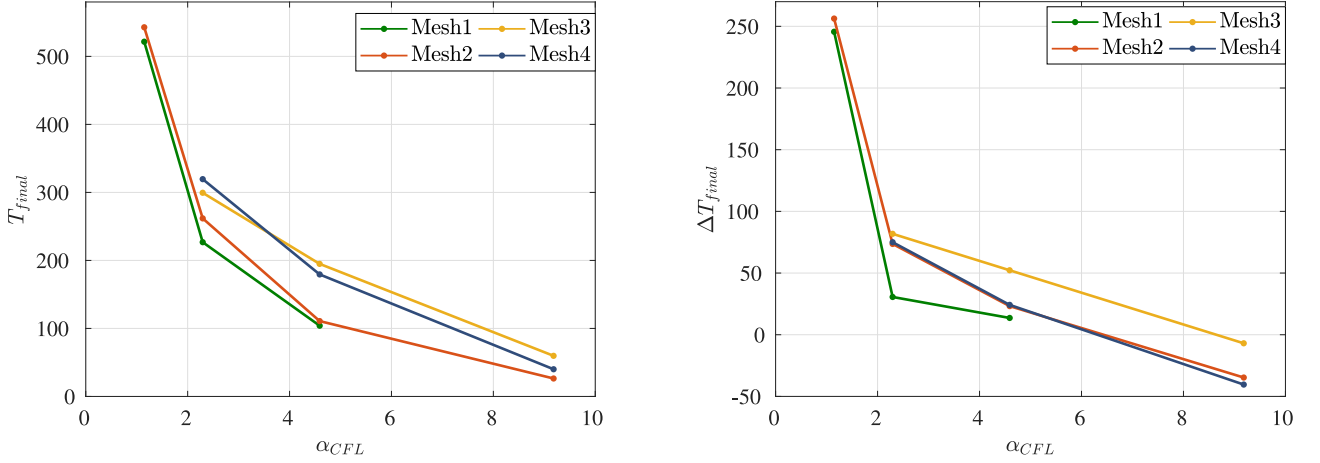


Figure 16: Numerical example 1. Left: final time instant ( $T_{final}$ ) for which the EM time integrator becomes unstable. Right: Difference between the final time instant ( $\Delta T_{final}$ ) at which the EM time integrator and the mid-point rule become unstable. Results shown for various values of  $\alpha_{CFL}$  and for the discretisations in Figure 15.

Finally, the temperature contour plot is displayed over time in Figure 18. The results have been obtained by means of the new EM time integrator using a different mesh from the four depicted in Figure 15. This mesh has been generated refining by a factor of  $\times 6$  in the three directions the computational domain defined by **Mesh1**.

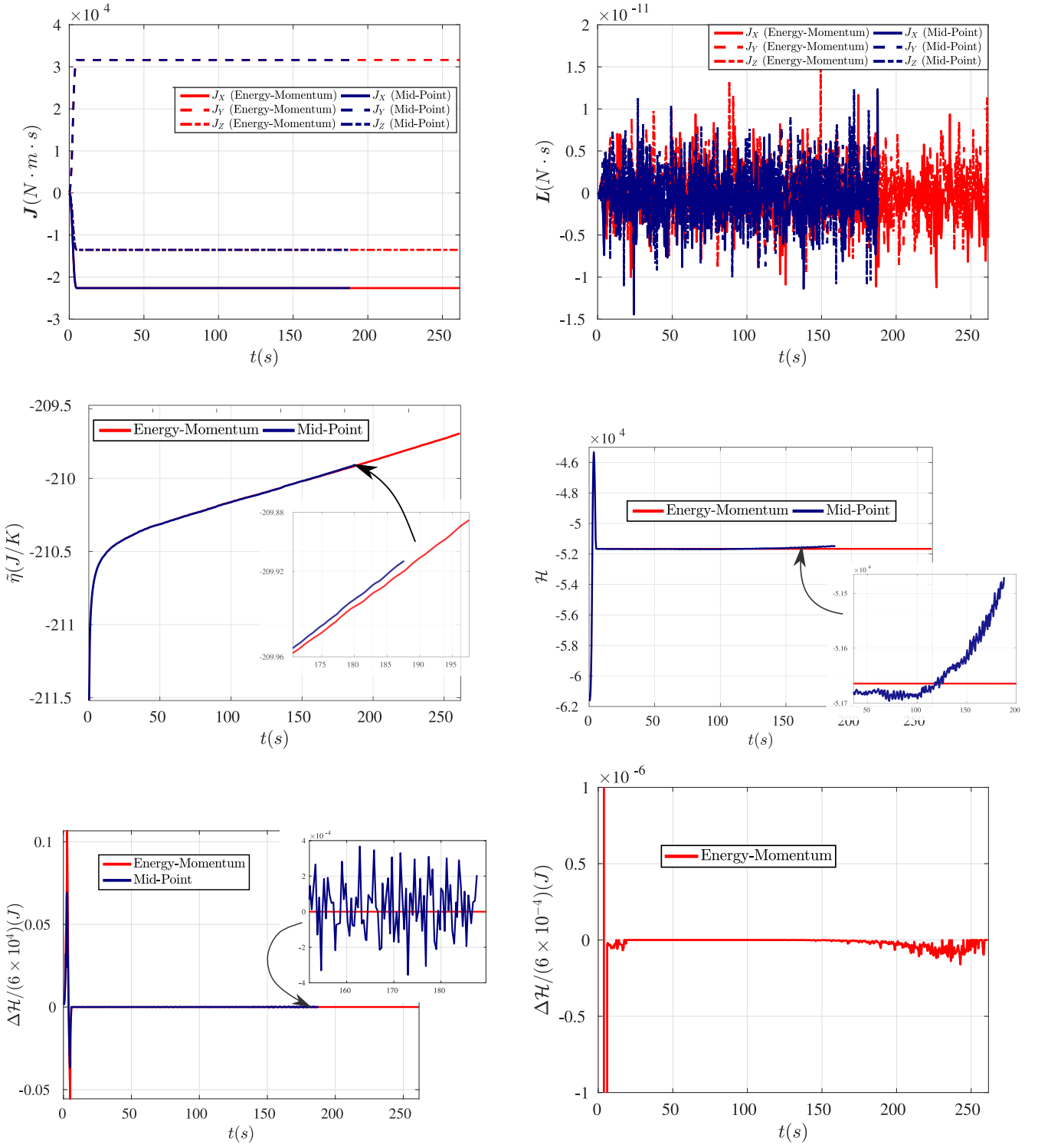


Figure 17: Numerical example 1. Evolution of: (a) angular momentum  $\mathbf{J}$ , (b) linear momentum  $\mathbf{L}$ , (c) global entropy  $\tilde{\eta} = \int_{\mathcal{B}_0} \eta dV$ , (d) Hamiltonian  $\mathcal{H}$  in (??), (e) increment of Hamiltonian  $\Delta\mathcal{H}$  for both the Mid-Point and the new EM time integrator. Finally, (f), zoomed detail of the increment of the Hamiltonian  $\Delta\mathcal{H}$  for the new EM time integrator. Results obtained for **Mesh2** with  $\alpha_{CFL} = 2.2955$  ( $\Delta t = 0.2$  s).

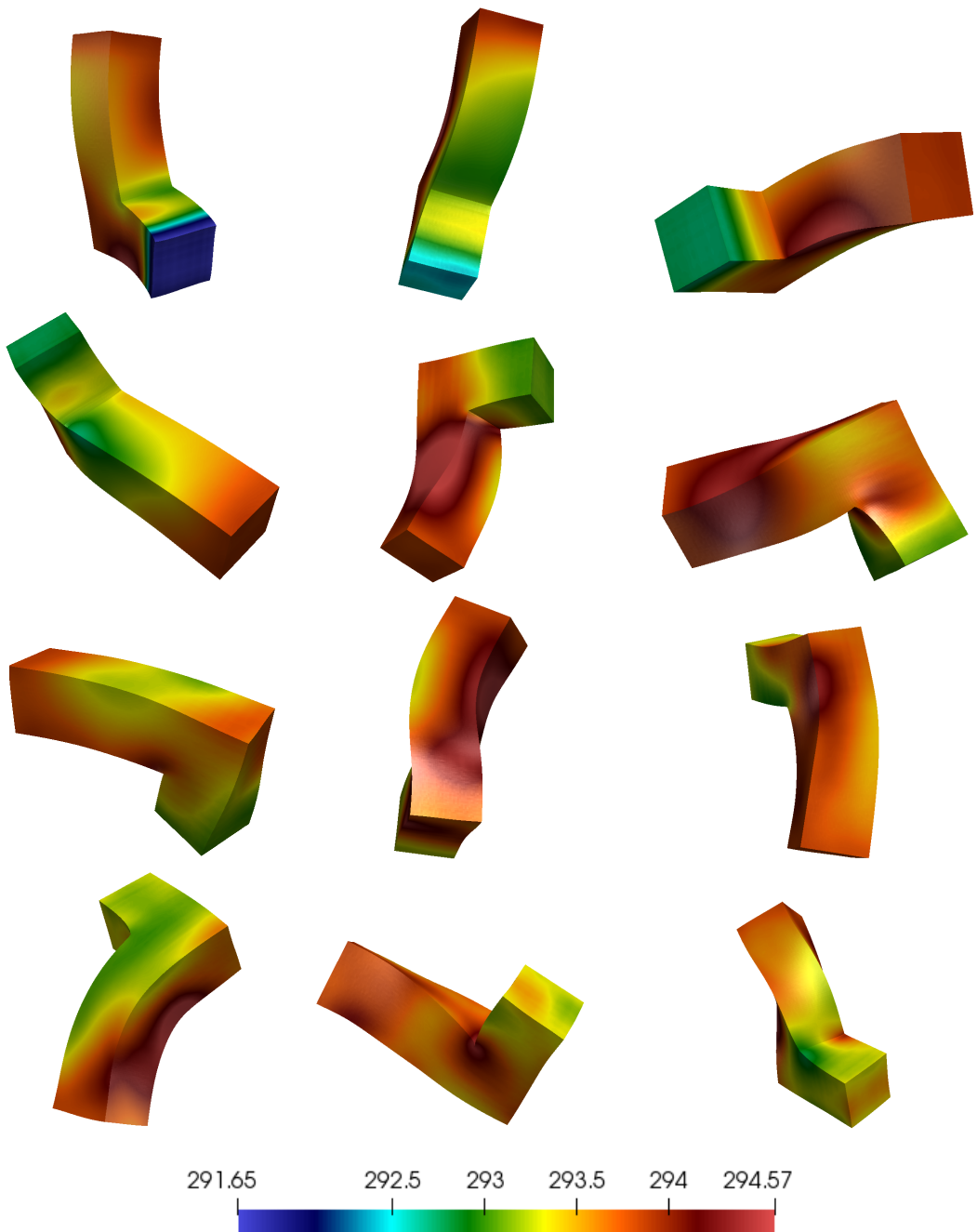


Figure 18: Numerical example 1. Contour plot distribution of absolute temperature  $T(K)$  for  $t = \{2.5, 5, 8, 11, 15, 19, 21, 25, 33, 35, 40, 43\}$  s (from left to right and top to bottom).  $Q_1-Q_1$  discretisation for both spatial geometry  $\phi$  and temperature  $\theta$ . Number of dofs in the mesh:  $\{85557, 28519\}$  for  $\{\phi, \theta\}$ . Results obtained by means of the new EM time integrator for  $\alpha_{CFL} = 3.44$  ( $\Delta t = 0.1$  s).

## 6.5. Numerical Example 2

The objective of this example is

- **O1** Study the stability and robustness in a problem where the deformation is exclusively induced by thermal effects.

The geometry for this example is displayed in Figure 19. The object in Figure 19 is subjected to a heat flux at the bottom surface (minimum coordinate  $Z$ ), characterised by the following mathematical expression

$$Q_\theta(t) = Q_{\max} \sin \frac{2\pi}{T} t; \quad T = 1 \text{ s}; \quad Q_{\max} = 3000 \text{ W/m}^2. \quad (88)$$

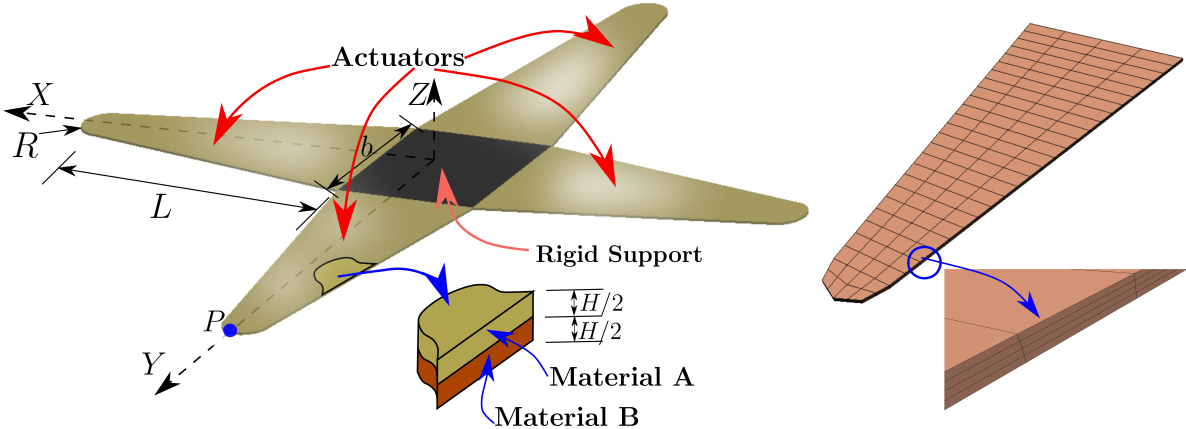


Figure 19: Numerical example 2. Left: geometry and general setting for the bi-material thermo-mechanical actuator. Right: computational domain considered for the analysis of **O1**, based on a  $Q_2$  discretisation for  $\{\mathbf{x}, T\}$ , ( $\{1215, 405\}$  dofs). Every  $Q_2$  finite element has been divided into  $2 \times 2 \times 2$  elements for visualisation purposes.

The constitutive model used in this example is that presented in Section ?? through equations (33), (??), (??) and (??). The value of the material parameters in that model can be found in Table 10.

With regards to objective **O1**, we use in this study the computational domain defined in Figure 19 and several values of  $\alpha_{CFL}$ . From Figure 20<sub>(a)-(b)</sub> it can be observed that the range of stability of the new EM time integrator is larger than that of the mid-point rule for approximately  $\alpha_{CFL} \leq 10$  (close to zero and even negative values of  $\Delta T_{final}$  are obtained in the range  $\alpha_{CFL} \geq 10$ ). For a fixed value of  $\alpha_{CFL} = 5.6$  ( $\Delta t = 4 \times 10^{-4}$  s), Figure 20<sub>(c)</sub> shows the evolution of the Hamiltonian in equation (??) for both the new EM time integrator and the mid-point rule. In this case, the non-vanishing heat flux  $Q_\theta$  (88) prevents the Hamiltonian from being preserved. Nonetheless, from equations (??), (??) and (??), it is clear that the quantity of interest defined as

$$\tilde{\mathcal{H}} = \mathcal{H} - \Pi_{\text{ext}} - \mathcal{Q}_{\text{ext}} \quad (89)$$

must be preserved by the new EM time integrator. This is in fact confirmed in Figure 20<sub>(d)</sub>, where  $\tilde{\mathcal{H}}$  is perfectly preserved throughout the entire simulation by the new proposed time integrator. On the contrary,  $\tilde{\mathcal{H}}$  increases over time when using the mid-point time integrator until it finally becomes unstable. Finally, Figure 22 shows the pressure contour plot over various snapshots computed by means of the new EM time integrator using the computational domain defined in Figure 21.

Table 10: Numerical example 2. Geometrical parameters (see Figure 19) and material parameters (see (85)).

<b>Geometrical parameters</b>	$L$	0,12	m	
	$b$	0,06	m	
	$H$	0,001	m	
	$R$	0,01	m	
<b>Material parameters A</b>	$\mu_1$	41.67	kPa	
	$\mu_2^A$	0	Pa	
	$\lambda^A$	27.78	Pa	
	$c_v^A$	2000	$\text{JK}^{-1}\text{m}^{-3}$	(Specific heat capacity)
	$\theta_R^A$	293,15	K	(Reference temperature)
	$\Gamma_0^A$	0		
	$q^A$	1		
	$k^A$	10	$\text{WK}^{-1}\text{m}^{-1}$	(Thermal conductivity)
	$\rho_0^A$	1000	$\text{kg}/\text{m}^3$	(Material density)
<b>Material parameters B</b>	$\mu_1^B$	250	kPa	
	$\mu_2^B$	0	Pa	
	$\lambda^B$	166	Pa	
	$c_v^B$	2000	$\text{JK}^{-1}\text{m}^{-3}$	(Specific heat capacity)
	$\theta_R^B$	293,15	K	(Reference temperature)
	$\Gamma_0^B$	0.01		
	$q^B$	1		
	$k^B$	10	$\text{WK}^{-1}\text{m}^{-1}$	(Thermal conductivity)
	$\rho_0^B$	1000	$\text{kg}/\text{m}^3$	(Material density)

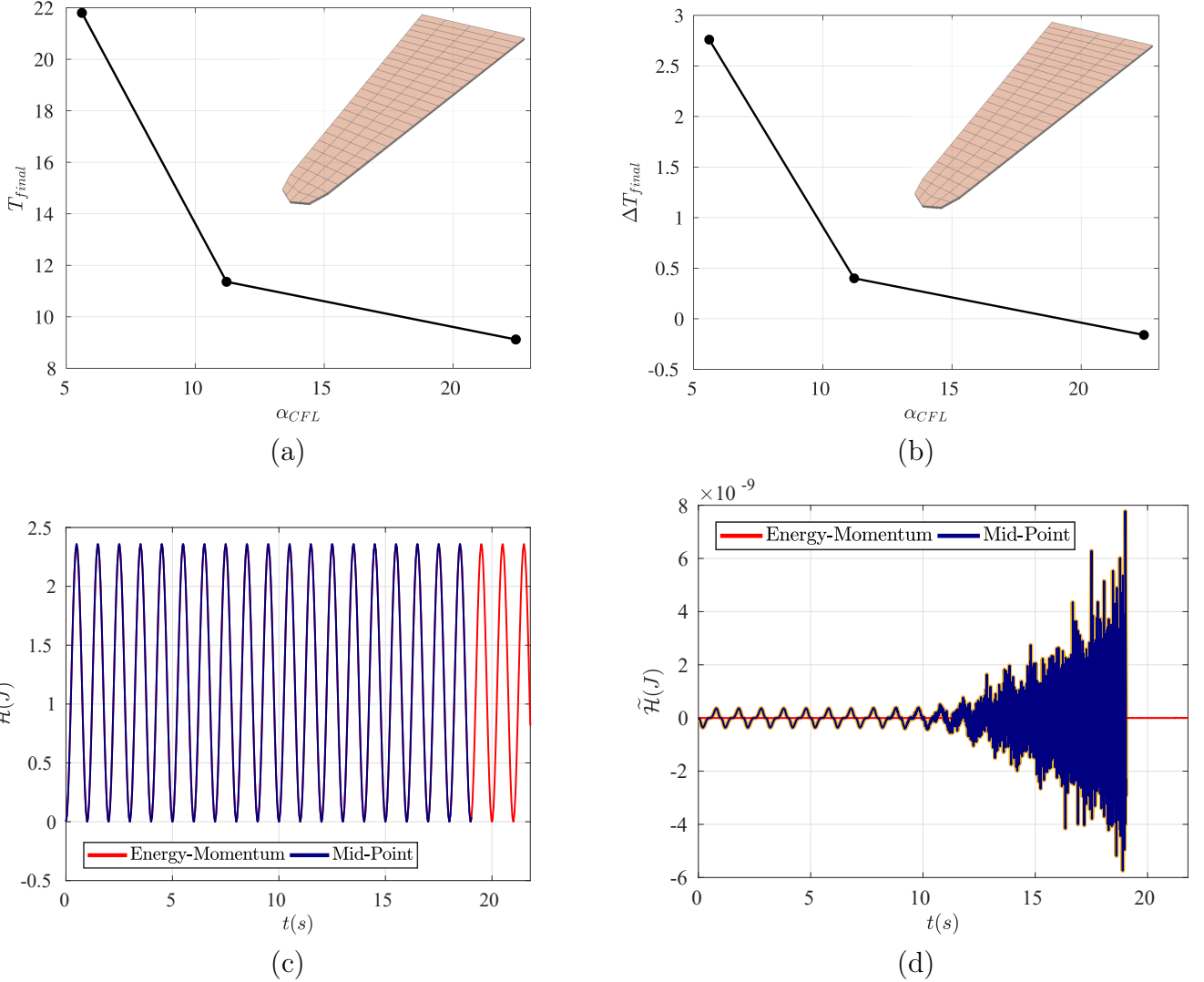


Figure 20: Numerical example 2. (a) Final time instant ( $T_{final}$ ) for which the EM time integrator becomes unstable. (b) Difference between the final time instant ( $\Delta T_{final}$ ) at which the EM time integrator and the mid-point rule become unstable. Results shown for various values of  $\alpha_{CFL} = \{5.6, 11.21, 22.42\}$  ( $\Delta t = \{4, 8, 16\} \times 10^{-4}$  s) and for the computational domain displayed. (c) Evolution of the Hamiltonian  $\mathcal{H}$  (??) when using the mid-point rule and the new EM time integrator for  $\alpha_{CFL} = 5.6$ . (d) Evolution of the quantity of interest  $\tilde{\mathcal{H}}$  in (89) for both mid-point rule and the new EM time integrator for  $\alpha_{CFL} = 5.6$ .

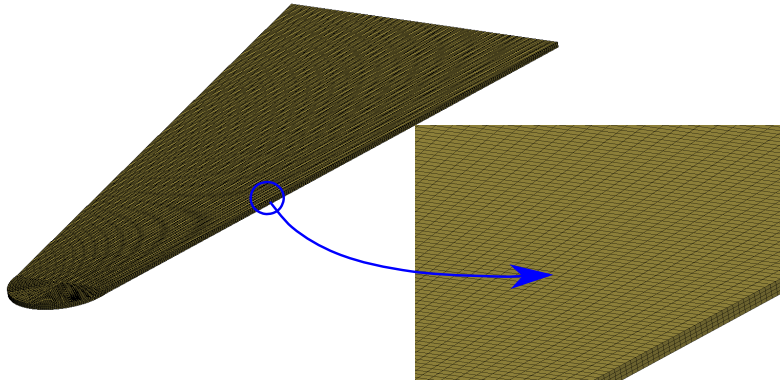


Figure 21: Numerical example 2. Computational domain discretised with  $Q_2$  elements for both geometry  $\phi$  and temperature  $\theta$ . Discretisation of  $\{164430, 54810\}$  dofs for  $\{\phi, \theta\}$ . In the figure every  $Q_2$  finite element has been divided into  $2 \times 2 \times 2$  elements for visualisation purposes.

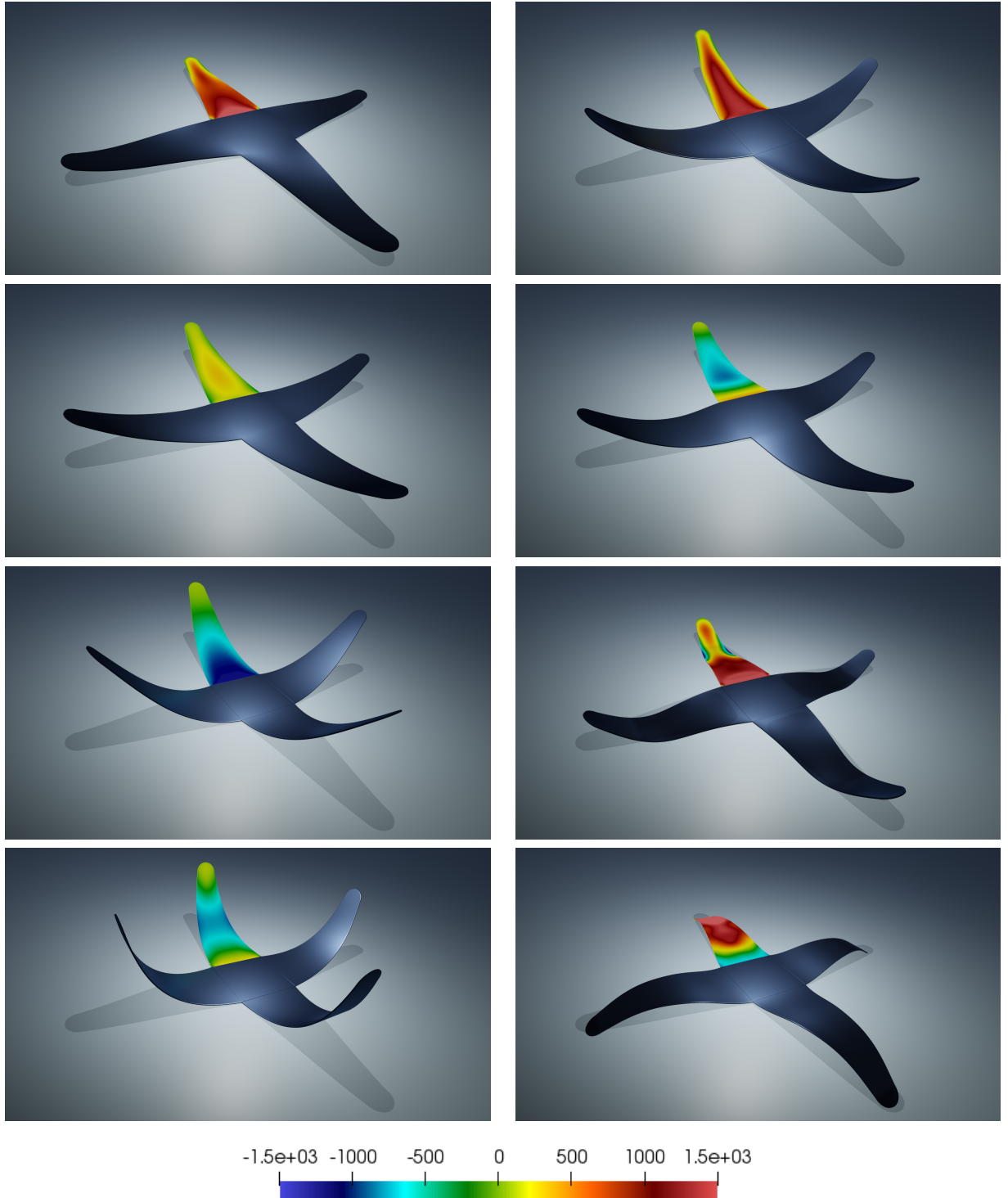


Figure 22: Numerical example 2. Rendering of deformed configuration and contour plot distribution of hydrostatic pressure  $p$  for snapshots corresponding to:  $t = \{0.41, 1.01, 1.81, 2.61, 3.41, 3.81, 4.41, 5.01\}$  s (from top to bottom and left to right). Results obtained with new EM time integrator and with  $\alpha_{CFL} = 6.4$  ( $\Delta t = 10^{-4}$  s). Computational domain in Figure 21.

### 6.6. Numerical Example 3

The objective of this example is

- **O1** Confirmation of the results provided in the previous examples, in terms of stability and robustness, in a challenging numerical example.

The geometry for this example is displayed in Figure 23. The squared object in Figure 23 is subjected to an initial velocity profile given by the following equation

$$\mathbf{v}|_{t=0} = \sqrt{\frac{2}{\pi}} \left( \exp\left(-\frac{(X-5)^2}{10}\right) + \exp\left(-\frac{(Y-5)^2}{10}\right) \right) \begin{bmatrix} 0 \\ 0 \\ 1 \end{bmatrix} \text{ (m/s).} \quad (90)$$

In addition, the object in Figure (23) is initially subjected to a uniform temperature distribution of  $\theta|_{t=0} = \theta_R$ , and a heat flux  $Q_\theta$  defined as

$$Q_\theta(t) = \begin{cases} \frac{10^4}{4\pi R^2} \text{ (W/m}^2\text{)} & 0 \leq t < 2 \text{ s,} \\ 0 & t \geq 2 \text{ s.} \end{cases} \quad (91)$$

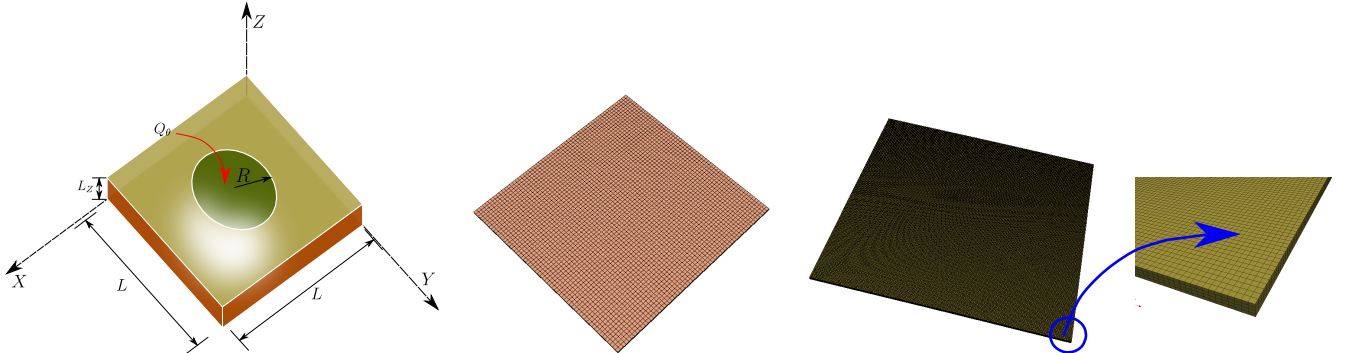


Figure 23: Numerical example 3. Left: geometry with  $\{L, L_Z, R\} = \{10, 0.1, 1.5\}$  (m). Centre: computational domain considered for the analysis of **O1**, based on a  $Q_2$  discretisation for  $\{\phi, \theta\}$ . Symmetric boundary conditions have been applied, hence only a quarter of the domain displayed has been simulated, yielding  $\{1215, 405\}$  dofs. Right: Computational domain considered for simulations in Figures 25-28, discretised with  $Q_2$  elements for both geometry  $\phi$  and temperature  $\theta$ . Symmetric boundary conditions have been applied, hence only a quarter of the domain displayed has been simulated, yielding  $\{219615, 73205\}$  dofs for  $\{\phi, \theta\}$ . In the figure every  $Q_2$  finite element has been divided into  $2 \times 2 \times 2$  elements for visualisation purposes.

The constitutive model used in this example is that presented in Section ?? through equations (33), (??), (??) and (??). The value of the material parameters in that model can be found in Table 11.

With regards to objective **O1**, we use in this study the computational domain defined in Figure 23<sub>b</sub> and a value of  $\alpha_{CFL}$  of  $\alpha_{CFL} = 1.72$  ( $\Delta t = 0.02$  s). From Figure 24, it can be seen the variation of angular momentum  $\Delta \mathbf{J}$ , linear momentum  $\Delta \mathbf{L}$ , global entropy ( $\tilde{\eta}$ ) and Hamiltonian  $\mathcal{H}$ , for both the new EM time integrator and the mid-point rule. Furthermore, the Hamiltonian  $\mathcal{H}$  is displayed. The zoomed detail perfectly shows the sudden increase in the Hamiltonian  $\mathcal{H}$  prior to the instability when using the mid-point rule. The increase of the Hamiltonian  $\Delta \mathcal{H} = \mathcal{H}_{n+1} - \mathcal{H}_n$  is also displayed. It can be seen that the new EM time integrator preserves  $\mathcal{H}$  (beyond  $t \geq 2$  s), whereas the mid-point rule does not. It is interesting to observe that since only a quarter of the domain has been simulated, the introduction of symmetric boundary conditions introduces a reaction force which prevents the global linear and angular momentum ( $\mathbf{L}$  and  $\mathbf{J}$ ) to be preserved. Only the  $Z$  component of  $\mathbf{L}$  and  $\mathbf{J}$  is preserved throughout the

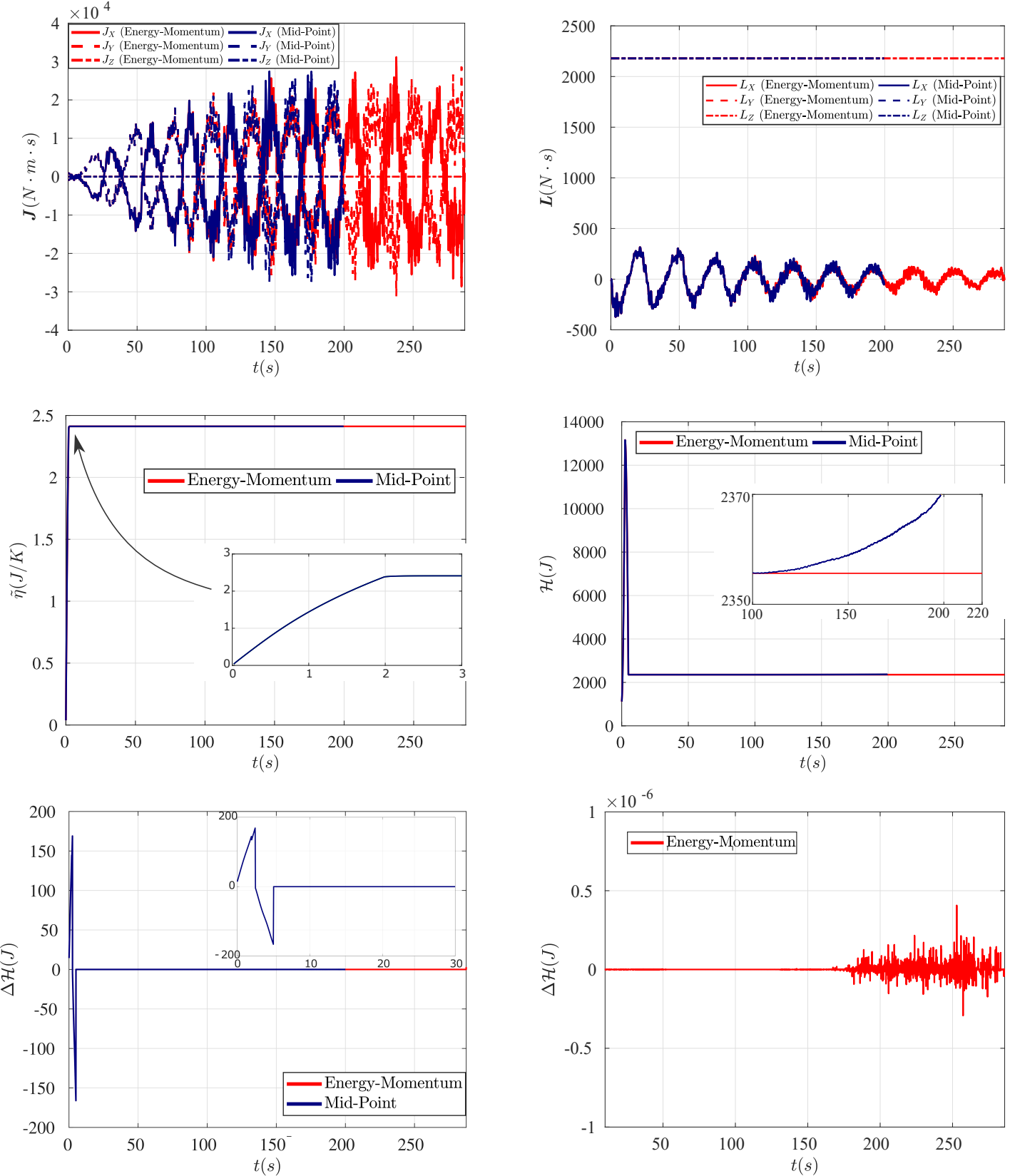


Figure 24: Numerical example 3. Evolution of: (a) angular momentum  $\mathbf{J}$ , (b) linear momentum  $\mathbf{L}$ , (c) global entropy  $\tilde{\eta} = \int_{B_0} \eta dV$ , (d) Hamiltonian  $\mathcal{H}$  in (??), (e) increment of Hamiltonian  $\Delta\mathcal{H}$  for both the Mid-Point and the new EM time integrator. Finally, (f), zoomed detail of the increment of the Hamiltonian  $\Delta\mathcal{H}$  for the new EM time integrator. Results obtained for mesh in Figure 23 with  $\alpha_{CFL} = 1.72$  ( $\Delta t = 0.02$  s).

Table 11: Numerical example 3. Geometrical parameters (see Figure 23) and material parameters (see (85)).

<b>Geometrical parameters</b>	$L$	10	m
	$L_Z$	0.1	m
	$R$	1.5	m
<b>Material parameters</b>	$\mu_1$	19,42	kPa
	$\mu_2$	0	Pa
	$\lambda$	29,13	Pa
	$c_v$	1	$\text{JK}^{-1}\text{m}^{-3}$ ( <i>Specific heat capacity</i> )
	$\theta_R$	308,15	K ( <i>Reference temperature</i> )
	$\Gamma_0$	$6,7 \times 10^{-4}$	
	$q$	1	
	$k$	10	$\text{WK}^{-1}\text{m}^{-1}$ ( <i>Thermal conductivity</i> )
	$\rho_0$	1000	$\text{kg}/\text{m}^3$ ( <i>Material density</i> )

simulation (for both time integrators), as the symmetric boundary conditions only affect the  $X$  and  $Y$  directions.

Finally, we consider the computational domain defined in Figure 23<sub>c</sub>. Figure 25 displays the pressure contour plot distribution for various time snapshots. Furthermore, Figure 26 shows the wrinkling pattern that forms over the surface of the plate over time. The wrinkles can be better appreciated in Figure 27. Finally, Figure 28 shows the evolution of the  $Z$  components of the displacement of the centroid of the plate over time, induced by the initial velocity profile in (90).

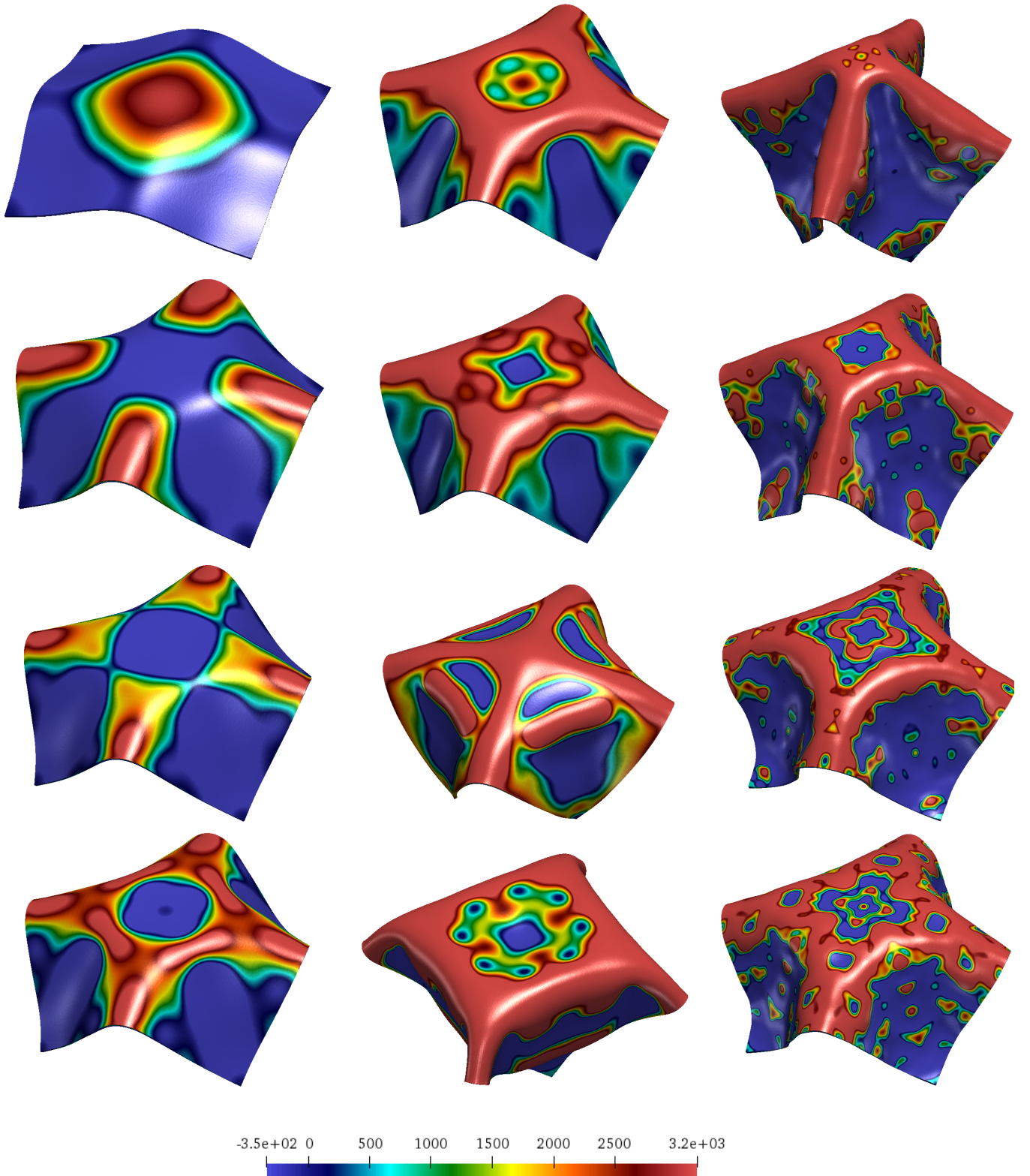


Figure 25: Numerical example 3. Contour plot of hydrostatic pressure  $p = \frac{1}{3J} \mathbf{S} : \mathbf{C}$  at time steps  $t = \{1.98, 3.58, 3.98, 4.18, 4.38, 4.98, 5.98, 9.36, 23.62, 26.60, 28.52, 29.28\}$  s (from left to right and top to bottom). Results of obtained by means of the new EM time integrator for  $\alpha_{CFL} = 4.7$  ( $\Delta t = 0.02$  s). Computational domain in Figure 23c. The results do not show the vertical (Z direction) elevation of the plate (refer to Figure 28).

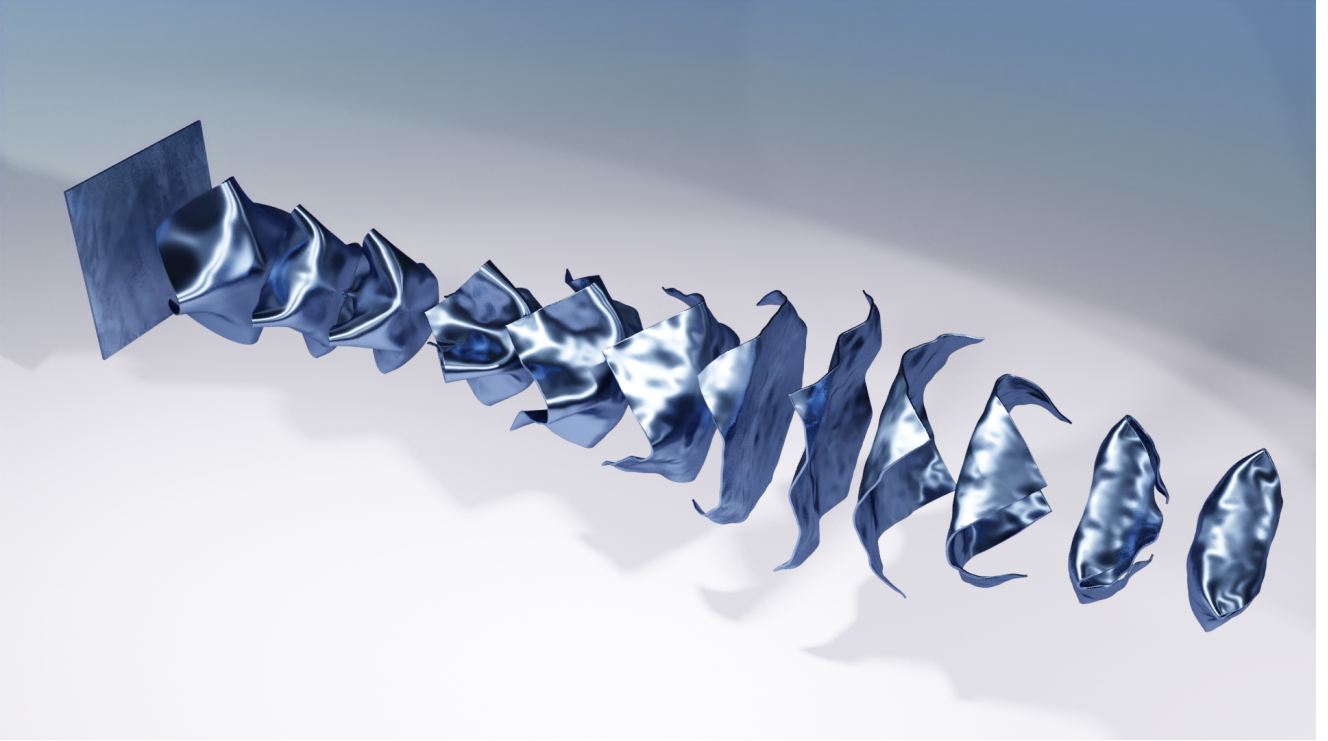


Figure 26: Numerical example 3. Rendering of results for deformed configuration at various time steps (from top to bottom and from left to right). Results obtained by means of the new EM time integrator for  $\alpha_{CFL} = 4.7$  ( $\Delta t = 0.02$  s). Computational domain in Figure 23<sub>c</sub>.

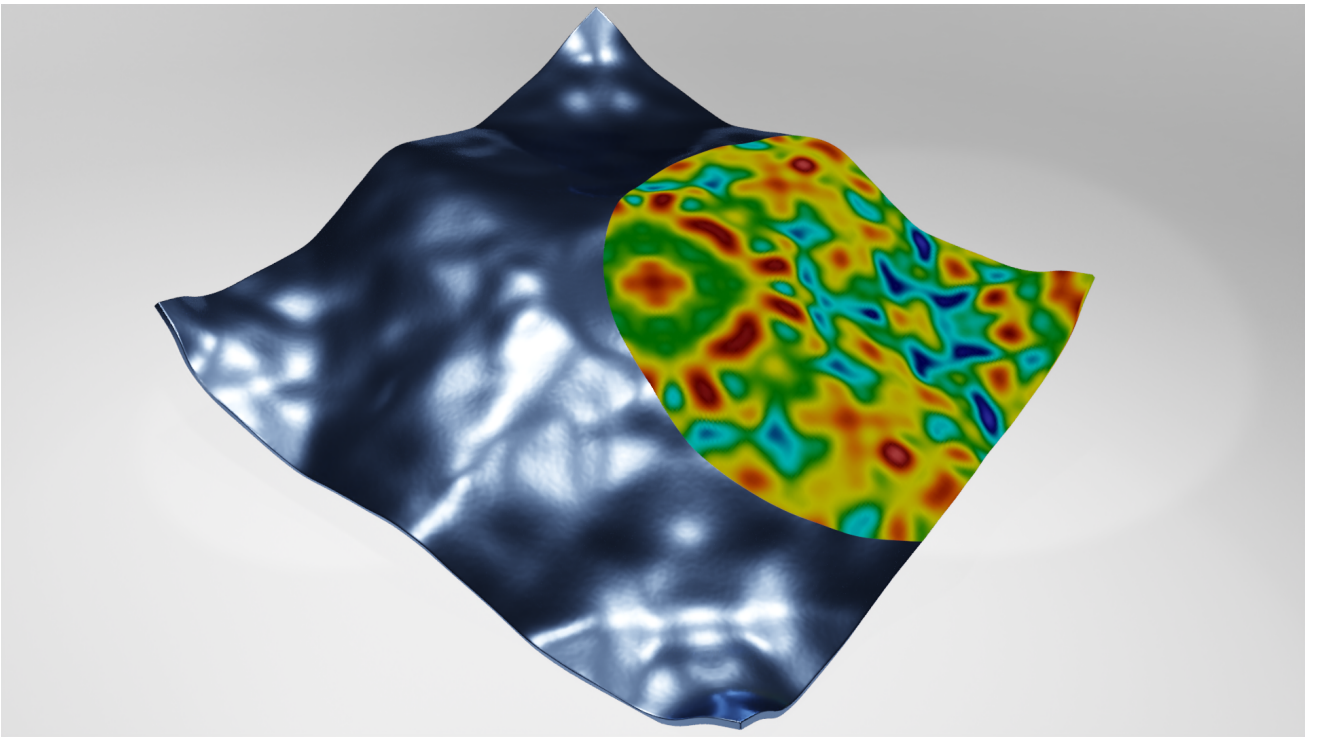


Figure 27: Numerical example 3. Rendering of wrinkling pattern over the surface of the thin plate at time  $t = 23.62$  s. Results obtained with the new EM time integrator for  $\alpha_{CFL} = 4.7$  ( $\Delta t = 0.02$  s). Computational domain in Figure 23<sub>c</sub>.

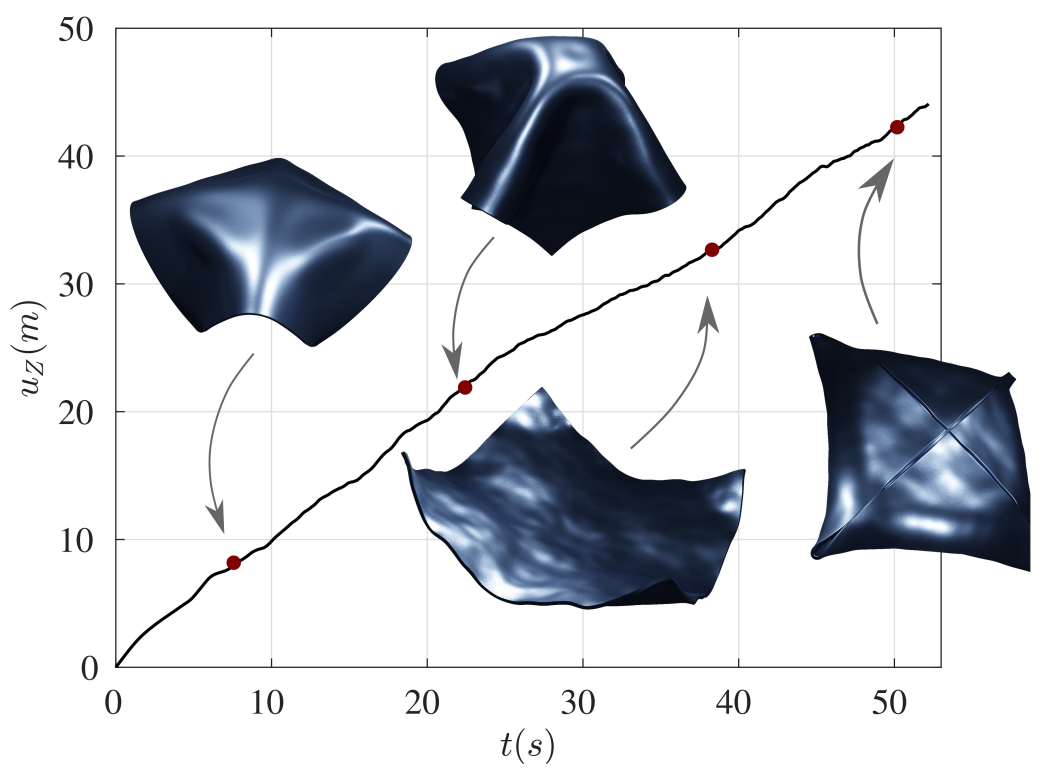


Figure 28: Numerical example 3. Evolution of the displacement in  $Z$  direction of the centroid of the thin plate in Figure 23 with respect to time ( $t$ ). Deformed configuration at selected snapshots.

## 7. Conclusions

A new one-step implicit and thermodynamically consistent Energy-Momentum (EM) preserving time integration scheme has been presented for the simulation of structural components undergoing large deformations and temperature fields, for which well-posed constitutive models are used for the entire range of deformations and temperature. The use of polyconvexity inspired constitutive models and the new tensor cross product algebra pioneered by de Boer [12] and re-discovered by Bonet et al. [9] in the context of nonlinear solid mechanics, are key for the development of the discrete derivatives, fundamental for the construction of the EM algorithmic derived variables, namely the second Piola-Kirchoff stress tensor and the entropy (or the absolute temperature). The proposed scheme inherits the advantages of the EM scheme recently published by Franke et al. [14] (i.e. consistency, stability, conservation) whilst resulting in dramatically far simpler algorithmic expressions, thus circumventing a bottleneck and paving the way for the incorporation of further physics into the model. A series of numerical examples have been presented in order to demonstrate the robustness and applicability of the new EM scheme. These examples make use of a temperature-based version of the EM scheme (using the Hemlholtz's free energy as the thermodynamical potential and the temperature as the thermodynamical state variable). Appendix A includes an entropy-based analogue EM scheme (using the internal energy as the thermodynamical potential and the entropy as the thermodynamical state variable).

## 8. Neural Network postprocessing

The objective of this section is to establish the quantitative relationship between different neural network hyperparameters; namely: the number of nodes ( $n_{nodes}$ ), the number of neurons ( $n_{neurons}$ ), the number of experiments ( $n_{experiments}$ ) and the number of layers ( $n_{layers}$ ), and how they affect the neural network predictive performance.

In order to study how these hyperparameters impact the performance of the machine learning model, we have decided to establish two finite element models that will act as ground-truth to compare against. First, a simple dielectric elastomer with 4 electrodes is analysed, followed by a complex 20 electrode FE model.

To measure the accuracy of the prediction made by the neural network, the R2 metric is used.

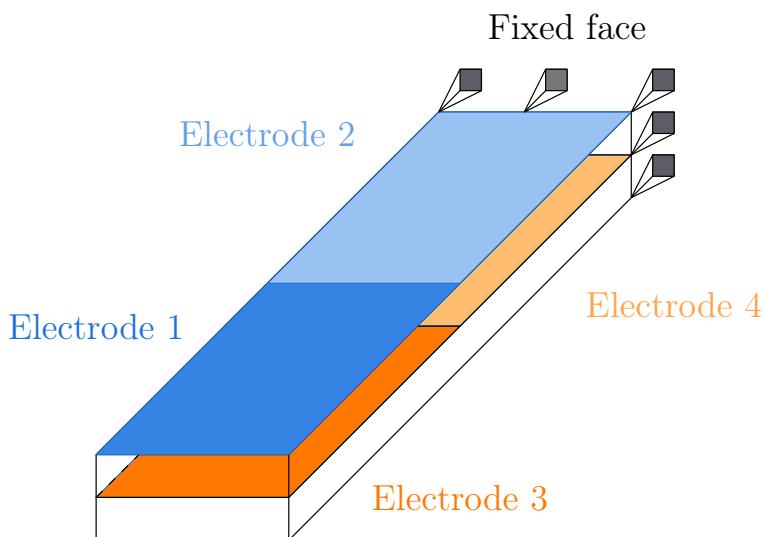
$$R^2 = 1 - \frac{\sum(y - y')^2}{\sum(y - \hat{y})^2} \quad (92)$$

Where  $y$  is the original data coming from an FE analysis,  $y'$  is the predicted data from the neural network and  $\hat{y}$  is the mean value of the FE data.

### 8.1. First test case: 4-electrode dielectric elastomer

#### 8.1.1. Data generation

The first ground-truth finite element example is a dielectric elastomer with 4 electrodes embedded: 2 electrodes at the top and 2 electrodes at the middle layer:



Different combinations of potential in each electrode will cause a unique deformation shape. For example, when the potential in electrode 1 and 2 are equal and the potential in electrode 3 and 4 are 0, a bending will be induced in the dielectric. More exotic combinations of potentials will induce a combination of bending and torsion, which can cause severe displacements, depending on the overall thickness of the dielectric and magnitude of the potentials.

To study these types of varying deformations, a Design of Experiments (DoE) will be employed using a Latin Hypercube Sampling algorithm. The main idea behind this is that each of the electrodes can have a varying potential between 0 and 0.3 V. With a fixed potential in each of the electrodes,  $n$  number of sampling points will be created by varying the potential in the rest of the electrodes. A finite number of combinations ( $n \times n_{variables} \times 2$ ) will be created, so that no electrode has the same potential using the Latin Hypercube algorithm. This effect can be visualized using 2 variables in a 3D cube, as seen in Figure 29

By using  $n$  number of design variables, this concept expands to an  $n$ -dimensional hypercube. This allows us to explore a broader design space, making sure that every point data is meaningful,

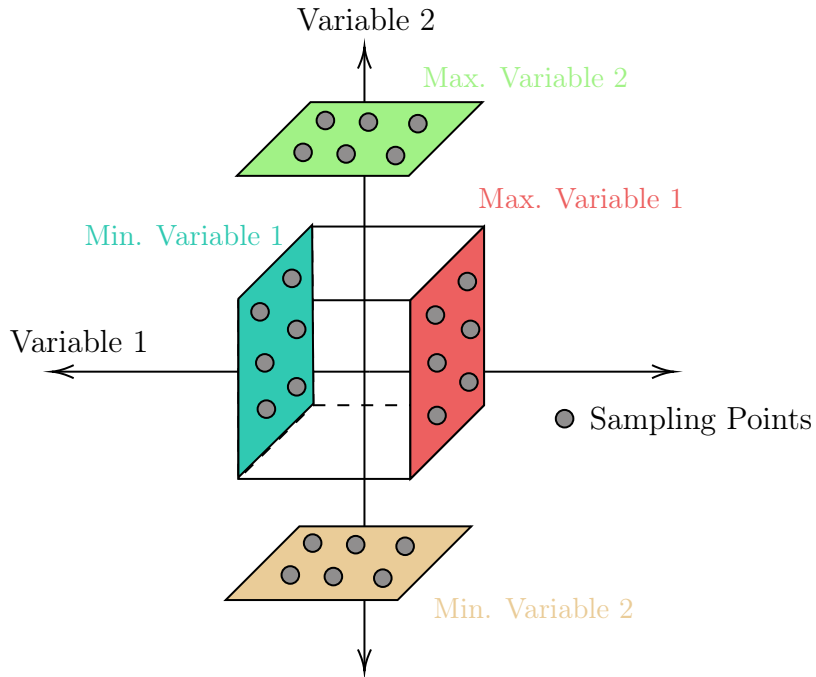


Figure 29: Data sampling strategy following a Latin Hypercube approach. The minimum and maximum value for each variable is fixed and  $n$  data points are chosen, which creates  $n_{variables} \times n_{points} \times 2$  experiments

as it represents a unique combination of potentials. In this paper, we utilized 25 sampling points, ie: there are 25 data points in each of the faces of the cube, creating  $4 \times 25 \times 2 = 200$  different combinations of potentials.

These potentials will be used as an input for the finite element analysis, in the form of a 4-element vector (the potential at each electrode). Moreover, since 200 experiments will likely be unsufficient to capture the complex phenomena behind this dielectric elastomer using a machine learning model, we will enrich this data further. To do so, we will take advantage of the load-stepping scheme implemented in the finite element analysis. Load-stepping allows for an easier convergence of the Newton-Raphson algorithm. By applying a fraction of the total load at the beginning of the analysis, solving the Newton-Raphson and then increasing the load, we can better capture non-linearities, increasing convergence.

Utilizing these intermediate data, we can extend the initial 200 finite element samples, to over 20000, accounting for possible cutbacks and bisections during the load-stepping, which will further increase the data available. For each load (combination of potentials), we also needed to store the displacement output. For ease of access and convenience, we projected the displacement of all the nodes to one of the top surfaces of the dielectric elastomer, which contains 133 nodes. Hence, for each 4-element vector load, we will have a corresponding 399-element vector of displacement (coordinates 1, 2 and 3 of each of the 133 points). These will be our training and test samples.

### 8.1.2. Training strategy

The goal now is to train a neural network to accurately predict the displacement of the dielectric elastomer for a given input potential. Hence, the input for the neural network is a 4-element vector and the output is a 399-element vector. However, since the primary deformation mechanisms will be bending and torsion, the effect of shear deformation is negligible. This allows us to effectively remove one of the components of the displacements, namely the one that represents the movement in axial direction. As a result, the original 399-element data is reduced to 266-element data, which holds only displacements in the first and third coordinate directions.

Using this data, we can train a neural network that predicts the displacement for a given combination of potentials. However, the proper architecture to do this prediction is unknown at this

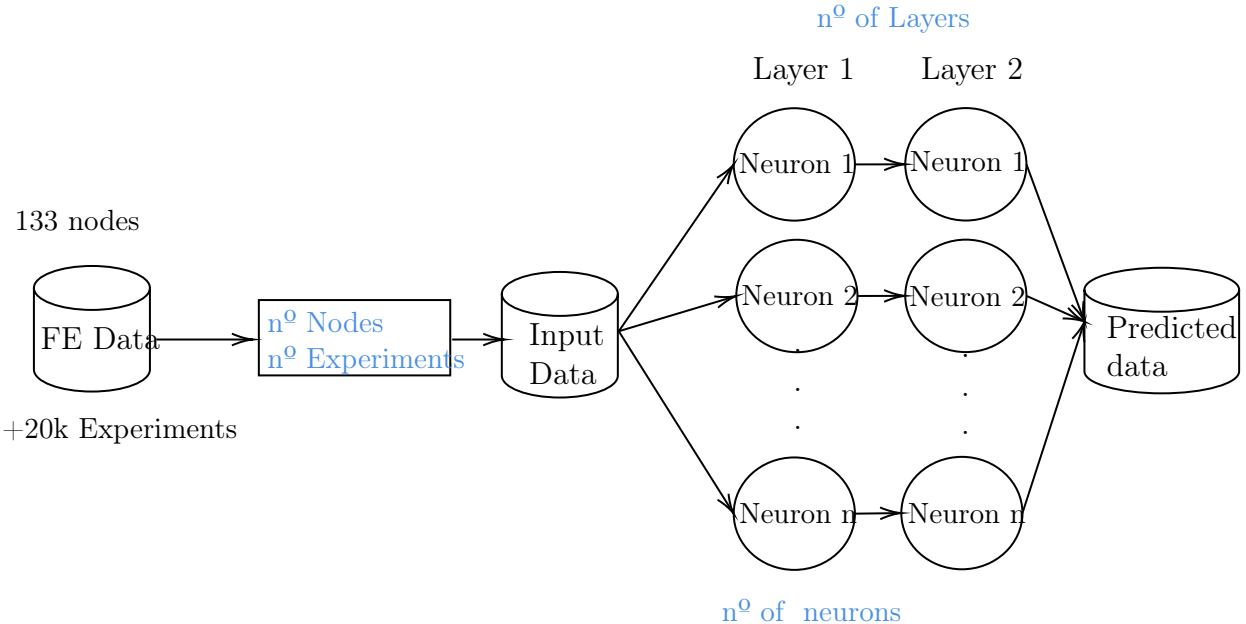


Figure 30: Training process schematic. The number of variables modified during the parametric study can be seen in blue.

stage. There is no clear direction in which the hyperparameters of the neural network need to be changed in order to achieve reasonable prediction capabilities. For this reason, a parametric study was carried out in which neural network calibration is done by varying different hyperparameter values. Namely: the number of nodes ( $n_{nodes}$ ), the number of neurons ( $n_{neurons}$ ), the number of experiments ( $n_{experiments}$ ) and the number of layers ( $n_{layers}$ ). To study the convergence of the machine learning model, the number of epochs was also introduced in the parametric study.

Alongside architecture-specific parameters, like the number of neurons, the number of layers and the number of epochs, we also studied the effect of the number of nodes and experiments. From the available 133 nodes, we took only a subset of them and used them to train the neural network, leaving the remaining nodes as test data to compare against. The same concept is used by selecting only a subset of experiments out of the ones available. The purpose of this subset selection is calibrating a neural network that is able to predict the complete response, reducing the computational expense without losing accuracy by reducing the number of nodes and experiments used.

For each of the hyperparameters specified, the values studied were the following:

Parameters	Value			
Layers	2	3	4	6
Neurons	10	20	40	-
Experiments	200	1000	2000	4000
Nodes	10	30	40	-
Epochs	500	1000	5000	-

Table 12: Values used in the parametric study during the training phase. Every combination of these parameters was analysed and parsed to obtain the best performing architecture.

Every possible combination of these parameters was studied, totalling 200 different architectures that were run and analysed. To measure the performance of these architecture, the R2 measurement (92), was used. This metric allows us to compare the displacements predicted by the neural network against the test data (the remaining data that was not taken into the training process). To provide a clearer outlook on the results of the parametric hyperparameter study, we

compiled the output of R2 measurements on every combination of 10 and 30 nodes using 2000 and 4000 experiments with 5000 epochs. These results can be visualized in Table ??

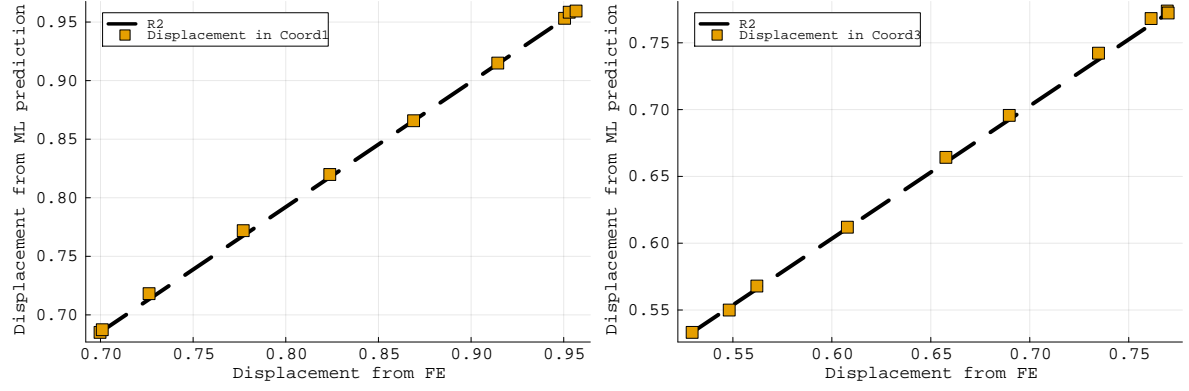
$n_{nodes} = 10$		$n_{neurons}$		
$n_{experiments} = 4000$		10	20	40
$n_{layers}$	2	0.964	0.951	0.966
	3	0.973	0.999	0.999
	4	0.998	0.996	0.998
	6	0.990	0.998	0.999
$n_{nodes} = 10$		$n_{neurons}$		
$n_{experiments} = 2000$		10	20	40
$n_{layers}$	2	0.946	0.956	0.960
	3	0.996	0.999	0.997
	4	0.995	0.999	0.998
	6	0.994	0.998	0.998
$n_{nodes} = 30$		$n_{neurons}$		
$n_{experiments} = 4000$		10	20	40
$n_{layers}$	2	0.932	0.950	0.964
	3	0.990	0.994	0.997
	4	0.992	0.997	0.999
	6	0.991	0.996	0.998
$n_{nodes} = 30$		$n_{neurons}$		
$n_{experiments} = 2000$		10	20	40
$n_{layers}$	2	0.953	0.944	0.979
	3	0.987	0.994	0.996
	4	0.993	0.997	0.997
	6	0.989	0.995	0.998

Table 13: R2 measurement for every combination of neurons and layers for 10 and 20 nodes and 2000 and 4000 experiments. These results were obtained using 5000 epochs.

Out of the analysed architectures in Table 13, the best configuration is a combination of 4 layers, 20 neurons, 2000 experiments, 10 nodes and 5000 iterations with an R2 on the test cases of 0.9994. To further visualize this result, we plotted the output displacement from the FE analysis against the displacement predicted by the best performing architecture. Since the displacement data is given per axis in the global coordinate system, we compared the displacement per axis; namely the first and third axis. The output of this analysis is displayed in Figure 31

As can be seen from Figure 31, there is a high correlation between the predicted data from the neural network and the data coming from the FE analysis, which was also indicated by a high R2 value.

To further analyse the performance of the machine learning architecture, we can plot the loss function during the training process, which exhibits a downward tendency as the training progresses. This result can be seen in Figure 32. Furthermore, we can see that the training is fully converged, as there is no significant variation in the lost function after 2000 epochs.



(a) Displacement in the first axis of the coordinate system (b) Displacement in the third axis of the coordinate system

Figure 31: R2 evaluation of the displacements. FE data vs ML predicted output for the better performing neural network architecture at sampling point 18673. A clear linear distribution can be seen between the predicted and FE displacements, indicating a high R2 and correlation between the data

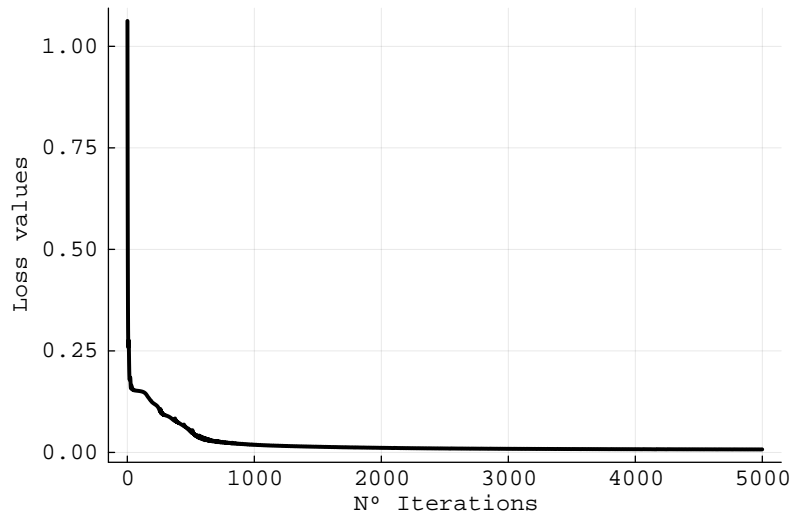


Figure 32: Loss function during the training for the best performant neural network configuration. Convergence is achieved after approximately 2000 training epochs.

## **9. Acknowledgements**

The first author acknowledges the support provided by Ministerio de Ciencia, Innovación y Universidades, for the award of a Juan de la Cierva Formación Fellowship. The first and third author acknowledge the support of AEI/FEDER and UE under the contracts DPI2016-77538-R and by Fundacion Séneca (Agencia de Ciencia y Tecnología de la Región de Murcia (Spain)) under the contract 20911/PI/18. The second author acknowledges the financial support received through the European Training Network Protection (Project ID: 764636).

## Appendix A. Entropy-based EM scheme

Although not pursued in this work, it is possible to define an entropy-based EM time integrator, counterpart of that in (??). For that we introduce first the entropy-based counterpart of the weak forms in (A.1), i.e.

$$\begin{aligned}\mathcal{W}_v &= \int_{\mathcal{B}_0} (\mathbf{v} - \dot{\phi}) \cdot \rho_0 \mathbf{w}_v \, dV = 0; \\ \mathcal{W}_\phi &= \int_{\mathcal{B}_0} \rho_0 \dot{\mathbf{v}} \cdot \mathbf{w}_\phi \, dV + \int_{\mathcal{B}_0} \mathbf{S} : \frac{1}{2} D\mathbf{C}[\mathbf{w}_\phi] \, dV - \int_{\mathcal{B}_0} \mathbf{f}_0 \cdot \mathbf{w}_\phi \, dV - \int_{\partial_t \mathcal{B}_0} \mathbf{t}_0 \cdot \mathbf{w}_\phi \, dA = 0; \\ \mathcal{W}_\eta &= \int_{\mathcal{B}_0} \theta \dot{\eta} w_\eta \, dV - \int_{\mathcal{B}_0} \mathbf{Q} \cdot \nabla_0 w_\eta \, dV - \int_{\mathcal{B}_0} R_\theta w_\eta \, dV - \int_{\partial_Q \mathcal{B}_0} Q_\theta w_\eta \, dA = 0,\end{aligned}\quad (\text{A.1})$$

where  $\{\mathbf{v}, \phi, \eta\} \in \mathbb{V}^\phi \times \mathbb{V}^\phi \times \mathbb{V}^\theta$  and  $\{\mathbf{w}_v, \mathbf{w}_\phi, w_\eta\} \in \mathbb{V}_0^\phi \times \mathbb{V}_0^\phi \times \mathbb{V}_0^\theta\}$  in (59). Notice that in order to obtain (A.1)<sub>c</sub>, the classical local form in (5) needs to be used, rather than its equivalent counterpart in (??). In order to design the entropy-based EM momentum from (A.1), we strictly follow the steps enumerated in Remark 1, yielding

$$\begin{aligned}(\mathcal{W}_v)_{\text{algo}} &= \int_{\mathcal{B}_0} \left( \mathbf{v}_{n+1/2} - \frac{\Delta\phi}{\Delta t} \right) \cdot \rho_0 \mathbf{w}_v \, dV = 0; \\ (\mathcal{W}_\phi)_{\text{algo}} &= \int_{\mathcal{B}_0} \rho_0 \frac{\Delta\mathbf{v}}{\Delta t} \cdot \mathbf{w}_\phi \, dV + \int_{\mathcal{B}_0} \mathbf{S}_{\text{algo}} : \frac{1}{2} (D\mathbf{C}[\mathbf{w}_\phi])_{\text{algo}} \, dV - \int_{\mathcal{B}_0} \mathbf{f}_{0_{n+1/2}} \cdot \mathbf{w}_\phi \, dV \\ &\quad - \int_{\partial_t \mathcal{B}_0} \mathbf{t}_{0_{n+1/2}} \cdot \mathbf{w}_\phi \, dA = 0; \\ (\mathcal{W}_\eta)_{\text{algo}} &= \int_{\mathcal{B}_0} \theta_{\text{algo}} \frac{\Delta\eta}{\Delta t} w_\eta \, dV - \int_{\mathcal{B}_0} \mathbf{Q}_{n+1/2} \cdot \nabla_0 w_\eta \, dV - \int_{\mathcal{B}_0} R_{\theta n+1/2} w_\eta \, dV - \int_{\partial_Q \mathcal{B}_0} Q_{\theta n+1/2} w_\eta \, dA = 0,\end{aligned}\quad (\text{A.2})$$

where the algorithmic expressions  $\{\mathbf{S}_{\text{algo}}, \theta_{\text{algo}}\}$  are defined as

$$\mathbf{S}_{\text{algo}} = 2D\mathbf{C}\tilde{U} + 2D\mathbf{G}\tilde{U} \times \mathbf{C}_{\text{algo}} + 2D_C\tilde{U}\mathbf{G}_{\text{algo}}; \quad \theta_{\text{algo}} = D_\eta\tilde{U}, \quad (\text{A.3})$$

and with  $\mathbf{C}_{\text{algo}}$  and  $\mathbf{G}_{\text{algo}}$  in (??). Following a similar procedure to that in Sections ?? and ??, it is possible to prove that the EM time integrator in (A.2) preserves both linear and angular momentum for vanishing external forces. With regards to its energy conservation properties, we replace in (A.2)  $\{\mathbf{w}_v, \mathbf{w}_\phi\}$  with  $\{\Delta\mathbf{v}/\Delta t, \Delta\phi/\Delta t\} \in \mathbb{V}_0^\phi \times \mathbb{V}_0^\phi$  and  $w_\eta = 1$ , yielding

$$\frac{\Delta K}{\Delta t} + \int_{\mathcal{B}_0} \frac{1}{\Delta t} \left( D\mathbf{C}\tilde{U} : \Delta\mathbf{C} + D\mathbf{G}\tilde{U} : \Delta\mathbf{G} + D_C\tilde{U}\Delta C + D_\eta\tilde{U}\Delta\eta \right) \, dV - \frac{\Delta\Pi_{\text{ext}}(\phi)}{\Delta t} - \mathcal{Q}_{\text{ext}} = 0. \quad (\text{A.4})$$

Therefore, from (A.4), the directionality property for the entropy-based formulation must be<sup>6</sup>

$$D\mathbf{C}\tilde{U} : \Delta\mathbf{C} + D\mathbf{G}\tilde{U} : \Delta\mathbf{G} + D_C\tilde{U}\Delta C + D_\eta\tilde{U}\Delta\eta = \Delta\tilde{U}. \quad (\text{A.5})$$

A definition of the discrete derivatives  $\{D_C\tilde{U}, D\mathbf{G}\tilde{U}, D_C\tilde{U}, D_\theta\tilde{U}\}$  based on the derivation presented in [14] for energies depending upon several arguments ensures the satisfaction of (A.5) (see also Appendix B, where  $\tilde{W}$  and  $\theta$  need to be simply replaced with  $\tilde{U}$  and  $\eta$ , respectively). Based on this definition of the discrete derivatives equation (A.4) can be finally written as

$$\frac{\Delta K}{\Delta t} + \int_{\mathcal{B}_0} \frac{\Delta\tilde{U}}{\Delta t} \, dV - \frac{\Delta\Pi_{\text{ext}}(\phi)}{\Delta t} - \mathcal{Q}_{\text{ext}} = 0, \quad (\text{A.6})$$

---

<sup>6</sup>see its temperature-based counterpart in (??)

which is completely equivalent to the result obtained for the temperature-based counterpart in (??). Equation (A.6) ensures the consistency of the entropy-based EM time integrator (A.2). It is convenient to recall that the main drawback of entropy-based formulations is that in general, it might not be possible to find an explicit representation of the internal energy functional (and of its derivatives). However, for the Helmholtz functional presented in Section ?? we have been able to obtain a simple explicit expression for its associated internal energy (see (??) and (??)).

## Appendix B. Discrete derivatives of the internal energy

### Appendix B.1. Definition of the discrete derivatives

Let us introduce the following notation,  $\{\mathcal{V}_1, \mathcal{V}_2, \mathcal{V}_3, \mathcal{V}_4\} = \{\mathbf{C}, \mathbf{G}, C, \theta\}$ . This will facilitate the definition of the discrete derivatives  $D_{\tilde{\mathcal{V}}_1}\tilde{W} = D_{\mathbf{C}}\tilde{W}$ ,  $D_{\tilde{\mathcal{V}}_2}\tilde{W} = D_{\mathbf{G}}\tilde{W}$  and  $D_{\tilde{\mathcal{V}}_3}\tilde{W} = D_C\tilde{W}$  in (??) and  $D_{\tilde{\mathcal{V}}_4}\tilde{W} = D_\theta\tilde{W}$  in (??)<sub>d</sub>.

$$\begin{aligned} D_{\tilde{\mathcal{V}}_i}\tilde{W} &= \frac{1}{2} \left( D_{\tilde{\mathcal{V}}_{i_{n+1,n}}} \tilde{W} + D_{\tilde{\mathcal{V}}_{i_{n,n+1}}} \tilde{W} \right); & i \in Y = \{1, 2, 3, 4\}; \\ D_{\tilde{\mathcal{V}}_{i_{n+1,n}}}\tilde{W} &= D_{\tilde{\mathcal{V}}_i}\tilde{W} \left( \tilde{\mathcal{V}}_{i_{n+1}}, \tilde{\mathcal{V}}_{i_n} \right) \Big|_{\tilde{\mathcal{V}}_{j_{n+1}}, \tilde{\mathcal{V}}_{k_n}}; & \forall j \in Y : j < i; \quad \forall k \in Y : k > i; \\ D_{\tilde{\mathcal{V}}_{i_{n,n+1}}}\tilde{W} &= D_{\tilde{\mathcal{V}}_i}\tilde{W} \left( \tilde{\mathcal{V}}_{i_n}, \tilde{\mathcal{V}}_{i_{n+1}} \right) \Big|_{\tilde{\mathcal{V}}_{j_n}, \tilde{\mathcal{V}}_{k_{n+1}}}; & \forall j \in Y : j < i; \quad \forall k \in Y : k > i, \end{aligned} \quad (\text{B.1})$$

where the discrete operators  $D_{\tilde{\mathcal{V}}_i}\tilde{W} \Big|_{\tilde{\mathcal{V}}_{j_{n+1}}, \tilde{\mathcal{V}}_{k_n}}$  and  $D_{\tilde{\mathcal{V}}_i}\tilde{W} \Big|_{\tilde{\mathcal{V}}_{j_n}, \tilde{\mathcal{V}}_{k_{n+1}}}$  are defined as

$$\begin{aligned} D_{\tilde{\mathcal{V}}_i}\tilde{W} \Big|_{\tilde{\mathcal{V}}_{j_{n+1}}, \tilde{\mathcal{V}}_{k_n}} &= \partial_{\tilde{\mathcal{V}}_i}\tilde{W} \left( \tilde{\mathcal{V}}_{n+1/2} \right) \Big|_{\tilde{\mathcal{V}}_{j_{n+1}}, \tilde{\mathcal{V}}_{k_n}} \\ &\quad + \frac{\tilde{W} \left( \tilde{\mathcal{V}}_{n+1} \right) \Big|_{\tilde{\mathcal{V}}_{j_{n+1}}, \tilde{\mathcal{V}}_{k_n}} - \tilde{W} \left( \tilde{\mathcal{V}}_n \right) \Big|_{\tilde{\mathcal{V}}_{j_{n+1}}, \tilde{\mathcal{V}}_{k_n}} - \partial_{\tilde{\mathcal{V}}_i}\tilde{W} \left( \tilde{\mathcal{V}}_{n+1/2} \right) \Big|_{\tilde{\mathcal{V}}_{j_{n+1}}, \tilde{\mathcal{V}}_{k_n}}}{||\Delta\tilde{\mathcal{V}}_i||^2} : \Delta\tilde{\mathcal{V}}_i \\ D_{\tilde{\mathcal{V}}_i}\tilde{W} \Big|_{\tilde{\mathcal{V}}_{j_n}, \tilde{\mathcal{V}}_{k_{n+1}}} &= \partial_{\tilde{\mathcal{V}}_i}\tilde{W} \left( \tilde{\mathcal{V}}_{n+1/2} \right) \Big|_{\tilde{\mathcal{V}}_{j_n}, \tilde{\mathcal{V}}_{k_{n+1}}} \\ &\quad + \frac{\tilde{W} \left( \tilde{\mathcal{V}}_{n+1} \right) \Big|_{\tilde{\mathcal{V}}_{j_n}, \tilde{\mathcal{V}}_{k_{n+1}}} - \tilde{W} \left( \tilde{\mathcal{V}}_n \right) \Big|_{\tilde{\mathcal{V}}_{j_n}, \tilde{\mathcal{V}}_{k_{n+1}}} - \partial_{\tilde{\mathcal{V}}_i}\tilde{W} \left( \tilde{\mathcal{V}}_{n+1/2} \right) \Big|_{\tilde{\mathcal{V}}_{j_n}, \tilde{\mathcal{V}}_{k_{n+1}}}}{||\Delta\tilde{\mathcal{V}}_i||^2} : \Delta\tilde{\mathcal{V}}_i. \end{aligned} \quad (\text{B.2})$$

Let us introduce the following set  $\tilde{\mathcal{V}}_C = \tilde{\mathcal{V}} \setminus \{\mathbf{C}\}$ , i.e.  $\mathcal{V}_C = \{\mathbf{G}, C, \theta\}$ . From above equations (B.1) and (B.2), the directional derivative  $D_C\tilde{W}$  can be computed as

$$\begin{aligned} D_C\tilde{W} &= \frac{1}{2} \left( \partial_C\tilde{W} \left( \mathbf{C}_{n+1/2}, \tilde{\mathcal{V}}_{1_{n+1}} \right) + \partial_C\tilde{W} \left( \mathbf{C}_{n+1/2}, \tilde{\mathcal{V}}_{C_n} \right) \right) \\ &\quad + \frac{1}{2} \frac{\tilde{W} \left( \mathbf{C}_{n+1}, \tilde{\mathcal{V}}_{1_{n+1}} \right) - \tilde{W} \left( \mathbf{C}_n, \tilde{\mathcal{V}}_{1_{n+1}} \right)}{||\Delta\mathbf{C}||^2} \Delta\mathbf{C} + \frac{1}{2} \frac{\tilde{W} \left( \mathbf{C}_{n+1}, \tilde{\mathcal{V}}_{C_n} \right) - \tilde{W} \left( \mathbf{C}_n, \tilde{\mathcal{V}}_{C_n} \right)}{||\Delta\mathbf{C}||^2} \Delta\mathbf{C} \\ &\quad - \frac{1}{2} \frac{\partial_C\tilde{W} \left( \mathbf{C}_{n+1/2}, \tilde{\mathcal{V}}_{1_{n+1}} \right) : \Delta\mathbf{C}}{||\Delta\mathbf{C}||^2} \Delta\mathbf{C} - \frac{1}{2} \frac{\partial_C\tilde{W} \left( \mathbf{C}_{n+1/2}, \tilde{\mathcal{V}}_{C_n} \right) : \Delta\mathbf{C}}{||\Delta\mathbf{C}||^2} \Delta\mathbf{C}. \end{aligned} \quad (\text{B.3})$$

From the previous equation, the discrete derivatives with respect to  $\mathbf{C}$  when  $\tilde{\mathcal{V}}_{C_{n+1}}$  and  $\tilde{\mathcal{V}}_{C_n}$  are kept fixed are defined as

$$\begin{aligned} D_C\tilde{W}(\bullet, \tilde{\mathcal{V}}_{C_{n+1}}) &:= \partial_C\tilde{W} \left( \mathbf{C}_{n+1/2}, \tilde{\mathcal{V}}_{C_{n+1}} \right) \\ &\quad + \frac{\tilde{W} \left( \mathbf{C}_{n+1}, \tilde{\mathcal{V}}_{C_{n+1}} \right) - \tilde{W} \left( \mathbf{C}_n, \tilde{\mathcal{V}}_{C_{n+1}} \right) - \partial_C\tilde{W} \left( \mathbf{C}_{n+1/2}, \tilde{\mathcal{V}}_{C_{n+1}} \right) : \Delta\mathbf{C}}{||\Delta\mathbf{C}||^2} \Delta\mathbf{C}; \\ D_C\tilde{W}(\bullet, \tilde{\mathcal{V}}_{C_n}) &:= \partial_C\tilde{W} \left( \mathbf{C}_{n+1/2}, \tilde{\mathcal{V}}_{C_n} \right) \\ &\quad + \frac{\tilde{W} \left( \mathbf{C}_{n+1}, \tilde{\mathcal{V}}_{C_n} \right) - \tilde{W} \left( \mathbf{C}_n, \tilde{\mathcal{V}}_{C_n} \right) - \partial_C\tilde{W} \left( \mathbf{C}_{n+1/2}, \tilde{\mathcal{V}}_{C_n} \right) : \Delta\mathbf{C}}{||\Delta\mathbf{C}||^2} \Delta\mathbf{C}. \end{aligned} \quad (\text{B.4})$$

Therefore, equation (B.3) can be conveniently written in a compact manner as

$$D_C \widetilde{W} = \frac{1}{2} \left( D_C \widetilde{W}(\bullet, \tilde{\mathcal{V}}_{C_{n+1}}) + D_C \widetilde{W}(\bullet, \tilde{\mathcal{V}}_{C_n}) \right). \quad (\text{B.5})$$

Similarly, defining the following sets  $\tilde{\mathcal{V}}_G = \tilde{\mathcal{V}} \setminus \{G\}$ ,  $\tilde{\mathcal{V}}_C = \tilde{\mathcal{V}} \setminus \{C\}$  and  $\tilde{\mathcal{V}}_\theta = \tilde{\mathcal{V}} \setminus \{\theta\}$ , it is possible to express the directional derivatives  $D_G \widetilde{W}$ ,  $D_C \widetilde{W}$  and  $D_\theta \widetilde{W}$  as

$$\begin{aligned} D_G \widetilde{W} &= \frac{1}{2} \left( D_G \widetilde{W}(\bullet, \mathcal{V}_{G_{n+1}}) + D_G \widetilde{W}(\bullet, \mathcal{V}_{G_n}) \right); \\ D_C \widetilde{W} &= \frac{1}{2} \left( D_C \widetilde{W}(\bullet, \mathcal{V}_{C_{n+1}}) + D_C \widetilde{W}(\bullet, \mathcal{V}_{C_n}) \right); \\ D_\theta \widetilde{W} &= \frac{1}{2} \left( D_\theta \widetilde{W}(\bullet, \mathcal{V}_{\theta_{n+1}}) + D_\theta \widetilde{W}(\bullet, \mathcal{V}_{\theta_n}) \right). \end{aligned} \quad (\text{B.6})$$

In the particular case of the last two directional derivatives (with respect to  $C$  and  $\theta$ ), the terms  $D_C \widetilde{W}(\bullet, \mathcal{V}_{C_{n+1}})$  (and  $D_C \widetilde{W}(\bullet, \mathcal{V}_{C_n})$ ) and  $D_\theta \widetilde{W}(\bullet, \mathcal{V}_{\theta_{n+1}})$  (and similarly  $D_\theta \widetilde{W}(\bullet, \mathcal{V}_{\theta_n})$ ) are extremely simplified since  $C$  and  $\theta$  are scalar fields, i.e.

$$\begin{aligned} D_C \widetilde{W}(\bullet, \mathcal{V}_{C_{n+1}}) &= \frac{\widetilde{W}(C_{n+1}, \mathcal{V}_{C_{n+1}}) - \widetilde{W}(C_n, \mathcal{V}_{C_{n+1}})}{\Delta C}; \\ D_\theta \widetilde{W}(\bullet, \mathcal{V}_{\theta_{n+1}}) &= \frac{\widetilde{W}(\theta_{n+1}, \mathcal{V}_{\theta_{n+1}}) - \widetilde{W}(\theta_n, \mathcal{V}_{\theta_{n+1}})}{\Delta \theta}; \end{aligned} \quad (\text{B.7})$$

In particular, for the Mooney-Rivlin model in equation (??) and (??), the tensor discrete derivatives  $\{D_C \widetilde{W}, D_G \widetilde{W}\}$  adopt the following extremely simple expressions

$$D_C \widetilde{W} = \frac{\mu_1}{2} \mathbf{I}; \quad D_G \widetilde{W} = \frac{\mu_2}{2} \mathbf{I}. \quad (\text{B.8})$$

### Appendix B.2. Proof of directionality property

The objective of this section is to prove that the definition of the discrete derivatives of the internal energy  $\widetilde{W}(\mathbf{C}, \mathbf{G}, C, \theta)$  in (B.1) and (B.2) satisfy the directionality property in equation (??). For that, let us denote the expression on the left-hand side of the directionality property in (??) as  $\mathcal{T}$ , namely

$$\mathcal{T} = D_C W : \Delta \mathbf{C} + D_G W : \Delta \mathbf{G} + D_C W \Delta C + D_\theta W \cdot \Delta \theta. \quad (\text{B.9})$$

Substitution of the expressions for  $D_C \widetilde{W}$  (B.3),  $D_G \widetilde{W}$  (B.6),  $D_C \widetilde{W}$  (B.6) and  $D_\theta \widetilde{W}$  (B.6) into (B.9) leads to

$$\begin{aligned} \mathcal{T} &= \frac{1}{2} \widetilde{W}(\mathbf{C}_{n+1}, \mathbf{G}_{n+1}, C_{n+1}, \theta_{n+1}) - \frac{1}{2} \widetilde{W}(\mathbf{C}_n, \mathbf{G}_{n+1}, C_{n+1}, \theta_{n+1}) \\ &\quad + \frac{1}{2} \widetilde{W}(\mathbf{C}_{n+1}, \mathbf{G}_n, C_n, \theta_n) - \frac{1}{2} \widetilde{W}(\mathbf{C}_n, \mathbf{G}_n, C_n, \theta_n) \\ &\quad + \frac{1}{2} \widetilde{W}(\mathbf{C}_n, \mathbf{G}_{n+1}, C_{n+1}, \theta_{n+1}) - \frac{1}{2} \widetilde{W}(\mathbf{C}_n, \mathbf{G}_n, C_{n+1}, \theta_{n+1}) \\ &\quad + \frac{1}{2} \widetilde{W}(\mathbf{C}_{n+1}, \mathbf{G}_{n+1}, C_n, \theta_n) - \frac{1}{2} \widetilde{W}(\mathbf{C}_{n+1}, \mathbf{G}_n, C_n, \theta_n) \\ &\quad + \frac{1}{2} \widetilde{W}(\mathbf{C}_n, \mathbf{G}_n, C_{n+1}, \theta_{n+1}) - \frac{1}{2} \widetilde{W}(\mathbf{C}_n, \mathbf{G}_n, C_n, \theta_{n+1}) \\ &\quad + \frac{1}{2} \widetilde{W}(\mathbf{C}_{n+1}, \mathbf{G}_{n+1}, C_{n+1}, \theta_n) - \frac{1}{2} \widetilde{W}(\mathbf{C}_{n+1}, \mathbf{G}_{n+1}, C_n, \theta_n) \\ &\quad + \frac{1}{2} \widetilde{W}(\mathbf{C}_n, \mathbf{G}_n, C_n, \theta_{n+1}) - \frac{1}{2} \widetilde{W}(\mathbf{C}_n, \mathbf{G}_n, C_n, \theta_n) \\ &\quad + \frac{1}{2} \widetilde{W}(\mathbf{C}_{n+1}, \mathbf{G}_{n+1}, C_{n+1}, \theta_{n+1}) - \frac{1}{2} \widetilde{W}(\mathbf{C}_{n+1}, \mathbf{G}_{n+1}, C_{n+1}, \theta_n) \\ &= \Delta \widetilde{W}, \end{aligned} \quad (\text{B.10})$$

which proves that the definition of the discrete derivatives satisfy the directionality property.

### Appendix B.3. Definition of the discrete derivatives in the limit

The objective of this section is to prove that the defition of the directional derivatives in equations (B.1) and (B.2) satisfies the second condition stated in Section ??, namely that they are well defined in the limit  $\|\Delta\mathbf{C}\| \rightarrow 0$ ,  $\|\Delta\mathbf{G}\| \rightarrow 0$ ,  $\|\Delta\mathbf{C}\| \rightarrow 0$  and  $\|\Delta\theta\| \rightarrow 0$ . In particular, it will be proved in this Section that based on the definition of the discrete derivatives, these can be equivalently written as

$$D_{\tilde{\mathcal{V}}_i} \widetilde{W} = \partial_{\tilde{\mathcal{V}}_i} \widetilde{W} \left( \tilde{\mathcal{V}}_{n+1/2} \right) + \sum_{i=1}^4 O \left( \|\Delta\tilde{\mathcal{V}}_i\|^2 \right) + \sum_{j=1, j \neq i}^4 \sum_{k=j+1, k \neq 1}^4 O \left( \|\Delta\tilde{\mathcal{V}}_j\| \|\Delta\tilde{\mathcal{V}}_k\| \right), \quad (\text{B.11})$$

which would prove that they are well defined in the limit. For that, let us carry out a Taylor series expansion of the four different evaluations of the internal energy  $\widetilde{W}$  in equation (B.3) around  $\mathbf{C}_{n+1/2}$ . This enables to express them as

$$\begin{aligned} \widetilde{W} \left( \mathbf{C}_{n+1}, \tilde{\mathcal{V}}_{\mathbf{C}_{n+1}} \right) &= \widetilde{W} \left( \mathbf{C}_{n+1/2}, \tilde{\mathcal{V}}_{\mathbf{C}_{n+1}} \right) + \partial_{\mathbf{C}} \widetilde{W} \left( \mathbf{C}_{n+1/2}, \tilde{\mathcal{V}}_{\mathbf{C}_{n+1}} \right) : \left( \frac{1}{2} \Delta \mathbf{C} \right) \\ &\quad + \left( \frac{1}{2} \Delta \mathbf{C} \right) : \partial_{\mathbf{CC}}^2 \widetilde{W} \left( \mathbf{C}_{n+1/2}, \tilde{\mathcal{V}}_{\mathbf{C}_{n+1}} \right) : \left( \frac{1}{2} \Delta \mathbf{C} \right) + O \left( \|\Delta \mathbf{C}\|^3 \right); \\ \widetilde{W} \left( \mathbf{C}_n, \tilde{\mathcal{V}}_{\mathbf{C}_{n+1}} \right) &= \widetilde{W} \left( \mathbf{C}_{n+1/2}, \tilde{\mathcal{V}}_{\mathbf{C}_{n+1}} \right) - \partial_{\mathbf{C}} \widetilde{W} \left( \mathbf{C}_{n+1/2}, \tilde{\mathcal{V}}_{\mathbf{C}_{n+1}} \right) : \left( \frac{1}{2} \Delta \mathbf{C} \right) \\ &\quad + \left( \frac{1}{2} \Delta \mathbf{C} \right) : \partial_{\mathbf{CC}}^2 \widetilde{W} \left( \mathbf{C}_{n+1/2}, \tilde{\mathcal{V}}_{\mathbf{C}_{n+1}} \right) : \left( \frac{1}{2} \Delta \mathbf{C} \right) + O \left( \|\Delta \mathbf{C}\|^3 \right); \\ \widetilde{W} \left( \mathbf{C}_{n+1}, \tilde{\mathcal{V}}_{\mathbf{C}_n} \right) &= \widetilde{W} \left( \mathbf{C}_{n+1/2}, \tilde{\mathcal{V}}_{\mathbf{C}_n} \right) + \partial_{\mathbf{C}} \widetilde{W} \left( \mathbf{C}_{n+1/2}, \tilde{\mathcal{V}}_{\mathbf{C}_n} \right) : \left( \frac{1}{2} \Delta \mathbf{C} \right) \\ &\quad + \left( \frac{1}{2} \Delta \mathbf{C} \right) : \partial_{\mathbf{CC}}^2 \widetilde{W} \left( \mathbf{C}_{n+1/2}, \tilde{\mathcal{V}}_{\mathbf{C}_n} \right) : \left( \frac{1}{2} \Delta \mathbf{C} \right) + O \left( \|\Delta \mathbf{C}\|^3 \right); \\ \widetilde{W} \left( \mathbf{C}_n, \tilde{\mathcal{V}}_{\mathbf{C}_n} \right) &= \widetilde{W} \left( \mathbf{C}_{n+1/2}, \tilde{\mathcal{V}}_{\mathbf{C}_n} \right) - \partial_{\mathbf{C}} \widetilde{W} \left( \mathbf{C}_{n+1/2}, \tilde{\mathcal{V}}_{\mathbf{C}_n} \right) : \left( \frac{1}{2} \Delta \mathbf{C} \right) \\ &\quad + \left( \frac{1}{2} \Delta \mathbf{C} \right) : \partial_{\mathbf{CC}}^2 \widetilde{W} \left( \mathbf{C}_{n+1/2}, \tilde{\mathcal{V}}_{\mathbf{C}_n} \right) : \left( \frac{1}{2} \Delta \mathbf{C} \right) + O \left( \|\Delta \mathbf{C}\|^3 \right). \end{aligned} \quad (\text{B.12})$$

Introduction of above equation (B.12) into the last four terms on the right-hand side of equation (B.3) yields

$$\begin{aligned} \frac{1}{2} \frac{\widetilde{W} \left( \mathbf{C}_{n+1}, \tilde{\mathcal{V}}_{\mathbf{C}_{n+1}} \right) - \widetilde{W} \left( \mathbf{C}_n, \tilde{\mathcal{V}}_{\mathbf{C}_{n+1}} \right)}{\|\Delta \mathbf{C}\|^2} \Delta \mathbf{C} + \frac{1}{2} \frac{\widetilde{W} \left( \mathbf{C}_{n+1}, \tilde{\mathcal{V}}_{\mathbf{C}_n} \right) - \widetilde{W} \left( \mathbf{C}_n, \tilde{\mathcal{V}}_{\mathbf{C}_n} \right)}{\|\Delta \mathbf{C}\|^2} \Delta \mathbf{C} \\ - \frac{1}{2} \frac{\partial_{\mathbf{C}} \widetilde{W} \left( \mathbf{C}_{n+1/2}, \tilde{\mathcal{V}}_{\mathbf{C}_{n+1}} \right) : \Delta \mathbf{C}}{\|\Delta \mathbf{C}\|^2} \Delta \mathbf{C} - \frac{1}{2} \frac{\partial_{\mathbf{C}} \widetilde{W} \left( \mathbf{C}_{n+1/2}, \tilde{\mathcal{V}}_{\mathbf{C}_n} \right) : \Delta \mathbf{C}}{\|\Delta \mathbf{C}\|^2} \Delta \mathbf{C} = O \left( \|\Delta \mathbf{C}\|^2 \right). \end{aligned} \quad (\text{B.13})$$

Introduction of the result in (B.13) into the expression for the directional derivative  $D_{\mathbf{C}} \widetilde{W}$  in (??) leads to

$$D_{\mathbf{C}} \widetilde{W} = \frac{1}{2} \left( \partial_{\mathbf{C}} \widetilde{W} \left( \mathbf{C}_{n+1/2}, \tilde{\mathcal{V}}_{\mathbf{C}_{n+1}} \right) + \partial_{\mathbf{C}} \widetilde{W} \left( \mathbf{C}_{n+1/2}, \tilde{\mathcal{V}}_{\mathbf{C}_n} \right) \right) + O \left( \|\Delta \mathbf{C}\|^2 \right). \quad (\text{B.14})$$

A Taylor series expansion on the two first terms on the right-hand side of above equation (B.14) enables these to be expressed as

$$\begin{aligned}
\partial_C \widetilde{W}(\mathbf{C}_{n+1/2}, \tilde{\mathcal{V}}_{\mathbf{C}_{n+1}}) &= \partial_C \widetilde{W}(\mathbf{C}_{n+1/2}, \tilde{\mathcal{V}}_{\mathbf{C}_{n+1/2}}) + \partial_{\mathbf{CG}}^2 \widetilde{W}(\mathbf{C}_{n+1/2}, \tilde{\mathcal{V}}_{\mathbf{C}_{n+1/2}}) : \left( \frac{1}{2} \Delta \mathbf{G} \right) \\
&\quad + \partial_{CC}^2 \widetilde{W}(\mathbf{C}_{n+1/2}, \tilde{\mathcal{V}}_{\mathbf{C}_{n+1/2}}) \left( \frac{1}{2} \Delta C \right) + \partial_{C\theta}^2 \widetilde{W}(\mathbf{C}_{n+1/2}, \tilde{\mathcal{V}}_{\mathbf{C}_{n+1/2}}) : \left( \frac{1}{2} \Delta \theta \right) \\
&\quad + O(\|\Delta \mathbf{G}\|^2) + O(\Delta C^2) + O(\|\Delta \theta\|^2) \\
&\quad + O(\|\Delta \mathbf{G}\| \Delta C) + O(\|\Delta \mathbf{G}\| \|\Delta \theta\|) + O(\Delta C \|\Delta \theta\|); \\
\partial_C \widetilde{W}(\mathbf{C}_{n+1/2}, \tilde{\mathcal{V}}_{\mathbf{C}_n}) &= \partial_C \widetilde{W}(\mathbf{C}_{n+1/2}, \tilde{\mathcal{V}}_{\mathbf{C}_{n+1/2}}) - \partial_{\mathbf{CG}}^2 \widetilde{W}(\mathbf{C}_{n+1/2}, \tilde{\mathcal{V}}_{\mathbf{C}_{n+1/2}}) : \left( \frac{1}{2} \Delta \mathbf{G} \right) \\
&\quad - \partial_{CC}^2 \widetilde{W}(\mathbf{C}_{n+1/2}, \tilde{\mathcal{V}}_{\mathbf{C}_{n+1/2}}) \left( \frac{1}{2} \Delta C \right) - \partial_{C\theta}^2 \widetilde{W}(\mathbf{C}_{n+1/2}, \tilde{\mathcal{V}}_{\mathbf{C}_{n+1/2}}) : \left( \frac{1}{2} \Delta \theta \right) \\
&\quad + O(\|\Delta \mathbf{G}\|^2) + O(\Delta C^2) + O(\|\Delta \theta\|^2) \\
&\quad + O(\|\Delta \mathbf{G}\| \Delta C) + O(\|\Delta \mathbf{G}\| \|\Delta \theta\|) + O(\Delta C \|\Delta \theta\|).
\end{aligned} \tag{B.15}$$

Introduction of (B.15) into (B.14) leads to the final expression for  $D_C \widetilde{W}$  (B.3) as

$$\begin{aligned}
D_C \widetilde{W} &= \partial_C \widetilde{W}(\mathbf{C}_{n+1/2}, \tilde{\mathcal{V}}_{\mathbf{C}_{n+1/2}}) \\
&\quad + O(\|\Delta \mathbf{C}\|^2) + O(\|\Delta \mathbf{G}\|^2) + O(\Delta C^2) + O(\|\Delta \theta\|^2) \\
&\quad + O(\|\Delta \mathbf{G}\| \Delta C) + O(\|\Delta \mathbf{G}\| \|\Delta \theta\|) + O(\Delta C \|\Delta \theta\|),
\end{aligned} \tag{B.16}$$

which proves condition (B.11). Proceeding similarly, it would be possible to generalise above result (B.16) to the discrete derivatives  $D_G \widetilde{W}$ ,  $D_C \widetilde{W}$  and  $D_\theta \widetilde{W}$  (all of them in (B.6)), namely

$$\begin{aligned}
D_G \widetilde{W} &= \partial_G \widetilde{W}(\mathbf{C}_{n+1/2}, \tilde{\mathcal{V}}_{\mathbf{C}_{n+1/2}}) \\
&\quad + O(\|\Delta \mathbf{C}\|^2) + O(\|\Delta \mathbf{G}\|^2) + O(\Delta C^2) + O(\|\Delta \theta\|^2) \\
&\quad + O(\|\Delta \mathbf{C}\| \Delta C) + O(\|\Delta \mathbf{C}\| \|\Delta \theta\|) + O(\Delta C \|\Delta \theta\|); \\
D_C \widetilde{W} &= \partial_C \widetilde{W}(\mathbf{C}_{n+1/2}, \tilde{\mathcal{V}}_{\mathbf{C}_{n+1/2}}) \\
&\quad + O(\|\Delta \mathbf{C}\|^2) + O(\|\Delta \mathbf{G}\|^2) + O(\Delta C^2) + O(\|\Delta \theta\|^2) \\
&\quad + O(\|\Delta \mathbf{C}\| \|\Delta \mathbf{G}\|) + O(\|\Delta \mathbf{C}\| \|\Delta \theta\|) + O(\|\Delta \mathbf{G}\| \|\Delta \theta\|); \\
D_\theta \widetilde{W} &= \partial_\theta \widetilde{W}(\mathbf{C}_{n+1/2}, \tilde{\mathcal{V}}_{\mathbf{C}_{n+1/2}}) \\
&\quad + O(\|\Delta \mathbf{C}\|^2) + O(\|\Delta \mathbf{G}\|^2) + O(\Delta C^2) + O(\|\Delta \theta\|^2) \\
&\quad + O(\|\Delta \mathbf{C}\| \|\Delta \mathbf{G}\|) + O(\|\Delta \mathbf{C}\| \Delta C) + O(\|\Delta \mathbf{G}\| \Delta C).
\end{aligned} \tag{B.17}$$

## Appendix C. EM scheme in Reference [14]

### Appendix C.1. EM scheme

It is instructive to highlight the differences of the EM scheme in (??) and that previously developed in Reference [14]. The latter comprises the following algorithmic weak forms

$$\begin{aligned} (\mathcal{W}_v)_{\text{algo}} &= \int_{\mathcal{B}_0} \left( \mathbf{v}_{n+1/2} - \frac{\Delta\phi}{\Delta t} \right) \cdot \rho_0 \mathbf{w}_v \, dV = 0; \\ (\mathcal{W}_\phi)_{\text{algo}} &= \int_{\mathcal{B}_0} \rho_0 \frac{\Delta\mathbf{v}}{\Delta t} \cdot \mathbf{w}_\phi \, dV + \int_{\mathcal{B}_0} \mathbf{S}_{\text{algo}} : \frac{1}{2} (D\mathbf{C}[\mathbf{w}_\phi])_{\text{algo}} \, dV - \int_{\mathcal{B}_0} \mathbf{f}_{0_{n+1/2}} \cdot \mathbf{w}_\phi \, dV \\ &\quad - \int_{\partial_t \mathcal{B}_0} \mathbf{t}_{0_{n+1/2}} \cdot \mathbf{w}_\phi \, dA = 0; \\ (\mathcal{W}_\theta)_{\text{algo}} &= \int_{\mathcal{B}_0} \frac{\Delta\theta}{\Delta t} w_\theta \, dV + \int_{\mathcal{B}_0} \left( \frac{\Delta\mathbf{C}}{\Delta t} : \mathbf{G}_{n+1/2} \right) (D_\theta \eta)^{-1} (\partial_C \eta_{n+1/2}) w_\theta \, dV \\ &\quad - \int_{\mathcal{B}_0} \mathbf{Q}_{n+1/2} \cdot \nabla_0 ((D_\theta \hat{U})^{-1} w_\theta) \, dV - \int_{\mathcal{B}_0} (D_\theta \hat{U})^{-1} R_{\theta n+1/2} w_\theta \, dV \\ &\quad - \int_{\partial_Q \mathcal{B}_0} (D_\theta \hat{U})^{-1} Q_{\theta n+1/2} w_\theta \, dA = 0. \end{aligned} \tag{C.1}$$

In above equation (C.1),  $\mathbf{S}_{\text{algo}}$  is defined as

$$\mathbf{S}_{\text{algo}} = 2 \left( D_C \hat{U} + D_{\mathbf{G}} \hat{U} \times \mathbf{C}_{\text{algo}} + D_C \hat{U} \mathbf{G}_{\text{algo}} - \theta_{\text{algo}} \partial_C \eta_{n+1/2} \mathbf{G}_{n+1/2} \right); \quad \theta_{\text{algo}} = D_\theta \hat{U} (D_\theta \eta)^{-1}, \tag{C.2}$$

with  $\mathbf{C}_{\text{algo}}$  and  $\mathbf{G}_{\text{algo}}$  in (??) and where the internal energy energy functional  $\hat{U}$  is defined as in equation (??), i.e.

$$\hat{U}(\mathbf{C}, \mathbf{G}, C, \theta) = \tilde{U}(\mathbf{C}, \mathbf{G}, C, \eta(C, \theta)) = \theta \eta(C, \theta) + \tilde{W}(\mathbf{C}, \mathbf{G}, C, \theta), \tag{C.3}$$

with the particularity that the entropy is re-expressed as a function  $\theta$  (and of  $C$ ). Apart from the fact that this formulation relies on the internal energy functional  $\hat{U}(\mathbf{C}, \mathbf{G}, C, \theta)$  (as opposed to the Helmholtz free energy functional  $\tilde{W}(\mathbf{C}, \mathbf{G}, C, \theta)$  for the EM scheme in (??)), the main differences between both approaches are:

1. The EM scheme in (C.1) relies on the local form (5), or more specifically on

$$\dot{\eta} + \frac{1}{\theta} \text{DIV} \mathbf{Q} - \frac{1}{\theta} R_\theta = 0, \tag{C.4}$$

wheareas the proposed scheme in (??) relies on the local form in (??).

2. The algorithmic stresses  $\mathbf{S}_{\text{algo}}$  in (C.2) (for the EM scheme in C.1) and in (??) (for the proposed EM scheme in (??)) differ considerably. In particular, the expression in equation (C.2) needs to incorporate a fourth term not present in equation (??). Notice that in the more generic case where the entropy could possibly depend also on  $\mathbf{C}$  and  $\mathbf{G}$  (and not just on  $C$ , as it has been assumed in this paper), this would entail the addition of two extra terms in (C.2) related to both  $\mathbf{C}$  and  $\mathbf{G}$ , bringing cumbersome difficulties in the formulation.
3. The second term on the right hand side of equation (C.1) (which entails more complexity for a consistent linearisation of the set of weak forms) is not present in the proposed EM scheme in (??).
4. The term  $\nabla_0((D_\theta \hat{U})^{-1} w_\theta)$  on equation (C.1)<sub>c</sub> can potentially entail excessive complexity when carrying out a consistent linearisation of (C.1)<sub>c</sub>. For the specific model considered in equations (??), (??) and (??) this is not the case, as this term is constant.
5. The EM scheme in (C.1) requires the definition of the discrete derivatives of the internal energy functional  $\hat{U}(\mathbf{C}, \mathbf{G}, C, \theta)$  and in addition, the discrete derivative of the entropy  $\eta(C, \theta)$ , namely  $D_\theta \eta$  (see (C.1)<sub>c</sub>).

## Appendix D. Thermo-elastic constitutive model

The objective of this appendix is to briefly recall the calorimetry considerations followed in order to derive the constitutive model presented in Section ???. For that, we start by re-expressing the internal energy  $\tilde{e}(\mathbf{C}, \eta)$  as a function of the absolute temperature as

$$\hat{e}(\mathbf{C}, \theta) = \tilde{e}(\mathbf{C}, \eta(\mathbf{C}, \theta)). \quad (\text{D.1})$$

Calorimetry principles permit to experimentally measure the change of internal energy as a function of the temperature (for a constant deformation) yielding

$$\partial_\theta \hat{e} = c_v, \quad (\text{D.2})$$

with  $c_v$  denoting the heat capacity of the material. Notice that above equation (D.2) can be equivalently written as

$$\partial_\theta \hat{e} = \partial_\eta \tilde{e} \partial_\theta \eta = \theta \partial_\theta \eta = c_v \Rightarrow \partial_\theta \eta = \frac{c_v}{\theta}. \quad (\text{D.3})$$

Integration of (D.3) results in

$$\int_{\eta(\mathbf{C}, \theta_R)}^{\eta(\mathbf{C}, \theta)} d\eta = \int_{\theta_R}^\theta \frac{c_v}{\theta} d\theta \Rightarrow \eta(\mathbf{C}, \theta) = \eta_R(\mathbf{C}) + c_v \ln \frac{\theta}{\theta_R}, \quad (\text{D.4})$$

with  $\eta_R(\mathbf{C}) := \eta(\mathbf{C}, \theta_R)$ . Since  $\eta = -\partial_\theta \tilde{\Psi}$  we can further integrate (D.4) as

$$\int_{\tilde{\Psi}(\mathbf{C}, \theta_R)}^{\tilde{\Psi}(\mathbf{C}, \theta)} d\tilde{\Psi} = - \int_{\theta_R}^\theta \eta(\mathbf{C}, \theta) d\theta, \quad (\text{D.5})$$

yielding

$$\begin{aligned} \tilde{\Psi}(\mathbf{C}, \theta) &= \tilde{\Psi}(\mathbf{C}, \theta_R) - \int_{\theta_R}^\theta \left( \eta_R(\mathbf{C}) + c_v \ln \frac{\theta}{\theta_R} \right) d\theta \\ &= \tilde{\Psi}(\mathbf{C}, \theta_R) - (\theta - \theta_R) \eta_R(\mathbf{C}) + c_v \left( \theta - \theta_R - \theta \ln \frac{\theta}{\theta_R} \right), \end{aligned} \quad (\text{D.6})$$

which can be finally written as

$$\tilde{\Psi}(\mathbf{C}, \theta) = \tilde{\Psi}_m(\mathbf{C}) - \eta_R(\mathbf{C})(\theta - \theta_R) + \tilde{\Psi}_\theta(\theta), \quad (\text{D.7})$$

with

$$\tilde{\Psi}_m(\mathbf{C}) = \tilde{\Psi}(\mathbf{C}, \theta_R); \quad \tilde{\Psi}_\theta(\theta) = c_v \left( \theta - \theta_R - \theta \ln \frac{\theta}{\theta_R} \right). \quad (\text{D.8})$$

## References

- [1] J. M. Ball. Convexity conditions and existence theorems in nonlinear elasticity. *Archive for Rational Mechanics and Analysis*, 63(4):337–403, 1976.
- [2] J. M. Ball. Energy-minimising configurations in nonlinear elasticity. *Archive for Rational Mechanics and Analysis*, 63(4):337–403, 1976.
- [3] J. M. Ball. *Geometry, Mechanics and Dynamics*, chapter Some open problems in Elasticity, pages 3–59. Springer, 2002.
- [4] J. M. Ball and F. Murat.  $W^{1,p}$ -quasiconvexity and variational problems for multiple integrals. *Journal of Functional Analysis*, 58(3):225–253, 1984.
- [5] K. J. Bathe. *Finite Element Procedures*. Prentice Hall, 1996.
- [6] P. Betsch, A. Janz, and C. Hesch. A mixed variational framework for the design of energy-momentum schemes inspired by the structure of polyconvex stored energy functions. *Computer Methods in Applied Mechanics and Engineering*, 335:660–696, 2018.
- [7] J. Bonet, A. J. Gil, C. H. Lee, M. Aguirre, and R. Ortigosa. A first order hyperbolic framework for large strain computational solid dynamics - Part I: Total Lagrangian isothermal elasticity. *Computer Methods in Applied Mechanics and Engineering*, 283(0):689–732, 2015.
- [8] J. Bonet, A. J. Gil, and R. Ortigosa. A computational framework for polyconvex large strain elasticity. *Computer Methods in Applied Mechanics and Engineering*, 283:1061–1094, 2015.
- [9] J. Bonet, A. J. Gil, and R. Ortigosa. On a tensor cross product based formulation of large strain solid mechanics. *International Journal of Solids and Structures*, 84:49–63, 2016.
- [10] J. Bonet, A. J. Gil, and R. D. Wood. *Nonlinear Continuum Mechanics for Finite Element Analysis: Statics*. Cambridge University Press, 2016.
- [11] J. Bonet, C. H. Lee, A. J. Gil, and A. Ghavamian. A first order hyperbolic framework for large strain computational solid dynamics - Part III: Thermo-elasticity. *Computer Methods in Applied Mechanics and Engineering*. Under review.
- [12] R. de Boer. *Vektor- und Tensorrechnung für Ingenieure*. Springer-Verlag, 1982.
- [13] E.A. de Souza Neto, D. Perić, and D.R.J. Owen. *Computational Methods for Plasticity. Theory and Applications*. 2008.
- [14] M Franke, A. Janz, M. Schiebl, and P. Betsch. An energy momentum consistent integration scheme using a polyconvexity-based framework for nonlinear thermo-elastodynamics. *International Journal for Numerical Methods in Engineering*, 115:549–577, 2018.
- [15] O. Gonzalez. Exact energy and momentum conserving algorithms for general models in nonlinear elasticity. *Comput. Methods Appl. Mech. Engrg.*, 190:1763–1783, 2000.
- [16] O. Gonzalez and A. M. Stuart. *A first course in Continuum Mechanics*. Cambridge University Press, 2008.
- [17] M. Groß and P. Betsch. Energy-momentum consistent finite element discretization of dynamic finite viscoelasticity. *Int. J. Numer. Meth. Engng*, 81(11):1341–1386, 2010.

- [18] C. Hesch and P. Betsch. Energy-momentum consistent algorithms for dynamic thermomechanical problems—Application to mortar domain decomposition problems. *International Journal for Numerical Methods in Engineering*, 86(11):1277–1302, 2011.
- [19] D. Kuhl and M. A. Crisfield. Constraint energy momentum algorighm and its application to non-linear structural dynamics of shells. *Computer Methods in Applied Mechanics and Engineering*, 136:293–315, 1996.
- [20] D. Kuhl and M. A. Crisfield. Energy-conserving and decaying algorithms in non-linear structural dynamics. *International Journal for Numerical Methods in Engineering*, 45:565–599, 1999.
- [21] S. C. Martín and J. C. García Orden. On energy-entropy-momentum integration methods for discrete thermo-visco-elastodynamics. *Computers & Structures*, 181:3–20, 2017. UK Association of Computational Mechanics.
- [22] R. Ortigosa, M. Franke, A. Janz, A.J. Gil, and P. Betsch. An energy–momentum time integration scheme based on a convex multi-variable framework for non-linear electroelastodynamics. *Computer Methods in Applied Mechanics and Engineering*, 339:1–35, 2018.
- [23] Ignacio Romero. Algorithms for coupled problems that preserve symmetries and the laws of thermodynamics: Part I: Monolithic integrators and their application to finite strain thermoelasticity. *Computer Methods in Applied Mechanics and Engineering*, 199(25):1841 – 1858, 2010.
- [24] J. Schröder. Anisotropic polyconvex energies. In J. Schröder and P. Neff, editors, *Poly-, quasi- and rank-one convexity in Applied Mechanics*, volume 516 of *CISM Courses and Lectures*, volume 516 of CISM Courses and Lectures, pages 53–105. Springer-Verlag, 2010.
- [25] J. C. Simo and N. Tarnow. The discrete energy-momentum method. Conserving algorithms for nonlinear elastodynamics. *Zeitschrift für angewandte Mathematik und Physik ZAMP*, 43(5):757–792, Sep 1992.